

**REPORT DOCUMENTATION PAGE**

*Form Approved  
OMB No. 0704-0188*

The public reporting burden for this collection of information is estimated to average 1 hour per response, including the time for reviewing instructions, searching existing data sources, gathering and maintaining the data needed, and completing and reviewing the collection of information. Send comments regarding this burden estimate or any other aspect of this collection of information, including suggestions for reducing the burden, to the Department of Defense, Executive Services and Communications Directorate (0704-0188). Respondents should be aware that notwithstanding any other provision of law, no person shall be subject to any penalty for failing to comply with a collection of information if it does not display a currently valid OMB control number.

**PLEASE DO NOT RETURN YOUR FORM TO THE ABOVE ORGANIZATION.**

<b>1. REPORT DATE (DD-MM-YYYY)</b> 02-28-2011	<b>2. REPORT TYPE</b> Final Report	<b>3. DATES COVERED (From - To)</b> 02-15-2008 to 11-30-2010
--	---------------------------------------	---

<b>4. TITLE AND SUBTITLE</b> Improving the Distortional Deformation Capabilities of Aerospace Composite Networks	<b>5a. CONTRACT NUMBER</b> FA9550-08-1-0077
	<b>5b. GRANT NUMBER</b>
	<b>5c. PROGRAM ELEMENT NUMBER</b>

<b>6. AUTHOR(S)</b> Jeffrey S. Wiggins	<b>5d. PROJECT NUMBER</b>
	<b>5e. TASK NUMBER</b>
	<b>5f. WORK UNIT NUMBER</b>

<b>7. PERFORMING ORGANIZATION NAME(S) AND ADDRESS(ES)</b> The University of Southern Mississippi School of Polymers and High Performance Materials 118 College Drive - Hattiesburg, MS 39406	<b>8. PERFORMING ORGANIZATION REPORT NUMBER</b>
---	---

<b>9. SPONSORING/MONITORING AGENCY NAME(S) AND ADDRESS(ES)</b> Air Force Office of Scientific Research 875 North Randolph Street, Suite 325, Room 3112, Arlington, Va., 22203-1768	<b>10. SPONSOR/MONITOR'S ACRONYM(S)</b> AFOSR
	<b>11. SPONSOR/MONITOR'S REPORT NUMBER(S)</b> AFRL-OSR-VA-TR-2012-0216

**12. DISTRIBUTION/AVAILABILITY STATEMENT**  
DISTRIBUTION STATEMENT A. Approved for public release; distribution unlimited

**13. SUPPLEMENTARY NOTES**

**14. ABSTRACT**  
Currently, the University in collaboration with Boeing Research and Technology, through leveraged financial support provided by AFOSR has established a comprehensive academic research platform based upon the development and utilization of multi-scale computational methods for designing composite matrix network chemistries with enhanced thermo-mechanical performance. Molecular dynamics models have been combined with advanced solution-to-gel-solid state analytical techniques to enhance computational accuracy and validate their accuracy. Our research platform is using computational methods to design new network architectures with enhanced performance, scaling up select chemistries, formulating new chemistries into network B-stage prepolymers, collating new chemistries with carbon fibers for high quality prepregs, curing new chemistries into aerospace quality test panels, and testing aerospace coupons for performance attributes predicted from computational models. Data generated through this iterative approach is used to validate and/or improve the computational methods under development.

**15. SUBJECT TERMS**

<b>16. SECURITY CLASSIFICATION OF:</b>			<b>17. LIMITATION OF ABSTRACT</b>  UU	<b>18. NUMBER OF PAGES</b>	<b>19a. NAME OF RESPONSIBLE PERSON</b> Connie Wyldmon, Director, SPA
a. REPORT	b. ABSTRACT	c. THIS PAGE			<b>19b. TELEPHONE NUMBER (Include area code)</b> 601.266.4119

Reset

## Executive Summary

In June 2007, the University of Southern Mississippi, Dr. Jeff Wiggins as P.I., submitted a proposal to AFOSR, Dr. Charles Lee as Program Manager, titled, “*Improving the Distortional Deformation Capabilities of Aerospace Composite Networks*”. The proposal was reviewed by AFOSR and awarded (FA9550-08-1-0077) February 15, 2008 in the amount of \$314,448 with an ending date of November 30, 2010. This report is the Final Report for FA9550-08-0077.

Motivation for this proposal was generated through prior-established research collaboration with Boeing Research and Technology (formerly Boeing Phantom Works) with an annual matching award from Boeing in the amount of \$50,000 annually during the period of the AFOSR award, and Boeing has fulfilled their match awards.

Additionally, in August, 2008 the University of Southern Mississippi, Dr. Jeff Wiggins as P.I. submitted a DURIP proposal to AFOSR, Dr. Charles Lee as Program Manager, titled, “*High Viscosity Polymer Mixer, Film and Prepreg System for Improving Computational Methods that Advance Composite Matrix Research*”. The proposal was reviewed by AFOSR and awarded (FA9550-09-1-0442) June 5, 2009 in the amount of \$264,003 with matching awards of \$132,000 by Boeing and \$132,000 by the University VP of Research. Matching awards were received. July 22, 2009 a change in AFOSR research portfolios was announced, and notification was provided Dr. Joycelyn Harrison was assigned Program Manager for both awards under the Low Density Aerospace Materials (formerly Polymer Matrix Composite) Portfolio. The focus of this report is the scientific accomplishments provided through FA9550-08-1-0077, but both AFOSR awards combined with over \$500,000 financial support from Boeing Research and Technology during this period have substantially impacted the research capabilities at the University for developing next generation aerospace structure and scientists.

## AFOSR FA9550-08-1-0077 Scientific Contributions

1. **Graduate Student Support:** AFOSR financial support has been instrumental towards providing a computational matrix research platform for aerospace. Our focus in this area is to develop a next generation scientist with the combined computational and experimental skills to drive the advancement of composite matrix science and engineering into the next generation. We are providing internships for select US Citizen students in combination with their fundamental scientific research dissertations.
  - a. **Dr. Sam Tucker:** Graduated in December 2010, Dissertation title, “*Study of 3,3’ vs. 4,4’ DDS Isomer Curatives on Physical Properties and Phenyl Ring Motions of DGEBA Epoxy via Molecular Dynamics, Deuterium NMR and Dielectric Spectroscopy*”. Dr. Tucker had a 3 month internship at Boeing Research and Technology (Seattle) in 2008 with Steve Christensen advancing multi-scale computational methods for aerospace. Currently employed at Boeing Research

and Technology in the Computational Methods group in the Structures Organization.

- b. **Mr. Matthew Jackson:** Anticipated graduation (Ph.D.) in August 2011, Dissertation title, “*Study of Solvent Ingress into Glassy Polymer Networks via Molecular Dynamics Methods*”. Mr. Jackson spent a 3 month internship at Boeing Research and Technology in summer 2009 under Steve Christensen advancing multi-scale computational methods for aerospace. He is currently a Boeing Research and Technology employee (on leave of absence while he completes his degree) and in negotiation with Boeing for his permanent employment.
- c. **Mr. Stephen Heinz:** Anticipated graduation (Ph.D.) in August 2011, Dissertation title, “*Development of Digital Image Correlation Techniques to Quantify Deformation Behavior of Glassy Polymer Networks*”. Mr. Heinz spent a 3 month internship at Boeing Research and Technology in summer 2010 under Gregg Bogucki advancing multi-scale computational methods for aerospace. He is currently a Boeing Research and Technology employee (on leave of absence while he completes his degree) and in negotiation with Boeing for his permanent employment.
- d. **Ms. Katherine Frank:** Anticipated graduation (Ph.D.) in December 2012, Dissertation title, “*Influence of Bulky Pendant Groups on Molecular Relaxations and Deformation of Glassy Polymer Networks*”. Ms. Frank spent a 3 month internship at Boeing Research and Technology in Summer 2010 under Steve Christensen advancing multi-scale computational methods for aerospace. She is currently a Boeing Research and Technology employee (on leave of absence while she completes her degree). Although not currently in permanent employment negotiation, she is expected to remain a research scientist within the aerospace community.

## 2. AFOSR FA9550-08-1-0077 Publications:

- a. *Uniaxial Compression Analysis Of Glassy Polymer Networks Using Digital Image Correlation*, S.R. Heinz and J.S. Wiggins, *Polymer Testing*, 29 (2010) 925-932
- b. *Failure of the Open Hole Off-Axis Tensile Specimen*, J.E. Goodsell, J. Dustin, A. Ritchey, S.R. Heinz, J.S. Wiggins and R.B. Pipes, *Am. Soc. Comp.*, submitted for publication 2010
- c. *Free Volume Dependence on Solvent Resistance of Crosslinked Epoxy Resins*; M.B. Jackson, M. Kaushik, S. Ward, R. Maskell, S. Nazarenko and J.S. Wiggins;

Society for the Advancement of Material and Process Engineering, International Symposium Proceedings, Salt Lake City, October 2010

- d. *Effects of network architecture and post cure conditions on mechanical properties of various epoxy-amine systems*; S.R. Heinz and J.S. Wiggins; Society for the Advancement of Material and Process Engineering, International Symposium Proceedings, Salt Lake City, October 2010
- e. *Molecular dynamics study on the effect of molecular weight between crosslinks on thermomechanical properties of aerospace epoxies*; Childers, Christopher H.; Tucker, Samuel J.; Wiggins, Jeffrey S.; Polymer Preprints (American Chemical Society, Division of Polymer Chemistry) (2010), 51(1), 815-816.
- f. *Study of Molecular Motions in Epoxy Networks Using Solid State Deuterium NMR*; Tucker, Samuel J. and Wiggins, Jeffrey S.; SAMPE 2010 Technical Conference Proceedings: New Materials and Processes for a New Economy, Seattle, WA, May 17-20, 2010.
- g. *Isomer Effects on Strain Recovery Properties of Glassy Polymer Networks Determined via Digital Image Correlation (DIC)*; Heinz, S. R. and Wiggins, J. S.; Society for the Advancement of Material and Process Engineering 2010 Technical Conference Proceedings: New Materials and Processes for a New Economy, Seattle, WA, May 17-20, 2010.
- h. *Advanced analysis of yield characteristics of composite polymer matrices using digital image correlation*; Heinz, Stephen R. and Wiggins, Jeffrey S.; Society for the Advancement of Material and Process Engineering, International Symposium Proceedings, ISBN 978-1-934551-05-9, 2009
- i. *Molecular dynamics simulation and synthetic experimentation results for a novel Triphenylamino triazine composite matrix curative*; Jackson, Matthew B., Tucker, Samuel J. and Wiggins, Jeffrey S.; Society for the Advancement of Material and Process Engineering, International Symposium Proceedings, ISBN 978-1-934551-05-9, 2009
- j. *Curing kinetics of aerospace epoxy resins by in-situ variable temperature NMR*; Tucker, Samuel J. and Wiggins, Jeffrey S.; Society for the Advancement of Material and Process Engineering, International Symposium Proceedings, ISBN 978-1-934551-05-9, 2009
- k. *Rheological behavior and morphology of polyhedral oligomeric silsesquioxane (POSS) epoxy nanocomposites*; Kar, Sritama; Wiggins, Jeffrey S.; Polymer Preprints (American Chemical Society, Division of Polymer Chemistry) (2009), 50(1)
- l. *Dispersion characteristics of polyhedral oligomeric silsesquioxane nanostructured chemicals into a biphenol-A epichlorohydrin/3,3'' DDS epoxy system*; Cook, Robert D.; Kar, Sritama; Wei, Yuhong; Misra, Rahul; Wiggins,

Jeffrey S.; Morgan, Sarah E. Polymer Preprints (American Chemical Society, Division of Polymer Chemistry) (2009), 50(1)

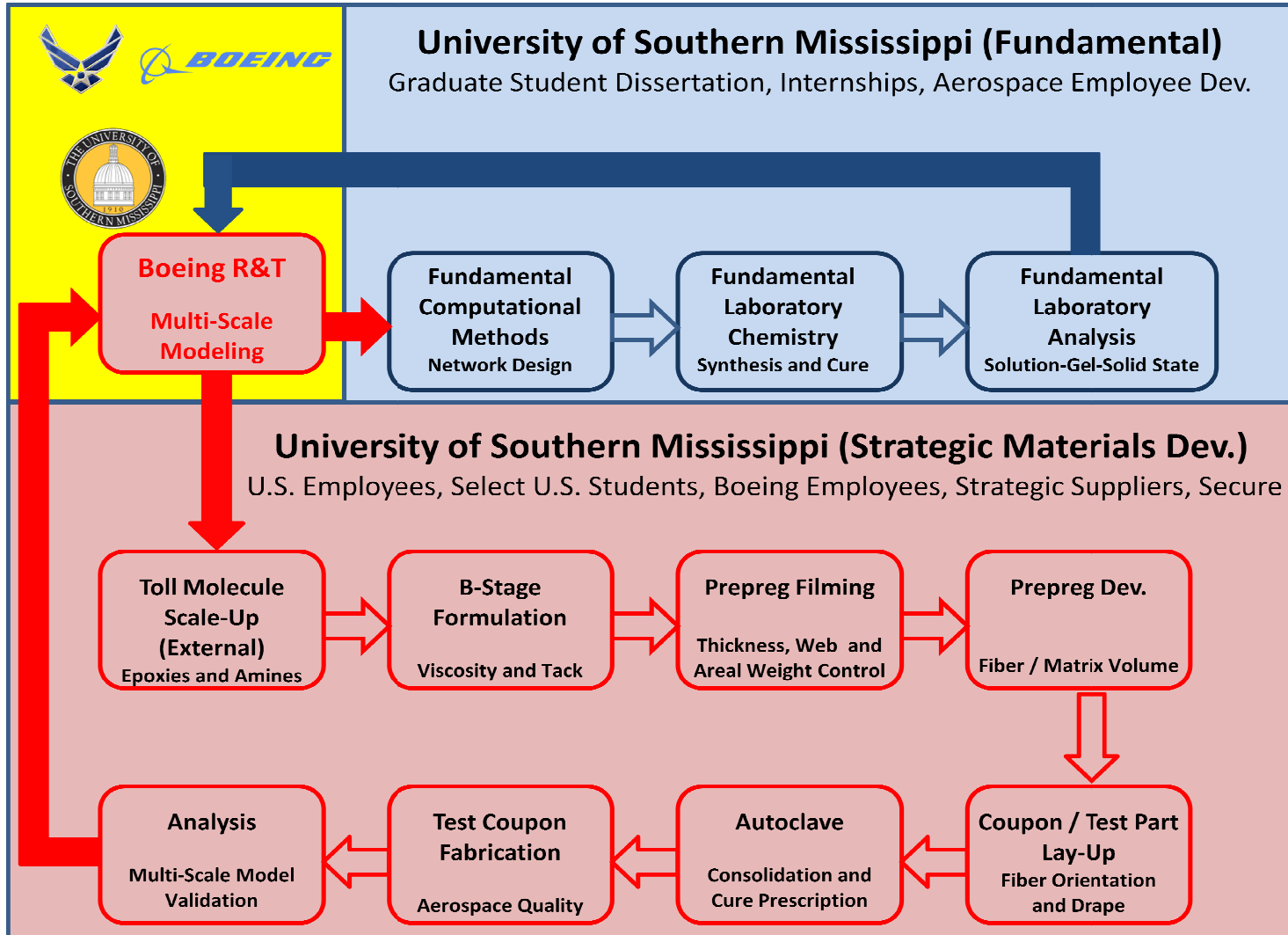
- m. *Room Temperature Cured Resin Systems*; Brooks, Olivia D.; Richey, Toby; Tucker, Samuel J.; Jackson, Mathew; Heinz, Stephen; Wiggins, Jeffrey S.; Abstracts, 60th Southeast Regional Meeting of the American Chemical Society, Nashville, TN, United States, November 12-15 (2008), SERM-421
- n. *Room temperature cure epoxy resin systems*; O.D. Brooks, R. Toby; S.J. Tucker, M.B. Jackson, and J.S. Wiggins; Abstracts of Papers, 235th ACS National Meeting, New Orleans, LA, United States, April 6-10, (2008), POLY-169.

### 3. AFOSR FA9550-08-1-0077 International Symposia Organized:

- a. *Epoxy Matrices*, Society for the Advancement of Material and Process Engineering (SAMPE) October 19-22, 2009 *Epoxy Matrices*,
- b. *Non-Epoxy Matrices*, Society for the Advancement of Material and Process Engineering (SAMPE) October 19-22, 2009
- c. *POSS Resin Systems*; Society for the Advancement of Material and Process Engineering (SAMPE) October 19-22, 2009
- d. *POSS Nanostructured Chemicals*; Society for the Advancement of Material and Process Engineering (SAMPE) May, 2010
- e. *Composite Matrix Chemistry and Science*; Society for the Advancement of Material and Process Engineering (SAMPE) October, 2010

### 4. AFOSR FA9550-08-1-0077 Computational Research Platform: Matrix Chemistry

Currently, the University in collaboration with Boeing Research and Technology, through leveraged financial support provided by AFOSR has established a comprehensive academic research platform based upon the development and utilization of multi-scale computational methods for designing composite matrix network chemistries with enhanced thermo-mechanical performance. Molecular dynamics models have been combined with advanced solution-to-gel-solid state analytical techniques to enhance computational accuracy and validate their accuracy. Our research platform is using computational methods to design new network architectures with enhanced performance, scaling up select chemistries, formulating new chemistries into network B-stage prepolymers, collating new chemistries with carbon fibers for high quality prepregs, curing new chemistries into aerospace quality test panels, and testing aerospace coupons for performance attributes predicted from computational models. Data generated through this iterative approach is used to validate and/or improve the computational methods under development. Our collaboration with Boeing Research and Technology is on-going continued to expand during this funding period, and the goals supported by AFOSR financially have helped establish a computational based approach to next generation structure design and scientists



AFOSR FA9550-08-1-0077 and AFOSR FA9550-09-1-0442  
 Computational Matrix Chemistry Research Platform

## **AFOSR FA9550-08-1-0077 Final Report**

### **Introduction**

Advancing a multiscale understanding of composites which range in length and time scales from the quantum/molecular matrix level through the structural continuum will provide scientists confidence for incorporating composites into applications. In order to do so, it is necessary to increase knowledge of how glassy polymer network solids influence and control critical structural performance. Linking glassy polymer network chemistry to structural capabilities has been difficult due to the complexities of analyzing intractable, insoluble, and thermally stable polymer network solids. In particular, connecting matrix chemistry to strain induced structural failures is particularly complicated since fracture initiation and progression in fiber-reinforced composites is quite complex and involves numerous failure modes associated with interfacial delamination, fiber-matrix interfaces, matrix cracking, fiber-breakage, and etc.

To advance understanding of glassy amorphous thermosets used in composite applications, two aerospace-grade matrices will be the focus of this work. The industry standard diepoxy, the diglycidyl ether of bisphenol A (DGEBA) will be cured with the tetra-functional diamines 3,3'-diaminodiphenyl sulfone (33DDS) and 4,4'-diaminodiphenyl sulfone (44DDS); shown in Figure 1. In addition to using industrially prevalent matrices, the use of isomeric amines provides the opportunity to study the effect on properties of aromatic networks possessing meta-substitution versus a fully para-substituted network. Specific objectives of this research are as follows:

- (1) In order to advance multiscale understanding of composite matrices, molecular dynamics simulations will be used to predict properties of matrices. Simulated properties will be

compared to experimentally determined properties for 33DDS/DGEBA and 44DDS/DGEBA to determine accuracy of simulations. Where simulations do not match experimental values, improvements to the simulation procedure will be made. Simulations will also be accomplished to determine the effects of meta-substitution in the backbone, varied crosslink density, aromatic and sulfone group content, and pendant bulky group incorporation.

(2) Polymer network glassy state (sub- $T_g$ ) molecular motions will be analyzed to gain an understanding of the chemical structures undergoing molecular motion and the types and rates of those motions using deuterium ( $^2\text{H}$ ) and carbon ( $^{13}\text{C}$ ) solid state NMR spectroscopy. Glassy state relaxations will be characterized with dielectric spectroscopy (DES) and dynamic mechanical analysis (DMA). The rates and types of motion seen in NMR spectroscopy will be related to the secondary transitions seen in DES and DMA for 33DDS/DGEBA and 44DDS/DGEBA matrices.

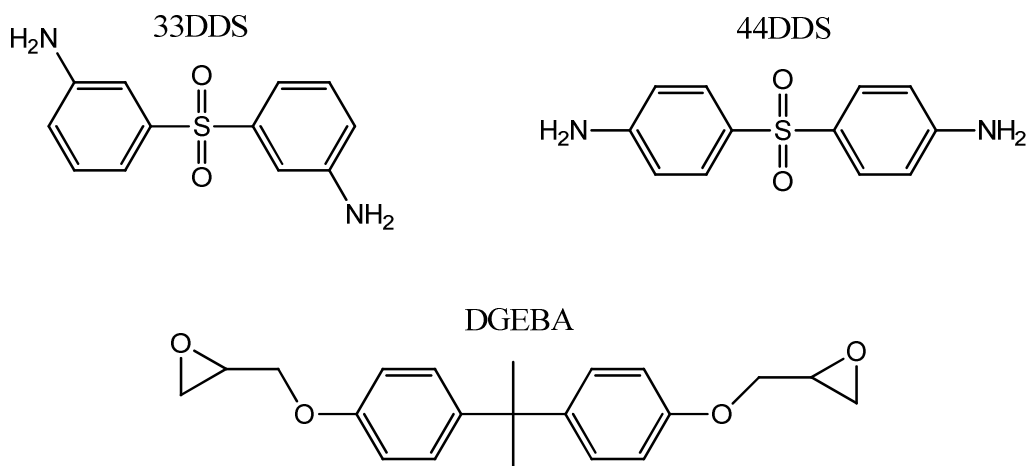


**Figure 1.** Structures of 44DDS, 33DDS, and DGEBA.

Epoxy networks are formed through step-growth polymerization reactions where glycidyl rings open in the presence of strong nucleophiles. Tetra-functional aromatic and aliphatic diamines are commonly used as curing agents for epoxies due to their economics and performance. Network formation usually occurs through two isothermal reaction steps. The first step is generally conducted at a lower temperature condition which promotes the formation of linear step-growth oligomers through primary amine-oxirane reactions, sometimes referred to as “B-stage.” The second step of the cure is performed at a higher temperature where secondary amine-oxirane crosslinking reactions drive the ultimate network formation. At some point of curing, dependent upon the flexibility of the molecules, reactive groups no longer possess the configurational freedom to come into contact with other reactive groups and form a bond. The network reaches its vitrified state when chemical reactions stop occurring, and crosslink density and network architecture remain constant. The extent of cure obtained during the post-cure drives the network into the vitrified state, thus giving the network its ultimate thermomechanical properties

Chemical compositions and crosslink densities are two factors that govern the thermal and physical properties of polymer networks.<sup>1,2</sup> Chemical composition refers to the chemical make-up of the polymer, including backbone features such as aromaticity, ethers, sulfones, etc and functional groups. In general, networks containing aromatic moieties show increased rigidity and thermal stability when compared to networks comprised from aliphatics. Hydroxyl groups form during the amine-oxirane ring opening reaction and contribute to network properties through hydrogen bonding with tertiary amines and other hydroxyls.<sup>3</sup> A recent report demonstrated that increasing intermolecular interactions through a higher density of hydrogen

bonding increased the low-deformation mechanical properties of epoxy networks at temperatures between secondary and primary relaxations.<sup>4</sup>

Crosslink density also has a significant effect on network properties. In general, a higher crosslink density results in a higher modulus,<sup>5</sup> and longer chain segments generally display higher degrees of local chain mobility and flexibility leading to a reduction in modulus.<sup>6</sup> The crosslink density of a network is dependent upon the molecular weight between crosslinks and the extent of reaction; higher conversion results in higher crosslink density. Quantitative conversion of functional groups in an epoxy is never attained due to network vitrification; the fully cured network architecture is comprised of tertiary and secondary amines. As a result, molecular weight of the monomers affects the average molecular weight between crosslinks,  $M_c$ , but does not precisely determine it.<sup>7</sup>

### **Multi-Scale Modeling**

In multi-scale modeling, the goal is to predict the properties and behavior of complex structures across all relevant time-length scales starting from fundamental chemical and physical mechanisms. Macroscopic material properties and behaviors, such as strength and performance, are always associated with phenomena that occur on a smaller length scale including the localization of micro-defects. When sub-scale events are examined in detail, it is found that these events result from mechanisms that occur on finer time-length scales, with root analysis leading to quantum and molecular level events. When molecular dynamics models are more accurate, modeling frameworks which capture dominant mechanisms across all time-length scales will offer more reliable predictive capabilities.

Despite extensive material research and development, high-modulus matrix resins used in advanced aerospace composites have historically been labeled as brittle. Whether or not this behavior is manifested will be dependent on the local strain environment. Advancements in molecular dynamics modeling provide insights to further study the physical deformations of glassy polymers. The mechanisms of glassy polymer distortions in response to applied strains are not well-understood, nor is there an accurate model that relates distortional capabilities of glassy polymers to specific structural chemistries. This deficiency is a key limitation for advancing reliable multi-scale models that relate matrix chemistry to ultimate composite performance.

Boeing Research and Technology has recently introduced the physics-based Onset Theory to reduce its dependence on empirical testing for the prediction of ultimate composite performance in advanced aerospace structures.<sup>8</sup> Onset Theory is a strain-based method, which uses invariant, scalar values to determine the onset of critical events that result in ultimate composite failure. Onset Theory predicts that composite matrix damage initiation is essentially controlled by two strain invariants, the first invariant of the strain tensor,  $J_1$ , associated with laminar transverse cracking failure dominated by volume increase of the matrix, and the von Mises strain, associated with equivalent strain and shape change of the matrix, a function of the second invariant of the strain deviator tensor,  $\epsilon_{vm}$ . Invariants are terms for mathematical constructs which remain unchanged when certain types of transformations are applied.  $J_1$  and  $\epsilon_{vm}$  are invariant to rotation of the principle axis system, meaning they are invariant to the geometry of the sample or the direction in which strain is applied.  $J_1$  gives a measure of the dilational response of the material to an applied strain, while  $\epsilon_{vm}$  measures the distortional response. Distortion and dilation will be further discussed in the following section within the introduction.

Onset Theory has shown that matrix fracture initiation, independent of structural designs and modes of loading, is associated with the effective critical volumetric or equivalent strains of the lamina. In composite lamina tensile tests, as the fiber angle within the composite increases, the method of failure changes from distortional to dilatational (Figure 1.2).<sup>9</sup> In composites, when critical volumetric or equivalent strains are reached, failure of the composite is imminent. Therefore, the most efficient approach to significantly improve performance of composite structures is to improve the von Mises strain of the matrix. Onset Theory will provide keys to:

- predict the strength of complex structures from basic properties
- reduce the number of durability tests
- link resin properties to composite properties
- simplify moisture and thermal degradations at the matrix molecular level<sup>10</sup>

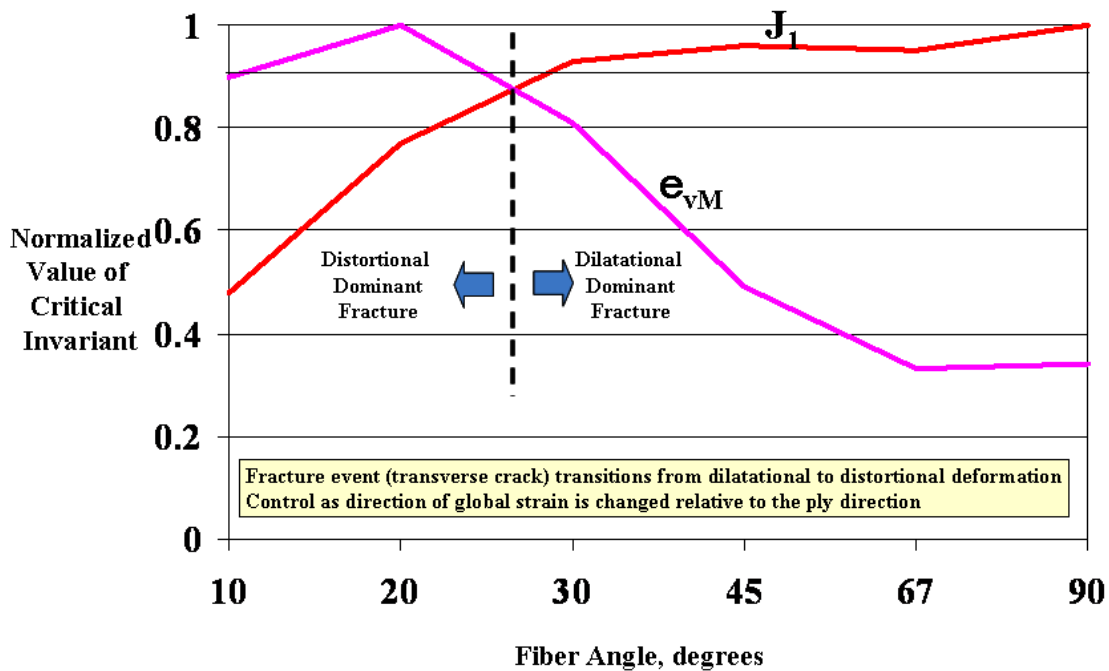


Figure 2. Invariant value vs. fiber angle for lamina tensile tests (S. Christensen, Boeing).

## **Polymer Dilatational and Distortional Deformations**

Polymer deformation models have been the subject of intense physical polymer research for several decades.<sup>11</sup> The evolution of molecular modeling over the last decade has provided new opportunities for scientists to study the physical interactions of glassy polymers, and one of the most powerful methods to study these nanoscopic events is molecular dynamics modeling. Molecular systems are studied by applying laws of chemistry, physics, and mathematics to predict molecular behavior via computer simulation. Due to the complex nature of physical interactions between polymers and a lack of analytical methods sufficiently sensitive to measure molecular level stresses and strains, molecular dynamics simulations are providing new molecular-level insights toward understanding the bulk property responses of polymers subjected to applied forces.<sup>12</sup>

In polymers, certain stress-field conditions may cause crazing. A craze is a narrow zone of highly deformed and voided polymer. The relevant criterion for craze formation proposed by Sternstein and Ongchin can be interpreted as a critical volume increase related to a critical polymer chain mobility induced by stress.<sup>13</sup> The development of cavitation is recognized as a leading energy dissipation process during the deformation of glassy polymers and largely controls their resistance to mechanical loading.<sup>14</sup> It has been shown that cavitation relieves hydrostatic tension in the matrix, increases deviatoric stresses, and promotes shear deformation.<sup>15</sup> The contribution of cavitation has proven to be essential to adequately model plasticity in zones of highly stressed fields including crack tips.

Condensed matter can deform in one of two ways: dilatation and distortion. At some amount of deformation, either dilatation or distortion becomes critical, and permanent deformation results. Materials are said to dilate when induced stress causes a deformation

resulting in volume expansion in the material but not a change in shape as depicted in Figure 3. Equation 1.1 gives the definition of  $J_1$ , which accounts for over 98% of the dilational strain. If the volume expansion is small, the cohesive forces of the material will persevere, and the material will recover to its initial volume upon release of the applied stress. However, if the stress causes large molecular displacements and cohesive forces in the material are exceeded, an increase in volume of the material will occur due to the formation of nanoscopic cavities. Once formed, cavities become permanent weaknesses within the material eventually leading to the onset of crack propagation and catastrophic failure.

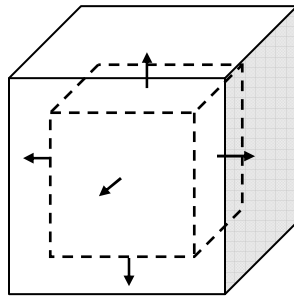


**Figure 3.** Pictorial representation of material dilation.

$$J_1 = \varepsilon_1 + \varepsilon_2 + \varepsilon_3$$

where:  $\varepsilon_1$ ,  $\varepsilon_2$ , and  $\varepsilon_3$  are the strains in the x, y, and z directions

**Equation 1.** Definition of the first invariant of the strain tensor,  $J_1$ .

Distortional deformation, depicted in Figure 4, is a molecular deformation mechanism that theoretically avoids cavitation by changing shape without undergoing a change in volume. Distortional deformation can be accurately measured by von Mises strain,  $\varepsilon_{vm}$ , defined in

Equation 2. In distortional deformation net frictional forces do not change and the ultimate strength of the material remains intact. Although intermolecular forces of attraction may be overcome during distortional events, the net result is a torsional movement of the material followed by recovery of the attractive forces that prevent the formation of cavities and cohesively hold the molecules intact. For these reasons, it is logical to conclude that increasing the distortional capability of a glassy polymer will lead to improved macroscale mechanics. Increasing the distortional capability of a polymer network involves enhancing the ability of the material to deform at the molecular level, and distortional deformation is dependent upon ability of the backbone to rotate through dihedral angles.<sup>16,17,18</sup> These rotations increase the ability of the system to respond to strain by means of plastic processes. Another way to reduce a polymer's resistance to plastic flow is to disperse toughening particles throughout the system, creating a cellular solid.<sup>18</sup> Particles are believed to increase the free-volume of the deformable material, increasing the uniformity of strain in the system, and ultimately augmenting the distortional capability of the network.<sup>18</sup>

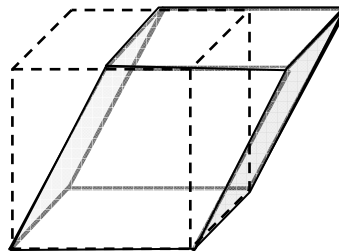


**Figure 1.4.** Pictorial representation of material distortion.

$$\varepsilon_{vm} = \sqrt{0.5 * [(\varepsilon_1 - \varepsilon_2)^2 + (\varepsilon_2 - \varepsilon_3)^2 + (\varepsilon_1 - \varepsilon_3)^2]}$$

where:  $\varepsilon_1$ ,  $\varepsilon_2$ , and  $\varepsilon_3$  are the strains in the x, y, and z directions

**Equation 2.** Definition of von Mises strain,  $\varepsilon_{vm}$ .

To better illustrate the molecular structure differences in dilational and distortional deformation behavior, well-known thermoplastic materials are good models for the purpose of demonstration. Relatively tough polycarbonate (PC) and polysulfone (PSu) are thermoplastics that exhibit classic distortional deformation under applied stress states as compared to relatively brittle polystyrene (PS) that displays classic dilational behavior.<sup>19</sup> When stress is applied to PC or PSu, the material responds with a plastic response in which no change in volume is observed. Practically speaking, distortion is responsible for the necking behavior of these polymers when put under tension, and for their relatively high impact strengths. On the other hand, polystyrene reacts to stress with a dilational response, generally does not neck under tension, and exhibits a relatively low-energy catastrophic failure in similar tensile and impact scenarios. A further noteworthy example is the behavior of brittle PS in unidirectional tensile stress testing under hydrostatic pressure. In this case, the material will deform without volume change and display distortional deformation behavior by necking, similar to polycarbonate. This examination of thermoplastic models including the backbone chemistries and torsional conformations that favor distortional deformation capabilities of glassy polymers can be used to provide insights for developing improved distortional capabilities within aerospace composite networks. Evaluating conformational rotations and molecular-level energy absorbing mechanisms by synthesizing model networks with controlled molecular level conformations is fundamental to this research. Controlled conformational positioning provides rotational mechanisms into the polymer backbone leading to variations in deformational and physical behaviors.

Cohesive forces in a material are governed by a balance between intermolecular attractions arising from Van der Waals forces and repulsions due to nearest neighbor effects<sup>20</sup>.

Van der Waals forces describe the complex combinations of dipole and electron-cloud distribution forces between molecules including Keesom forces, Debye forces, and London dispersion forces, which create instantaneous attractions between molecules.<sup>21,22,23</sup> Pauli repulsions result from the overlapping of proximal electron clouds and are the primary repulsive forces between molecules. The balance between these attractive and repulsive forces significantly influences physical properties of a material and can be described using the Lennard-Jones (L-J) 6-12 potential energy function depicted in Figure 6. The zero net force balance between attraction and repulsion occurs at a radial separation of about 3.4Å, and attractive forces are strongest when atoms are separated by 3.8Å. The interactions between attractive and repulsive forces dictate the energy barriers for bond rotations, such as gauche- to trans-conformations. Energy barriers associated with changes in molecular level conformations can also be considered as molecular level energy absorbing and dissipating mechanisms that control dilational and distortional modes of deformation in amorphous glassy polymers.

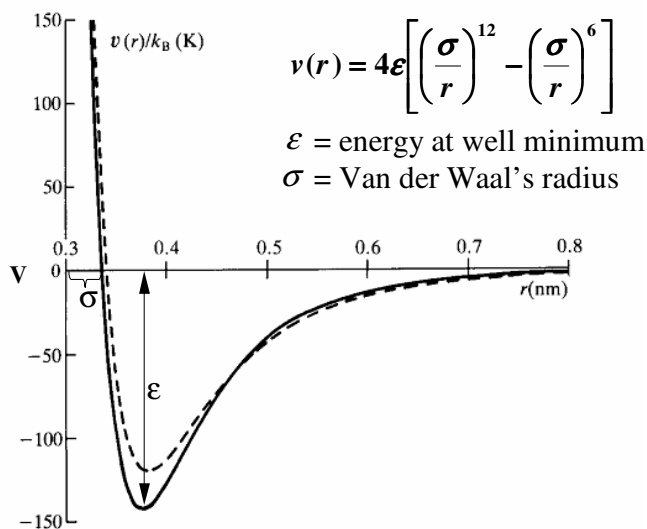


**Figure 6.** Lennard-Jones 6-12 Potential.

## **Secondary Relaxations**

Secondary relaxations are a broad term for relaxations in polymers other than the glass transition, which is termed the primary relaxation. Secondary relaxations are associated with short range sub- $T_g$  molecular motions, meaning they occur at lower temperatures than the long range cooperative motions which signal the onset of the glass transition. Since secondary relaxations occur below  $T_g$ , the term sub- $T_g$  relaxation is often used to refer to secondary relaxations. Secondary relaxations are usually attributed to simple motions such as methyl rotations, phenyl ring flips, or crankshaft motions of methylene sequences.<sup>24</sup> Secondary relaxations are of particular interest since applications based upon epoxy networks function in the glassy state, where simple, small scale molecular motion dominates polymer dynamics.

Secondary relaxations seen using dielectric spectroscopy (DES) and dynamic mechanical analysis (DMA) correlate with engineering properties such as tensile and compressive moduli, yield, fluid sensitivity, and electrical properties.<sup>4,25,26,27</sup> The mechanisms of secondary relaxations in glasses have been a topic of debate for the last several decades and are not completely agreed upon. In polymeric glasses, due to the complexity and heterogeneity in molecular structures, they are assumed to originate from different motions associated with varying length and time scales.<sup>28,29</sup>

Solid state NMR studies on molecular dynamics of typical model polymers have shed light on the origins of secondary relaxations. The sub- $T_g$  relaxation of poly(alkyl methacrylate) has been studied and believed to be associated with main chain motions caused from librations of ester side moieties.<sup>30,31</sup> The term libration refers to a nondescript motion in the backbone of the polymer caused by other distinct motions, such as the methyl rotations, phenyl ring flips, or crankshaft motions mentioned previously. Although speculated, it is not certain if the ester

librations trigger main chain motions, or the reverse is true.<sup>32</sup> Inglefield demonstrated through deuterium echo delay line shape experiments that the sub- $T_g$  relaxations observed in dynamic mechanical analysis for linear and crosslinked epoxy systems were composite motions of phenyl ring flips and trans-gauche isomerization of hydroxypropylether groups.<sup>28</sup> Ring flips were assigned as the faster motions contributing to mechanical loss in the low temperature region of the secondary relaxation, and the trans-gauche isomerization was assigned as the slower motions contributing to mechanical loss at the higher temperature region of the relaxation. The two motions mentioned above do not fully account for the sub- $T_g$  transition of epoxy polymers. Although Inglefield indicates the existence of even slower motions than observed for epoxy polymers, he could not conclusively identify the specific architectural contributions.

Temperature dependence for the rate of the secondary relaxation obeys the Arrhenius Equation; when plotting  $\tau_c$  vs. T the activation energy,  $E_a$ , and exponential (frequency) pre-factor,  $\tau_0^{-1}$ , are calculated (Equation 3).<sup>10</sup>

$$\tau_c^{-1} = \tau_0^{-1} * e^{\left(\frac{-E_a}{RT}\right)}$$

where:  $\tau_c$  = correlation time

$\tau_0$  = exponential pre-factor

$E_a$  = activation energy

R = the universal gas constant

T = temperature

**Equation 3.** Arrhenius equation for calculating activation energy.

As discussed above, more complex motions can be associated with motional “cooperativity” of neighboring groups. This “cooperativity” tends to slow molecular motions and increase the

activation energy of relaxations.<sup>33</sup> Intra- and inter-chain cooperativity in polymeric glasses is governed by molecular architecture including symmetry, rigidity, and steric hindrance.<sup>34</sup> Kremer, et al. incorporated cyclohexylene rings into the main-chains of PET and reported a cooperative secondary relaxation of ester group interactions with “chair-chair” conformational transitions.<sup>35</sup> Yee and coworkers reported the secondary relaxation in BPA-PC was associated with cooperative motions of chain lengths up to seven repeat units.<sup>36</sup> In contrast, BPA-polyformals containing methylene-diether groups represent more flexible polymers and show no evidence of cooperation larger than one repeat unit.<sup>37</sup> These observations suggest the extent of backbone rigidity controls the level of in-chain motional cooperativity.

Reports also suggest that simple relaxations have very little, or no, contribution to configurational entropy unless involved in cooperative motions.<sup>38,39</sup> Starkweather described a method for calculating configurational entropy as a thermodynamic criterion to distinguish between simple and cooperative secondary relaxations, and proposed that activation energies of secondary relaxations are expressed as Equation 4:

$$E_a = RT * \left[ 1 + \ln \left( \frac{kT}{2\pi hf} \right) \right] + T\Delta S$$

where:  $E_a$  and  $R$  are the same as defined in Equation 1.3

$k$  = Boltzman constant

$h$  = Plank's constant

$f$  = the frequency equal to  $\tau_c^{-1}$

$\Delta S$  = configurational entropy

$T$  = the temperature at which the relaxation reaches its peak.<sup>40</sup>

**Equation 4.** Starkweather expression for cooperativity of motions.

Figure 7 depicts the application of Equation 4 for distinguishing relaxations with varying degrees of cooperativity. The line in Figure 7 was drawn using Equation 2 at  $\Delta S = 0$ , which defines the theoretical limit of activation energy for secondary relaxations. The figure includes activation energy data extracted from several references<sup>28,41,42</sup> and represents a range of cooperative motions. In general, as the activation energies on this diagram deviate from the theoretical limit, or simple motion line, a higher degree of cooperativity is assigned to the polymer secondary motions.

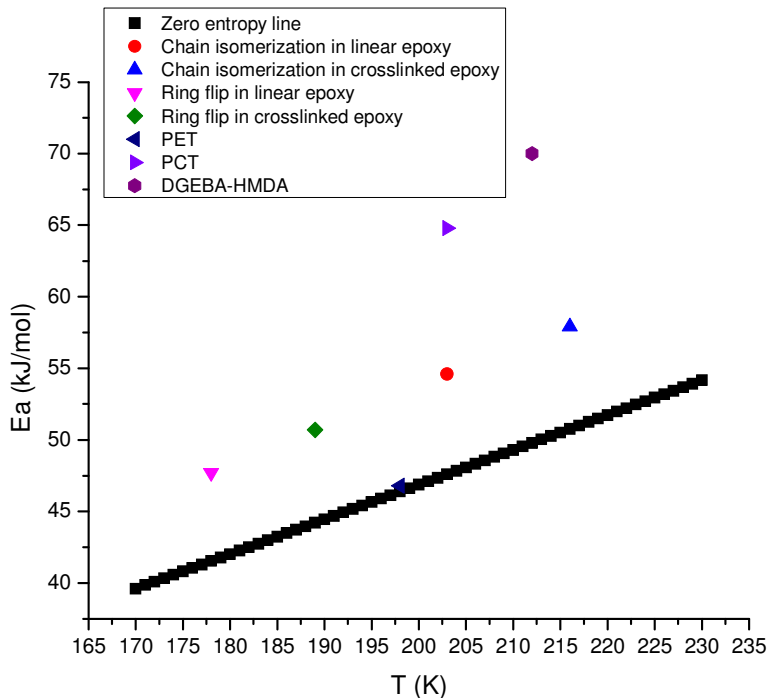


**Figure 7.** Starkweather plots of the  $E_a$  for several cooperative motions.

Johari and Goldstein discovered secondary relaxations in rigid small molecule glasses.<sup>43,44</sup> Since “local” motions are not possible for rigid molecules, this class of secondary relaxations is attributed to motions of the entire molecule. This principle suggests internal

flexibility of molecules is not a requirement for the occurrence of secondary relaxations.<sup>45,46</sup>

This class of secondary relaxations shows a temperature and pressure dependence, and is correlated to primary relaxations.<sup>47</sup> It was found that this class of secondary relaxations resembles primitive relaxations.<sup>48,49,50,51</sup> A primitive relaxation is a hypothetical local relaxation process for a small molecule or, in the case of polymers, a repeat unit. The similar characteristics of the special secondary relaxation and the primitive relaxation lead to a reasonable conclusion that the special secondary relaxation also functions as a precursor of the glass transition. To distinguish this secondary relaxation from other secondary relaxations, it is commonly recognized as the Johari-Goldstein  $\beta$ -relaxation in honor of their pioneering work.<sup>45</sup>

The JG  $\beta$ -relaxation was found in a variety of glasses including small molecule, metallic, and polymeric.<sup>52,53,54</sup> The universality of JG  $\beta$ -relaxation in glasses has been discussed and accepted by numerous researchers.<sup>55,56</sup> In polymeric glasses, research has mainly focused on linear polymers.<sup>57,58,59</sup> Very little work has been reported on crosslinked polymeric glasses regarding the mechanism of the JG  $\beta$ -relaxation, factors that affect its thermodynamic properties, or its correlation with the primary relaxation. Johari<sup>46</sup> and Beiner<sup>60</sup> examined the evolution of relaxation times during different stages of epoxy amine reactions. Johari calculated an  $E_{act}=63.4$  kJ/mol for the JG  $\beta$ -relaxation of 4,4'-diaminodicyclohexylamine and DGEBA, regardless of the extent of conversion.

Molecular dynamics has shown that the initial response of a Lennard-Jones material stretched between rigid walls is elastic due to intermolecular attractions. Molecular instability causes molecular level yielding behavior, ultimately resulting in cavitation within the material.<sup>61</sup> As shear strains are increased, local potential energy minima vanish, causing the system to become unstable and driving the system to relaxation at new minima.<sup>62</sup> Rather than a continuous

process, plastic flow of the system consists of a series of discrete yielding or cavitation events separated by nearly elastic behavior. As the material is continually strained, cavities become larger, increasing in size from nanoscopic to microscopic and eventually to macroscopic, where a coalescence of the cavities occurs, causing a complete fracturing of the material. The Lennard-Jones potential facilitates molecular modeling by providing the maintenance of minimum particle spacing and an estimate of long-range cohesion through its weakly attractive tail section.<sup>63</sup>

### **Configurational Entropy**

33DDS/DGEBA possesses more configurational entropy in the melt state than 44DDS/DGEBA. Due to the meta substitution, 33DDS/DGEBA possesses more configurations above  $T_g$ ; therefore, a larger amount of cooling from the melt state is required to eliminate the configurational entropy and cross the glass transition into the glassy state. The para substituted 44DDS creates a network with DGEBA consisting of only para linkages, giving 44DDS/DGEBA a lower number of configurations above  $T_g$ , and a lower amount of cooling is needed to eliminate the configurational entropy and become a glass. This difference in configuration entropy has the effect of lowering the glass transition of 33DDS/DGEBA when compared to 44DDS/DGEBA.

This explanation for 33DDS/DGEBA possessing a lower  $T_g$  than 44DDS/DGEBA also explains the higher density and lower amount of free volume in the 33DDS epoxy.<sup>64</sup> Polymer chains in epoxies cured with 33DDS possess a greater amount of flexibility due to the increased configurational entropy. This flexibility allows the chains to rearrange at lower temperatures, eliminating free volume to form more tightly packed amorphous networks than 44DDS epoxies.

The meta substitution also has an effect on the ability of the DDS rings to undergo ring-flipping, thus affecting secondary relaxations.<sup>65</sup> Phenyl rings in DGEBA and 44DDS can undergo facile rotation about the axis of symmetry comprised by the 1 and 4 phenyl ring bonds creating a phenyl ring  $\pi$ -flip (Figure 1.8).<sup>66,67</sup> The process requires the simultaneous rotation of two bonds: the bonds in the 1 and 4 positions of the phenyl ring.<sup>68</sup> Due to 33DDS's meta substitution, it does not possess an axis of symmetry through the phenyl ring, making it impossible for 33DDS rings to undergo ring flipping. Therefore, DDS ring flips, as a method of energy dissipation, are unavailable to the 33DDS/DGEBA network (Figure 8). When one of the bonds adjacent to the phenyl ring undergoes rotation, cooperative motions in the polymer backbone are necessary to relieve torsional strain.

Upon warming, the glass transition coincides with the onset of long-range segmental motions. In crosslinked aromatic systems, one bond rotations causing cooperative motions will result in long range segmental motions in the matrices. Therefore, the inability of 33DDS rings to undergo phenyl ring flips forces longer range cooperative motions as the result of a one bond rotation, having the effect of lowering  $T_g$  of 33DDS epoxies in comparison to 44DDS epoxies.

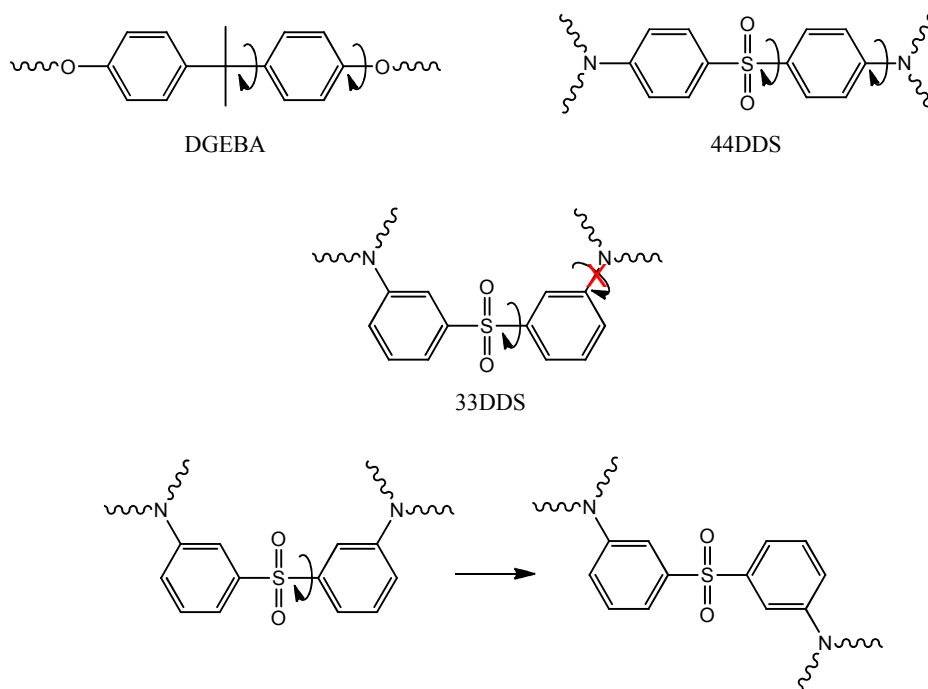


**Figure 8.** Phenyl ring  $\pi$ -flips in DGEBA and 44DDS are not possible in 33DDS forcing long range cooperative motion for a 33DDS phenyl ring rotation.

### Viscoelastic Mechanical Properties

Viscoelastic mechanical properties influence the performance of polymers in deformation and control stress relaxation, creep, and hysteresis.<sup>69</sup> Macroscopic deformations of materials, distortion and dilation, can be coupled to viscoelasticity. Linking viscoelastic behavior to chemical composition and architecture in glassy polymer network solids is critical since a variety of relaxations, including secondary relaxations, are used to probe macroscopic mechanical behavior.<sup>70</sup>

Figure 9 shows a stress-strain curve of an epoxy network in uniaxial compression. Deformations of glassy polymer networks in compression are governed through elastic, viscoelastic, and plastic responses. In the elastic region polymer chains undergo spring-like

affine deformations where the molecules are held intact by crosslinks and intermolecular cohesive forces. Strain recovers linearly and instantaneously upon release of stress in the elastic state.<sup>71</sup> Strain deviates from linearity under stress when the polymer enters its viscoelastic regime. Due to the viscoelastic nature of polymer chains, energy is dissipated in molecular movements and residual strain recovers more slowly after release of stress (non-instantaneous) so a time dependant factor is introduced. Raising the temperature accelerates viscoelastic strain recovery, showing these relaxations are time-temperature sensitive. As a result, by obtaining sets of measurements from a polymeric material at different temperatures and times, and using an appropriate shift factor,  $a_T$ , it is possible to assemble the data sets into a single “master curve” that represents stress relaxation data over a vast range of timescales.

Theoretically all viscoelastic strain is recoverable once the polymer is heated to above its  $T_g$ .<sup>72</sup> In the plastic regime, irreversible deformation occurs, and part of the strain developed is not recoverable. This can be explained by the cavitation of molecules and large dissipation of energy of this cavitation event.<sup>73</sup> Experimental techniques have been employed for decades to study viscoelasticity of glassy polymer solids; however, the phenomena is still not sufficiently understood. Although the connection of molecular motions and secondary relaxation processes to macroscopic viscoelastic behavior is not made in this work, it is the overall goal of advancing multi-scale understanding.

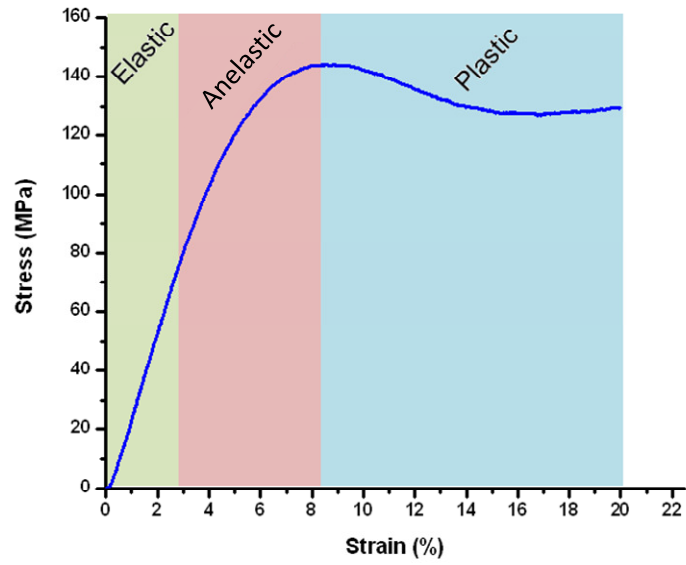


**Figure 9.** Uniaxial compression stress vs. strain plot.<sup>65</sup>

## **RESULTS PART I**

### **A MOLECULAR DYNAMICS APPROACH TO PREDICTING PROPERTIES OF CROSSLINKED AROMATIC POLYMERS**

#### **Introduction**

Molecular Dynamics (MD) simulations are a useful tool to visualize network architecture, the process of crosslinking, and molecular interactions. MD simulations also provide a powerful technique for predicting thermomechanical properties of polymers. In this regard, MD simulations represent an expedient, multiscale technique, connecting interactions and properties on the atomistic time and size scale to macroscale properties of the material.

Molecular dynamics simulations have further use as a multiscale technique when considering composite property prediction. Composite properties are predicted using a Finite Element Analysis (FEA), a technique which operates in the continuum using constitutive relations. FEA uses the physical properties of the individual components in a composite to calculate the ultimate properties of the composite. For example, in a matrix-fiber composite, FEA would combine the physical properties of the matrix with those of the fibers to calculate the properties of the fiber reinforced matrix composite. Using MD with FEA in a hierarchical or concurrent fashion creates a powerful simulation combination where the outputs of the molecular dynamics simulations (thermomechanical properties of polymers) become the inputs for finite element analysis. The ultimate goal is to design composites possessing a specific set of properties without having to complete the time-consuming and costly process of synthesizing the monomers, B-staging the matrix, incorporating the B-staged matrix into the fiber, curing the composite, and finally completing dozens of different material properties tests. This goal has not

yet been attained; however, we are able to predict matrix properties with steadily decreasing error.

In this research, atomistically explicit MD methods have been refined to continually improve the accuracy of simulations without substantially increasing the time or computing power needed to complete simulations. Increasing the accuracy and efficiency of MD has been accomplished through better understanding of the polymers involved, and specifically, an increased awareness of how chemical make-up and network architecture influence the simulations.

## **Objective**

This section provides a detailed description of the molecular dynamics simulation procedure and theory behind that procedure. Sections II and III of this report are based on the same general procedure and theory; however, we will adjust our approach to create more accurate simulations. Our reasoning for using MD simulations is twofold. First, we want to improve the accuracy of the simulations by comparing the simulated thermomechanical properties to experimentally obtained values and adjusting the simulation procedure where discrepancies are observed. Second, we want to use the simulations, where accurate, to understand the effect of the chemical and structural design of the network on thermomechanical properties. An example of chemical design is the introduction of additional sulfone or phenyl ring content, while network design could include a change in crosslink density. Even though some of the simulated properties may not exactly match experimental results, simulations giving values which are internally comparable are useful to show trends among polymers.

For the purpose of improving accuracy of simulations by comparison of the simulated properties to experimentally obtained properties, two amine / epoxy systems will be used: 3,3'-diaminodiphenyl sulfone (33DDS) / diglycidyl ether of bisphenol A (DGEBA) and 4,4'-diaminodiphenyl sulfone (44DDS) / DGEBA. The thermomechanical properties which will be compared are tensile modulus (E), shear modulus (G), glass transition temperature ( $T_g$ ), density ( $\rho$ ), and compression yield strain ( $\epsilon_y$ ). In addition to these properties, the simulations will report Poisson's ratio ( $\nu$ ), coefficient of thermal expansion in the glassy state ( $\alpha$ ), and the first invariant of the strain tensor ( $J_1$ ).

To examine the effect of chemical and structural design on network properties, the two base systems (33DDS/DGEBA and 44DDS/DGEBA) will be compared with a third system (22DDS/DGEBA) to study the effect of para vs. meta vs. ortho amine group positioning. 33DDS and 44DDS will also be modified to contain more sulfones and phenyl rings, additional meta linkages in the middle of the diamine, and higher and lower crosslink densities. The epoxy (DGEBA) will be kept the same across all simulations such that the effects of changes in the diamines can be selectively studied.

## **Materials**

3,3'-Diaminodiphenyl sulfone and 4,4'-diaminodiphenyl sulfone were purchased from Sigma Aldrich and used as received. Diglycidyl ether of bisphenol A was purchased under the tradename EPON 825 from Hexion and used as received. The DGEBA was cured with both the 44DDS and 33DDS to make polymers for the experimental physical testing.

The simulated systems consist of a diepoxy cured with multifunctional amines. The epoxy is kept the same across all simulations (DGEBA), while the amine is changed to observe

the effect on thermomechanical properties. The chemical structures for the amines and epoxy simulated in the section are shown in Figure 10.

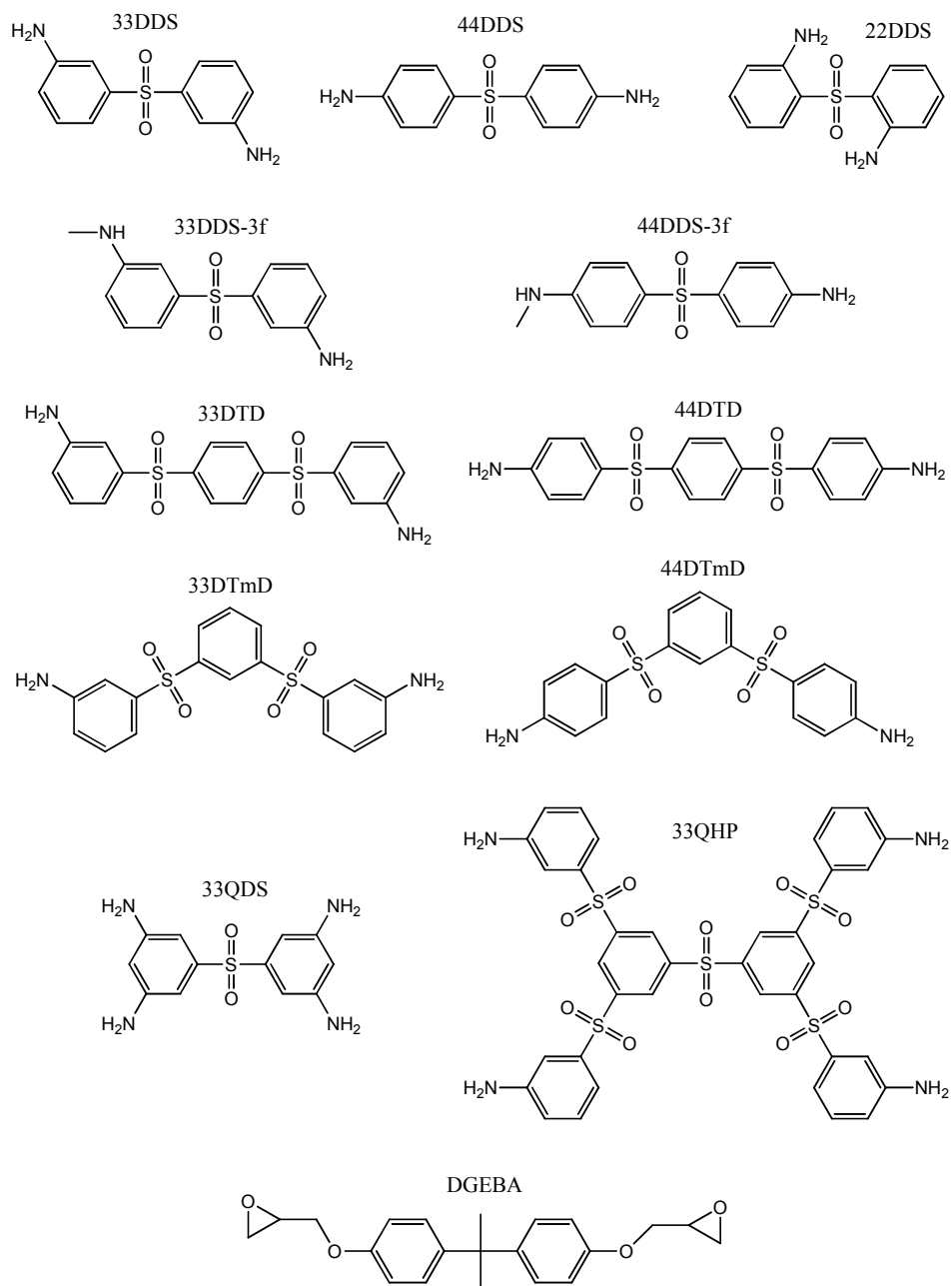


**Figure 10.** Simulated amines and epoxy.

Table 1 lists the chemical names for the amines and epoxy in the figure above. The center column lists the commonly used industrial name or a name derived from industry naming and is the name from which the abbreviations are taken. The column on the right gives the Chemdraw® name for each molecule. My naming system for amines was modeled from the industrial names for 3,3' and 4,4'-diaminodiphenyl sulfone.

**Table 1.** Abbreviations and Names for Amines and Epoxy Used in Simulations.

Abbrev.	Industry/Author naming system	Chemdraw® name
33DDS	3,3'-diaminodiphenyl sulfone	3,3'-sulfonyldianiline
44DDS	4,4'-diaminodiphenyl sulfone	4,4'-sulfonyldianiline
22DDS	2,2'-diaminodiphenyl sulfone	2,2'-sulfonyldianiline
33DTD	3,3'-diaminotriphenyl disulfone	3,3'-(1,4-phenylenedisulfonyl)dianiline
44DTD	4,4'-diaminotriphenyl disulfone	4,4'-(1,4-phenylenedisulfonyl)dianiline
33DTmD	3,3'-diaminotriphenyl meta-disulfone	3,3'-(1,3-phenylenedisulfonyl)dianiline
44DTmD	4,4'-diaminotriphenyl meta-disulfone	4,4'-(1,3-phenylenedisulfonyl)dianiline
33QDS	3,3',5,5'-quatraminodiphenyl sulfone	5,5'-sulfonylbis(benzene-1,3-diamine)
33QHP	3,3',3",3'''-quatraminohexaphenyl pentasulfone	3,3',3",3'''-(5,5'-sulfonylbis(benzenedisulfonyl))tetraaniline
DGEBA	Diglycidyl ether of Bisphenol A	2,2'-(((propane-2,2-diylbis(4,1-phenylene))bis(oxy))bis(methylene))bis(oxirane)

## Methods

### *Matrix Preparation*

To prepare 33DDS/DGEBA and 44DDS/DGEBA samples in the bulk, 33DDS and 44DDS must first be solubilized into DGEBA. 33DDS is fully solubilized at 110°C and 45 minutes, while 44DDS is dissolved at 125°C and 45 minutes. Both amines are solubilized using magnetic stirring and a vacuum to remove air and water which become defects in the cured networks. Once the amines are dissolved into DGEBA, the mixtures are poured into molds to create geometries needed for physical property determination, and the samples are cured. To

achieve cure without degradation, the 33DDS/DGEBA and 44DDS/DGEBA are cured for 5 hours at 125°C and 1 hour at 200°C.

### ***Instrumental Analysis***

Density is determined using the hydrostatic weighing method. By weighing a sample in and out of water, the Archimedes principle can be used to calculate density. A smooth matrix sample of approximate dimensions 10 X 10 X 4mm is weighed on an accurate balance. This same sample is then submerged in water and weighed. Density is calculated using Equation 5. The average of 5 samples is reported.

$$\text{density of body} = \frac{\text{weight of body}}{\text{weight of body} - \text{weight of immersed body}} * \text{density of water}$$

#### **Equation 5.** Density determination by hydrostatic weighing.

Dynamic mechanical analysis (DMA) is accomplished on a Thermal Analysis (TA) Q800® instrument using a tensile fixture. A strain of 0.05% and a frequency of 1Hz are used. Silicone molds used in DMA sample preparation create small rectangular strips, which have dimensions of approximately 5.0 X 1.7 X 61.0mm. TA Universal Analysis® software is used to analyze the DMA plots. Tensile modulus is determined as the storage modulus at 25°C and the T<sub>g</sub> is determined as the tanδ maximum. The average of three samples is reported.

Shear modulus is determined using a TA ARES rheometer. Silicone molds used in rheometry sample preparation create rectangles, which have dimensions of approximately 10.0 X 4.0 X 46.0mm. A strain of 0.05% and frequency of 6.28 rad/sec (1Hz) is used. The average of 4 samples is reported.

Differential scanning calorimetry (DSC) is accomplished on a TA Q200 instrument at a temperature ramp of 10°C per minute. An initial heating to >25°C above  $T_g$  is accomplished to clear thermal history, and a subsequent cooling and heating ramp are run for each sample.  $T_g$  is calculated using the ‘glass transition’ analysis function in TA’s Thermal Advantage software. For each sample, the second heating and cooling  $T_g$ s are averaged to give the reported  $T_g$  of that sample. The average of four samples is reported.

Compression yield strain is measured on an MTS 800 testing frame with a specially designed compression subpress according to ASTM D695. To obtain the precise cylindrical sample geometry necessary, samples are prepared in cylindrical Teflon molds. Once cured, the matrix cylinders are precisely lathed to a diameter of 0.50in. Then the cylinders are cut with a diamond edged saw to be 1.00 in. long and completely square (90° angles at the rim) to create a geometry in concordance with ASTM D695. The compression tests are run at a strain controlled compression rate of 0.05in./min. The average of two samples is reported.

### ***Molecular Dynamics Simulation Procedure***

All molecular dynamics calculations and simulations were accomplished in Accelrys Materials Studio 4.2® using the Condensed Phase Optimized Molecular Potentials for Atomistic Simulation Studies (COMPASS®) forcefield, group based cutoffs based on user assigned charge groups, and the “Medium” quality setting. The quality of the simulation is determined by four parameters: cutoff distance, spline width, buffer width, and relative dielectric. The cutoff distance determines the distance at which the nonbond forces (van der Waals and Coulombic interactions) will be included in the summation. The spline width specifies the size of the region within which non-bond interactions are splined from their full value to zero. The buffer width defines the distance beyond cutoff at which non-bond interactions are zero.<sup>lxxiv</sup> Finally, the

dielectric constant is adjusted relative to the permittivity of free space. The “Medium” quality summation sets the cutoff distance at 9.50Å, the spline width at 1.00Å, the buffer width at 0.50Å, and the relative dielectric at 1.00.

### ***Build seed and structures***

The molecules analyzed were built using Materials Studio’s Dendrimer function. The Dendrimer function starts with a Seed molecule and builds Structure molecules onto that Seed as prescribed by the user. The Seed and Structure molecules are essentially monomers. The user determines the chemical structure and reactive sites of the Seeds and Structures.

Materials Studio® cannot predict a chemical reaction, such as the ring opening of an epoxide by an amine, so the Seeds and Structures used need to combine in a way that yields a bonded epoxy-amine system. Additionally, in order to save computing time and ensure that dipoles are not broken at the summation cutoff, the calculations are completed using group based cutoffs instead of atom based cutoffs, meaning the software will not consider each atom individually when performing calculations. Instead, groups of bonded atoms with a net charge of 0 will be assigned as charge groups, and MD calculations will be performed considering these charge groups.

To (1) create a chemically correct network and (2) create a method by which non-bond forces may be summed without splitting dipoles, the amine and epoxy Seeds and Structures are built in a specific fashion. The epoxies are built with epoxide groups that have already been opened and are missing a methyl group, and the amines are built with two methyl groups bonded to each nitrogen atom (Figure 11). It may be noted that each opened epoxide is missing one methyl group because this group is included on the amine in order to make neutral charge groups. The H\* atoms present on both the modified epoxy and amine are hydrogen atoms that

function as connection points. When the modified epoxies and amines are bonded together, these H\* atoms will disappear to leave a chemically correct epoxy-amine bond.

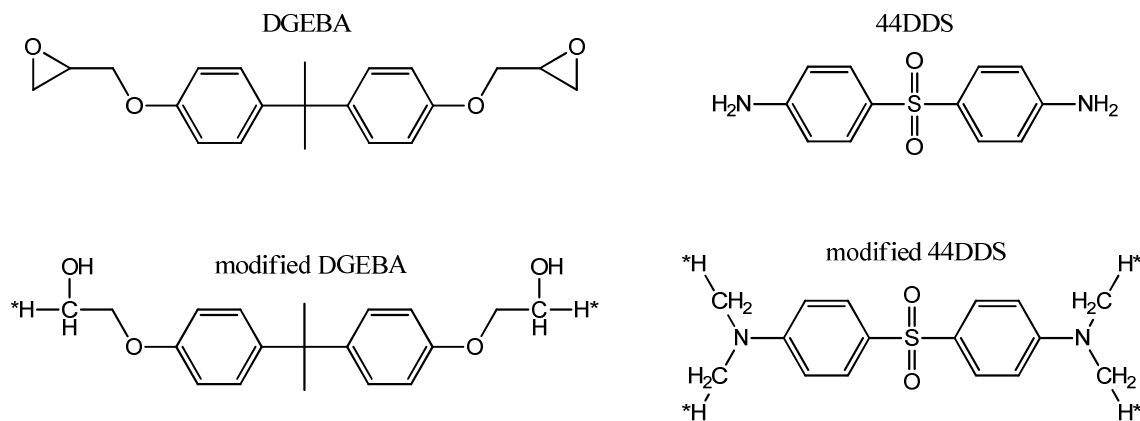


**Figure 11.** Modified DGEBA and 44DDS for use in MD simulations.

### ***Build polymer and amorphous cell***

For the purpose of this research, amines are always used as the Seed, and both amines and epoxies are used as Structures. The polymer is built in dendritic fashion, starting with an amine and adding first an epoxy, then an amine, then an epoxy, and so on. Dendrimers are built assuming full conversion of epoxies and amines until the dendrimer reaches ~3,500 atoms, at which point the appropriate number of epoxies or amines are added to balance the stoichiometry (2:1 epoxy:amine ratio). The dendrimers are relaxed using the Clean function to minimize some of the energy in the structure, mostly by setting the bonds to the appropriate angles and lengths.

Before any of the remaining calculations can be performed, a periodic cell must be created from the dendrimer. The periodic Amorphous Cell is necessary to overcome the problem of surface effects. Periodic boundary conditions define a quantity of material in three dimensional space; as atoms move and leave that space, replacements come in.<sup>lxv</sup> The

amorphous cell construction function is used to place a single dendrimer into 10 separate amorphous cells at a temperature of 298K. The density of the amorphous cell is ramped at 0.01g/cc to reach a final density of 0.4 g/cc. To optimize geometry and configuration of the amorphous cell, the maximum number of lookahead bonds (6) and lookahead configurations (48) are used. Ring catenations are identified, and the amorphous cell construction is restarted if ring catenation is found. A total of 1,000 dynamics steps are performed at the end of the construction.

### ***Minimization and equilibration***

The amorphous cell construction will attempt to return ten amorphous cells as specified. However, some of these jobs may fail for energetic reasons. Of the amorphous structures created, the three with the lowest final total energy are chosen to be further analyzed. Three structures are chosen to obtain statistically viable data and average out some of the error. These three structures are minimized using 2,500 iterations with the Discover Minimizer employing the Smart Minimizer method. The Smart Minimizer uses a combination of the steepest descent, conjugate gradient, and Newton energy minimization processes. To determine whether the structure is appropriately minimized, the maximum derivative of the energy is calculated. The closer the maximum derivative is to 0, the closer the structure is to the bottom of the energy well, meaning the energy has been effectively minimized. The minimization process should yield a maximum derivative of  $\sim 10$ . If the maximum derivative is above 15, the structure is minimized again. For the minimization, both van der Waals and Coulombic forces are considered.

The three amorphous cells are further minimized using a previously written anneal script donated by Boeing Research and Technology. The annealing procedure uses a series of alternating NPT and NVT statistical mechanical ensembles that start at 650K and reduce in

temperature by 150K stepwise to 300K. An NPT simulation keeps moles, pressure, and temperature constant over the course of the simulation while allowing other factors such as volume to change, while an NVT run keeps moles, volume, and temperature constant while allowing pressure to change. The anneal process should drastically reduce the energy in the amorphous cell and yield a system close to its energy minimum. The maximum derivative after this step must be less than 0.001. If the maximum derivative is above 0.001, the anneal process must be repeated. The anneal process uses the Andersen thermostat and barostat.

### ***Calculation of molecular trajectories***

The output file from the anneal process is taken through another NPT simulation to obtain trajectories through time. In this NPT process, the three amorphous cells are individually run through a series of 250,000 time steps of 1fs and a dynamics time of 250ps. In other words, frames were captured every 2.5ps for a total time of 0.25ns. To cut down on the excessive amount of data this yields, a cell at each of the 250,000 steps is not saved. Instead, a frame is saved every 2,500 steps to give a total of 100 frames. The NPT is completed at atmospheric temperature and pressure using the Andersen thermostat and the Berendsen barostat.

### ***Analysis of Molecular Trajectories***

After the NPT trajectories are completed, a series of tests are run to determine the physical properties of the material. Tensile modulus (E), shear modulus (G), and Poisson's ratio ( $\nu$ ) are all calculated on the output of the NPT simulation using the Discover Static Elastic Property Analysis tool. The last 10 frames of each of the three trajectories are analyzed, and the values obtained from the tests are averaged. The values for the three different trajectories are then averaged.

To calculate E, G, and  $\nu$ , a total of twelve loading experiments are performed, in which six shear processes are accomplished and uniaxial tensile and compression stresses are applied stepwise along the x, y, or z directions.<sup>lxxvi</sup> For each loading direction, constant stress dynamics is performed as a series of up to 10 stages, each having a 1ps duration. At the end of each stage, values of the internal stress tensor and of the strain tensor are recorded. Before continuing on to the next stage, the applied (external) stress is incremented by a predefined amount (0.05 GPa, or 500 bar). An experiment for any given pulling direction stops when the strain in that direction exceeds 0.2, or when all 10 stages have been completed, whichever occurs first. When all three loading experiments are completed, the recorded stress-strain data are averaged for all three directions.

In isotropic systems, only two independent coefficients, referred to as Lamé coefficients, are needed to fully describe the stress-strain behavior. The stiffness matrix resulting from the constant stress dynamics experiment is shown in Equation 6. Tensile modulus and Poisson's ratio are calculated from a least-squares fit to the average tensile stress vs. strain data and the average lateral strain vs. tensile strain data generated by the program. Since these are isotropic systems, Young's modulus and Poisson's ratio can be written in terms of the Lamé coefficients, shown in equations 7 and 8, respectively. The shear modulus is calculated directly from the stiffness matrix (Equations 6 and 9).

$\lambda+2\mu$	$\Lambda$	$\lambda$	0	0	0
$\lambda$	$\lambda+2\mu$	$\lambda$	0	0	0
$\lambda$	$\Lambda$	$\lambda+2\mu$	0	0	0
0	0	0	$\mu$	0	0
0	0	0	0	$\mu$	0
0	0	0	0	0	$\mu$

**Equation 6.** Stiffness matrix with Lamé coefficients.

$$E = \mu * \frac{3\lambda + 2\mu}{\lambda + \lambda}$$

**Equation 7.** Young's modulus expressed in terms of the Lamé coefficients.

$$\nu = \frac{\lambda}{2(\mu + \lambda)}$$

**Equation 8.** Poisson's ratio expressed in terms of Lamé coefficients.

$$G = \mu$$

**Equation 9.** Shear modulus calculated from Lamé coefficients.

Compression yield strain is calculated using a stress controlled compression script written for Materials Studio 4.2 by Boeing. Uniaxial loads are placed in the x, y, and z directions in separate simulations. Twenty uniaxial loads are applied to each cell starting at 0kPa and increasing up to 0.275kPa. The cell dimensions are recorded after each load, and the corresponding axial strains are calculated from the average of the uniaxial compressions in the x, y, and z directions. A stress vs. strain curve is approximated by fitting the data to a second order polynomial. The compression yield strain is approximated from the maximum of the second order polynomial curve. Von Mises strain ( $\epsilon_{vm}$ ) is approximated by multiplying the compression yield strain ( $\epsilon_y$ ) by 1.5 (Equation 10).

$$\epsilon_{vm} = 1.5 * \epsilon_y$$

**Equation 10.** Approximation of von Mises strain.

To determine CTE ( $\alpha$ ), glass transition temperature ( $T_g$ ), density ( $\rho$ ), and the first invariant of the strain tensor ( $J_1$ ), the temperature cycle in Amorphous Cell Protocols is employed. The pressure is kept constant at 0.0001GPa (1bar), the stage duration is set to the maximum of 40,000fs, and the averaging period is also maximized at 20,000fs. The temperature simulation cycles the temperature from 800K to 100K and back to 800K in these 40,000 time steps. Since a theoretical V vs. T plot should be obtained infinitely slowly, the values for the heating and cooling cycles are averaged to give an approximation of a slow process.

With the pressure held constant at atmospheric pressure, the volume will change as the temperature is cycled. Volume, temperature, and density data are recorded every 25K during heating and cooling. The density at room temperature for the heating and cooling cycles is averaged to yield the ambient condition density for the structure. The temperature and volume data are used to create heating and cooling volume vs. temperature plots. An example plot is shown in Figure 12.

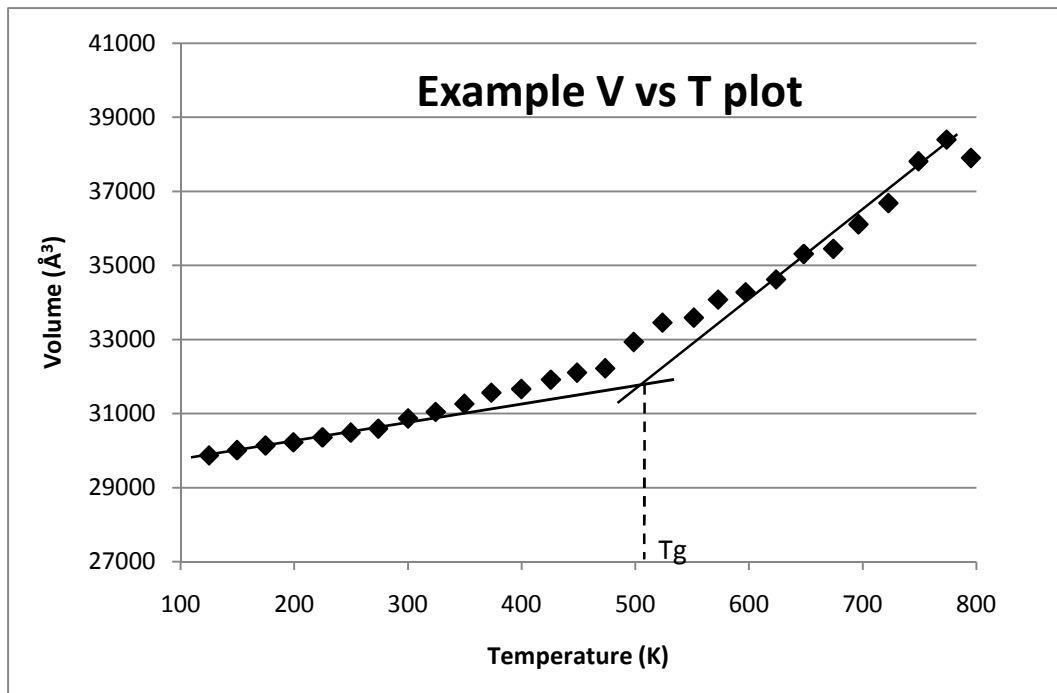


Figure 12. Example volume vs. temperature plot

The slope of the V vs. T line at temperatures above  $T_g$  gives the rubbery CTE, while the slope of the plot at temperatures below  $T_g$  gives the glassy CTE. The slope is calculated between 100K and 300K to determine the glassy CTE and between 600K and 800K to determine the rubbery CTE. The  $T_g$  is determined by extrapolating the two linear curves from which glassy and rubbery CTEs were calculated until these curves intersect. The temperature at the intersection is determined as the  $T_g$ . Finally,  $J_1$  is calculated from the average simulated glassy CTE and  $T_g$  data according to Equation 11.

$$J_1 = [\alpha_g(T_g - 273) + 1]^3 - 1$$

**Equation 11.** Determination of  $J_1$ .

### ***Accuracy of Simulations***

To determine the accuracy of simulations, experimental data for 33DDS/DGEBA and 44DDS/DGEBA are compared to simulated values. Table 2.2 details the five thermomechanical properties experimentally obtained, tensile modulus (E), shear modulus (G), glass transition temperature ( $T_g$ ), density ( $\rho$ ), and compression yield strain ( $\epsilon_y$ ). Multiple trials for each experiment were completed, and the average values and standard deviations are reported above the raw data.

By comparing 33DDS to 44DDS, we can observe which simulated properties give accurate values, which simulations show correct trends for comparative purposes, and which simulation procedures need to be altered to yield more accurate results. The 33DDS vs. 44DDS comparison also shows the effect of meta substitution in the polymer backbone on thermomechanical properties of chemically isomeric systems. The experimental data show that tensile modulus, shear modulus, and density are statistically higher in the 33DDS/DGEBA

matrix than the 44DDS/DGEBA matrix; however, the glass transition temperature and compression yield strain of 44DDS/DGEBA are significantly higher than the corresponding values for 33DDS/DGEBA.

**Table 2.** Experimental Properties of 44DDS/DGEBA and 33DDS/DGEBA

System	E, GPa	G, GPa	T <sub>g</sub> , °C DSC	T <sub>g</sub> , °C DMA	ρ, gm/cc	ε <sub>y</sub>
<b>44DDS/DGEBA</b>	<b>2.19</b>	<b>0.71</b>	<b>217</b>	<b>220</b>	<b>1.23</b>	<b>0.110</b>
<i>Std. Dev.</i>	<i>0.31</i>	<i>0.05</i>	<i>0.4</i>	<i>1</i>	<i>0.001</i>	<i>0.002</i>
Trial 1	1.85	0.74	217	220	1.24	0.112
Trial 2	2.26	0.70	218	220	1.23	0.109
Trial 3	2.45	0.65	217	221	1.23	
Trial 4		0.75	217		1.23	
Trial 5					1.23	
<b>33DDS/DGEBA</b>	<b>2.60</b>	<b>0.76</b>	<b>173</b>	<b>186</b>	<b>1.24</b>	<b>0.095</b>
<i>Std. Dev.</i>	<i>0.23</i>	<i>0.02</i>	<i>0.3</i>	<i>1</i>	<i>0.003</i>	<i>0.001</i>
Trial 1	2.45	0.73	174	186	1.23	0.094
Trial 2	2.48	0.78	174	187	1.23	0.096
Trial 3	2.86	0.76	174	186	1.24	
Trial 4		0.77	173		1.24	
Trial 5					1.24	

The first set of simulations compares 44DDS to 33DDS and will be used to demonstrate the failures and successes of the simulations in accurately predicting properties and showing trends. Tri-functional versions of the amines are simulated to observe the effect of crosslink density on properties. The structures for the four amines used and the epoxy, DGEBA, are given in Figure 13.

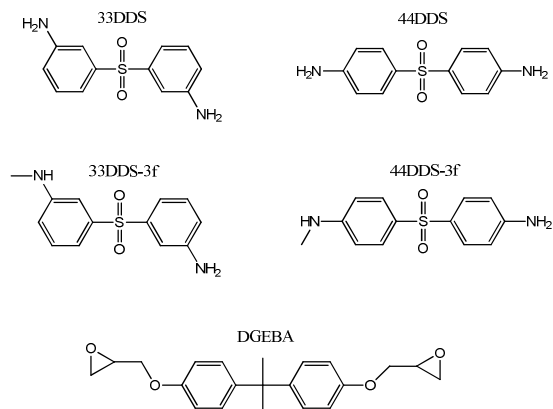


**Figure 13.** Structures of 3f and 4f 33DDS and 44DDS and DGEBA.

Table 3 gives the simulation data for these four epoxy systems. All thermomechanical properties are simulated in triplicate for each system, and the average values and standard deviations are recorded above the three trials for each system.

**Table 3.** Simulated Properties for 33DDS/DGEBA and 44DDS/DGEBA

System	E, GPa	G, GPa	$\nu$	$\alpha$ , in/inF $\times 10^{-6}$	$T_g$ , °C	$\rho$ , g/cc	$J_1$	$\epsilon_y$
<b>44DDS</b>	<b>5.07</b>	<b>1.92</b>	<b>0.322</b>	<b>32.4</b>	<b>202</b>	<b>1.196</b>	<b>0.031</b>	<b>0.14</b>
Std. Dev.:	0.18	0.08	0.007	0.7	12	0.002	0.004	0.01
Trial 1	5.26	2.00	0.314	33.2	214	1.198	0.035	0.13
Trial 2	4.91	1.85	0.326	32.2	201	1.195	0.031	0.15
Trial 3	5.04	1.90	0.326	31.8	191	1.195	0.028	0.14
<b>33DDS</b>	<b>4.42</b>	<b>1.68</b>	<b>0.317</b>	<b>35.1</b>	<b>222</b>	<b>1.193</b>	<b>0.038</b>	<b>0.17</b>
Std. Dev.:	0.54	0.20	0.010	3.3	7	0.002	0.003	0.02
Trial 1	3.91	1.48	0.318	38.8	223	1.194	0.042	0.18
Trial 2	4.98	1.88	0.327	32.5	229	1.191	0.036	0.15
Trial 3	4.37	1.68	0.307	34.0	215	1.195	0.036	0.19
<b>3f-44DDS</b>	<b>4.35</b>	<b>1.64</b>	<b>0.327</b>	<b>37.8</b>	<b>231</b>	<b>1.194</b>	<b>0.044</b>	<b>0.15</b>
Std. Dev.:	0.35	0.14	0.004	3.2	30	0.010	0.009	0.01
Trial 1	4.32	1.62	0.330	35.9	212	1.203	0.040	0.16
Trial 2	4.72	1.78	0.323	35.9	216	1.194	0.038	0.14
Trial 3	4.02	1.51	0.329	41.5	265	1.184	0.055	0.14
<b>3f-33DDS</b>	<b>4.21</b>	<b>1.57</b>	<b>0.344</b>	<b>35.2</b>	<b>194</b>	<b>1.203</b>	<b>0.033</b>	<b>0.14</b>
Std. Dev.:	0.30	0.13	0.017	0.7	19	0.001	0.004	0.01
Trial 1	3.90	1.44	0.358	35.8	190	1.203	0.032	0.15
Trial 2	4.50	1.70	0.325	34.5	177	1.202	0.029	0.13
Trial 3	4.24	1.57	0.349	35.4	215	1.203	0.037	0.15

Obtaining accurate densities is considered the first step in determining the validity of molecular dynamics simulations. If the amorphous cell is not relaxed into a structure that possesses a density close to the true density of the material, there is not a good chance the simulations are accurate. The experimental densities for 44DDS/DGEBA and 33DDS/DGEBA are 1.233 and 1.236g/cc, respectively. The simulated densities were a little lower at 1.196 and 1.193g/cc, respectively. This difference in density is not large enough to assume that the simulations are invalid, but it indicates the possibility that the structures did not reach a fully relaxed conformation. The simulations for the 3 functional amines also gave densities a bit low; however, at least these simulations produced the correct trend: 33DDS/DGEBA having a greater density than 44DDS/DGEBA.

The simulated values for tensile and shear moduli do not show agreement with the experimental data. Firstly, the experimental values are significantly lower than the simulated values. In part, this is explained by the perfect nature of the test specimens in the simulation compared to the experimental test specimens, which possess microscopic defects such as bubbles, voids, microcracks, etc. The larger error is that the simulation fails to show the correct trend between the meta and para amine. Physical properties determined through experimentation clearly show that 33DDS possesses higher E and G than 44DDS. The tri-functional amines show values closer to the experimentally determined values, but the trend is wrong once again.

As is the case with modulus, the simulated  $T_g$ s for 33DDS and 44DDS do not give a good estimate of  $T_g$ . As determined by DSC and DMA, the  $T_g$  of 33DDS/DGEBA should be in the range of 170-190°C, and the  $T_g$  of 44DDS/DGEBA in the range of 210-230°C. The simulated values predict a  $T_g$  of 222°C for 33DDS/DGEBA and a  $T_g$  of 202°C for 44DDS. Interestingly, the tri-functional amines give much more accurate values for the  $T_g$ s of 33DDS/DGEBA and

44DDS/DGEBA of 194°C and 231°C, respectively. This result is either indicative of a polymer build that more accurately represents reality when incomplete crosslinking is assumed or a simulation procedure for  $T_g$  with too much error. Both of these concerns are addressed in latter simulations summarized in Sections II and III.

The first invariant of the strain tensor,  $J_1$ , gives a measure of the elastic response of the polymer, while von Mises strain  $\epsilon_{vm}$  gives an approximation of the distortional ability of the matrix.  $J_1$  is approximated from the same simulation as  $T_g$ , and the same trends are observed: systems with high  $T_g$ s also possess high  $J_1$ s. We have not determined the  $J_1$  by means of experimental testing; however, since simulated  $J_1$  values came from the same simulation as the  $T_g$ , they are likely just as flawed as the simulated  $T_g$ s. If a simulation procedure that more accurately predict  $T_g$  can be developed, more confidence could be placed in the simulated  $J_1$  values.

The compression strain at yield,  $\epsilon_y$ , is used to estimate  $\epsilon_{vm}$ . Based on failure theory, increasing the distortional ability of resins is believed to be integral to increasing the failure properties of composites. Before starting this work, our hypothesis was that meta-substituted amines would provide kinks in the backbone that would increase the distortional capability by lowering activation energy for molecular level rearrangements. The simulated results provide support for this hypothesis by showing that the 33DDS matrix possesses a substantially higher compression yield strain than the 44DDS matrix. However, the opposite trend is seen in the experimental data. This result not only debunked our hypothesis, but it also showed a limitation of the simulation procedure.

### Effect of Chemical and Structural Design of the Network

In addition to the previous four amines studied, an additional seven amines are combined with DGEBA, and their properties are simulated (Figure 14). The structures in Figure 2.5 are chosen in order to study the effects of specific variables in molecular structure on simulated material properties, including, crosslink density, sulfone and aromatic content, and the effect of the amine group's position on the ring (para vs. meta vs. ortho). These simulated results are summarized in Table 4

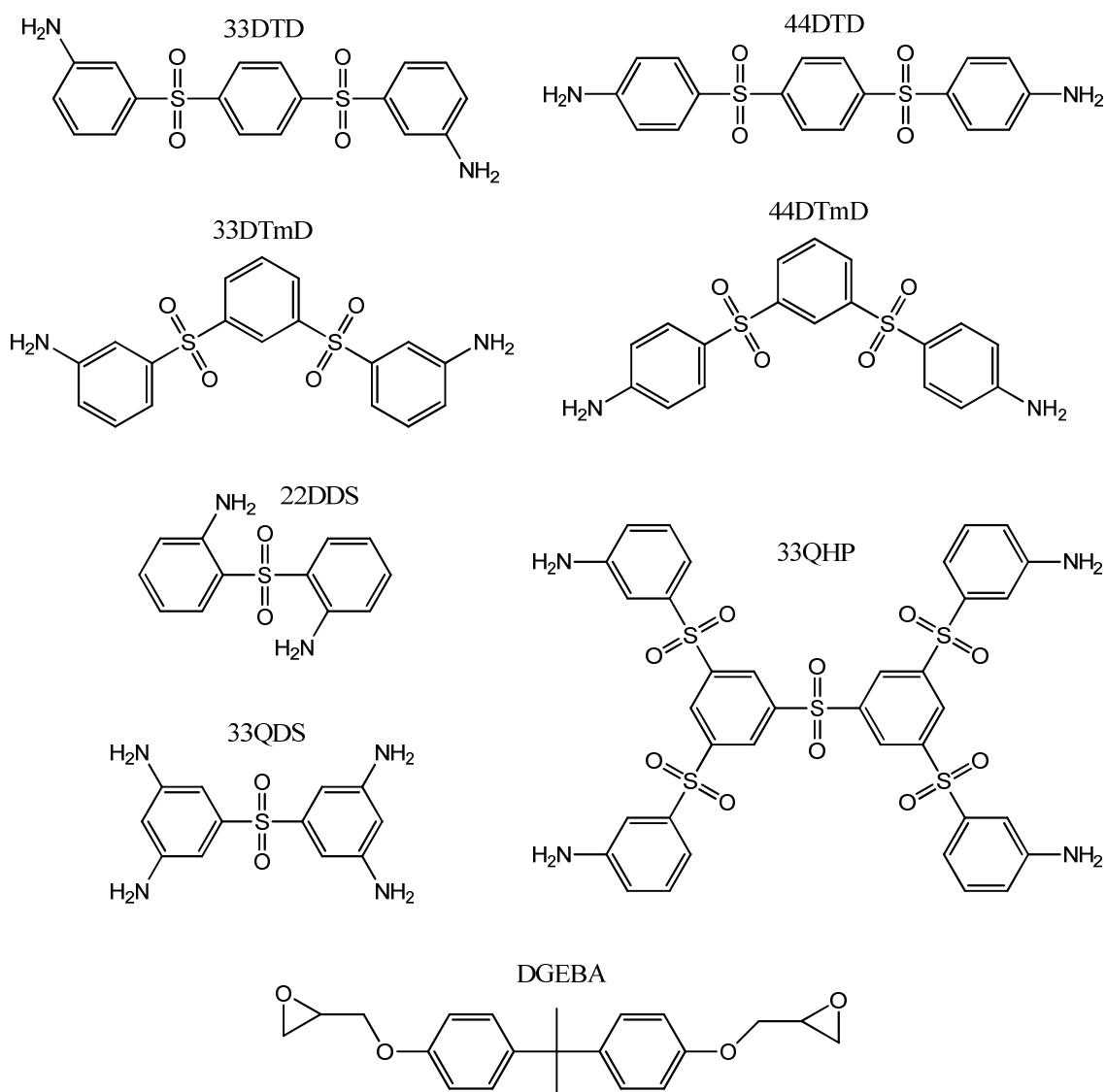


**Figure 14.** Amines simulated to determine effect of chemistry and structure of the network.

**Table 4.** MD Simulation Values for All Amines with DGEBA

System	E, GPa	G, GPa	$\nu$	$\alpha$ , in/inF $\times 10^{-6}$	$T_g$ , °C	$\rho$ , g/cc	$J_1$	$\epsilon_y$
33-DDS	4.71	1.77	0.330	31.7	197	1.200	0.030	0.17
44-DDS	5.07	1.92	0.324	32.9	202	1.201	0.032	0.14
33-DDS (3f)	4.54	1.71	0.333	31.4	185	1.207	0.028	0.14
44-DDS (3f)	4.76	1.80	0.325	33.1	213	1.202	0.035	0.15
22-DDS	4.85	1.85	0.315	34.4	171	1.195	0.028	0.14
33-DTD	4.17	1.54	0.351	31.5	183	1.220	0.027	0.13
44-DTD	4.03	1.52	0.323	35.1	188	1.222	0.031	0.12
33-DTmD	4.37	1.63	0.336	33.5	165	1.219	0.025	0.13
44-DTmD	4.28	1.59	0.342	33.2	184	1.229	0.030	0.14
33-QDS	4.65	1.74	0.332	33.4	161	1.179	0.025	0.11
33-QHP	4.88	1.84	0.327	33.1	179	1.229	0.028	0.065

### ***Crosslink Density***

To study the effect of crosslink density, 33DDS and 44DDS are compared to their tri-functional counterparts, 33DDS-3f and 44DDS-3f. As discussed previously, the tri-functional amines give results more commensurate with experimental findings (Table 2.2). 33DDS is also compared to 33QDS, the octa-functional equivalent of 33DDS. As expected, the higher crosslinked structure possesses a significantly decreased  $\epsilon_y$ . Somewhat unexpectedly, it also shows decreased tensile and shear moduli,  $T_g$ , and  $J_1$ .

### ***Sulfone and Aromatic Content***

33DDS and 44DDS are compared to 33DTD and 44DTD, respectively, to show the impact of additional spacer components (sulfones and phenyl rings) between the amines. The addition of sulfones and phenyl rings between amine groups by necessity increases the molecular weight between crosslinks, which decreases the crosslink density. Unfortunately for the purposes of this study, the effect of the change in crosslink density cannot be separated from the effect of additional sulfone groups and phenyl rings. The 33DTD and 44DTD show decreases in E, G,  $T_g$ , and  $\epsilon_y$  when compared to 33DDS and 44DDS, respectively. It is interesting to see that increasing sulfone content and aromaticity created a decline in all the properties.

33QHP and 33QDS can also be compared to study the effect of sulfone and aromatic content. In this case, the increased aromaticity and sulfone content create a polymer that has greater Young's modulus, shear modulus, and  $T_g$  and a lower compression yield strain. These trends indicate a polymer that is more rigid and possesses less distortional capability.

#### ***Para vs Meta vs Ortho Substitution***

22DDS, 33DDS, and 44DDS can all be compared to show the effects of ortho vs meta vs para substitution of the amine. In this comparison, the 33DDS shows increased  $\epsilon_y$ , indicating superior distortional capability. 33DTD and 44DTD can be compared to 33DTmD and 44DTmD, respectively, to determine the effect of meta substitution in the middle of the diamine. As expected, when the middle phenyl group is bonded in the meta as opposed to the para position, the  $\epsilon_y$  rises, connecting the presence of meta substitution with distortional capability (Table 2.4). The internal meta substitution also decreases  $T_g$  and increases E and G moderately.

Although the fully crosslinked 33DDS and 44DDS show the opposite trend to experimental compression yield data, the tri-functional 33DDS and 44DDS show the correct trend. In fact, across all thermomechanical properties, the tri-functional 33DDS and 44DDS gave simulated values more commensurate with experimentally determined results than the fully crosslinked 33DDS and 44DDS. This result shows the error introduced into simulations by the assumption of 100% conversion. Furthermore, this result implies experimental matrices (i.e., real polymers, not simulated polymers) possess a substantial amount of unreacted secondary amines. This is a significant piece of evidence in the debate over the percent crosslinking in thermoset matrices due to the difficulty in studying these systems spectroscopically.

Studying the effect of structural and chemical design on network properties shows some interesting trends. However, due to the inconsistencies seen in the comparison between 33DDS

and 44DDS simulated vs. experimental data using this simulation procedure, it is difficult to draw too many conclusions when only simulated values are compared. Furthermore, none of the simulated materials shows values significantly greater than 33DDS and 44DDS in the majority of thermomechanical properties, which decreases their appeal for synthesis and experimental testing. In order to make firm conclusions about the effects of structural and chemical design on network properties, a more accurate simulation procedure must be proven.

## **RESULTS PART II**

### **A MOLECULAR DYNAMICS APPROACH TO PREDICTING PROPERTIES OF CROSSLINKED AROMATIC POLYMERS**

#### **Objective**

The second chapter closely follows the objectives of the first chapter, and contains two primary objectives. The first objective is to employ a simulation procedure, which has been revised using the lessons learned in the Chapter I, to accomplish simulations more commensurate with experimental results for 33DDS/DGEBA and 44DDS/DGEBA. Once again simulation and experimental data are compared to determine for which physical properties the simulation procedure provides accurate values or trends and for which properties the simulation procedure needs to be further revised.

Secondly, simulations are accomplished to study the effect on thermomechanical properties of two interesting nano-modifiers bonded into a 33DDS/DGEBA matrix at varying weight percents. The first modifier is polyhedral oligomeric silsesquioxane (POSS) which is incorporated into the matrix by a single amine and possesses methyl groups on its other seven corners to help with solubilization. Figure 15 shows the Materials Studio structure of the POSS bonded to two DGEBA molecules. For simulations, the POSS/DGEBA structure is bonded into a 33DDS/DGEBA matrix to give different percent weights POSS. This procedure simulates ideal reaction of POSS into a 33DDS/DGEBA matrix as shown in Figure 16. The results of these simulations provide data about the effect on physical properties of bulky pendant groups bonded into the matrix.

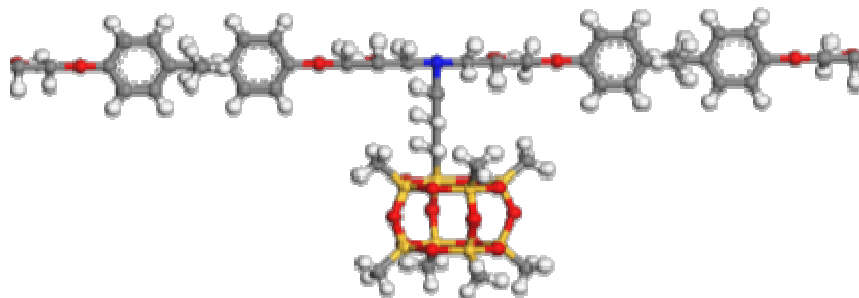


**Figure 15.** Structure for POSS/DGEBA.

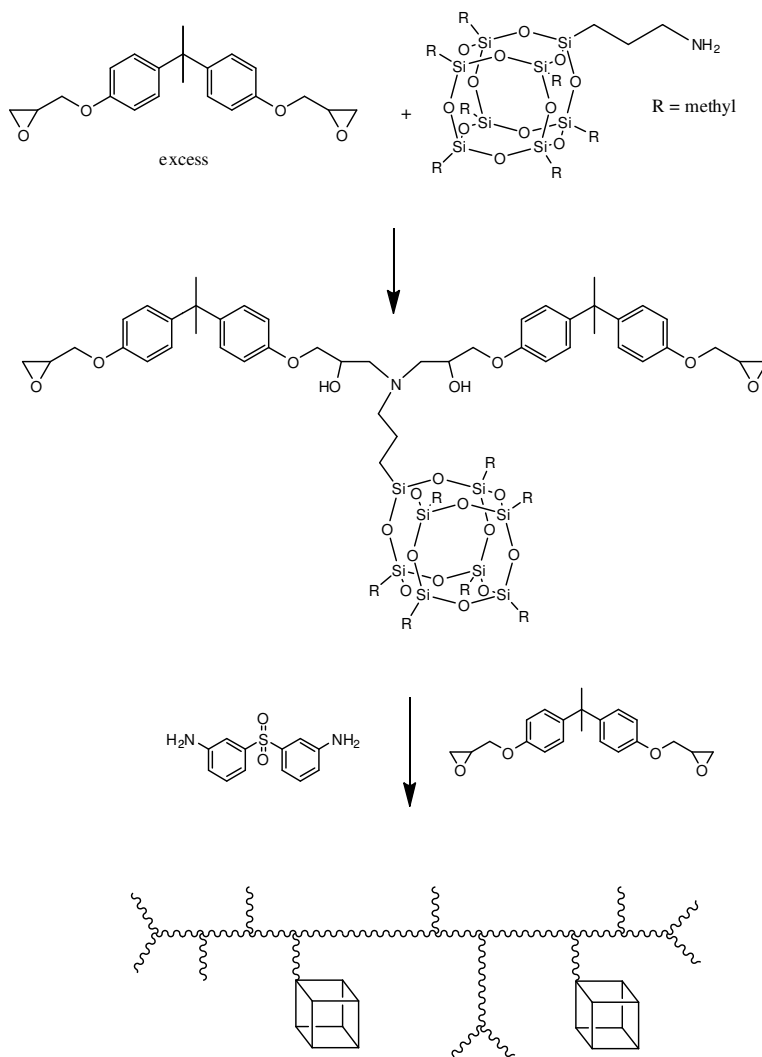


**Figure 16.** Simulated synthesis procedure for making dispersed POSS/33DDS/DGEBA.

The second modifier is a fluorinated pyrene, which has also been bonded into the matrix by an amine. Whereas the POSS molecule is a real molecule that can be synthesized and incorporated into epoxy matrices for evaluation, the F-pyrene is simulated to determine whether the POSS has special properties or will act in the same way as another bulky pendant group. The fluorines are added to make the pyrene less hydrophilic and therefore more capable of pervading free volume. This comparison will help determine whether the mechanism of nano-inclusions by pendant bulky groups is dependent upon the amount of free volume the bulky group creates. Figure 17 shows the Materials Studio structure for the F-pyrene/DGEBA, and Figure 18 shows the synthetic procedure this simulation models.

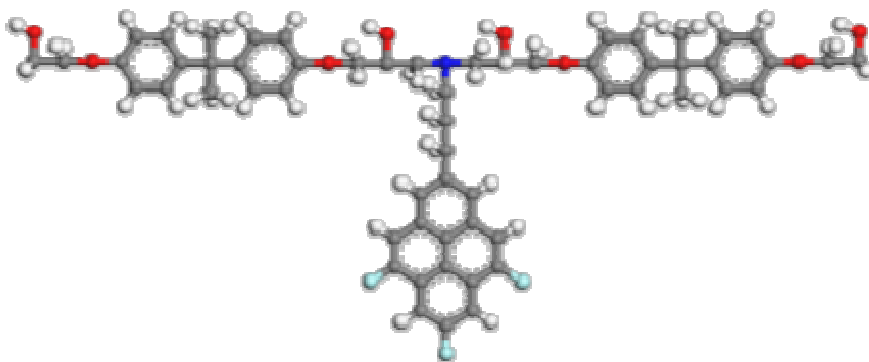


**Figure 17.** Structure for F-pyrene/DGEBA.

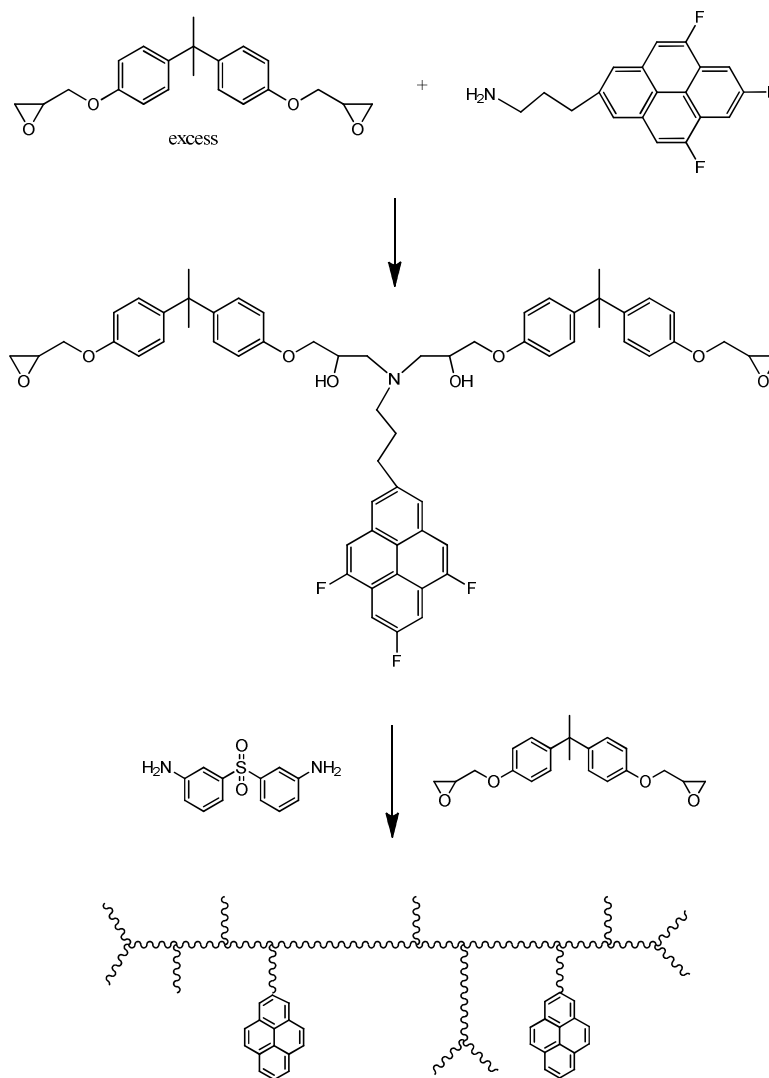


**Figure 18.** Simulated synthesis procedure for making dispersed F-pyrene/ 33DDS/DGEBA.

### ***MD Simulation Procedure***

To reduce some of the error in simulations and create more accurate models, the second round of simulations was accomplished with the same basic method described in the previous chapter, but with a few alterations. First, molecular dynamics calculations were completed in an updated version of Accelrys' software, Materials Studio 4.4. The Condensed Phase Optimized

Molecular Potentials for Atomistic Simulation Studies (COMPASS) forcefield and group-based cutoffs based on user assigned charge groups were still used. The quality used for most of the simulations is still “Medium,” but this is increased to “Fine” for the elastic property determination. The “Fine” quality summation sets the cutoff distance at 12.50Å, the spline width at 3.00Å, the buffer width at 1.00Å, and the relative dielectric at 1.00.

### ***Build seed and structures.***

The Seeds and Structures are built in exactly the same way as described in Section I.

### ***Build polymer and amorphous cell***

The dendrimer build and amorphous cell construction are accomplished with the same procedure used in Section I, with the one alteration that dendrimers are built to ~5,000 atoms as opposed to ~3,500 atoms.

### ***Minimization and equilibration***

Minimization, annealing, and equilibration processes are carried out in exactly the same manner as reported in Section I.

### ***Calculation of molecular trajectories***

The calculation of molecular trajectories is completed in the same manner as stated in Section I.

### ***Analysis of molecular trajectories***

Tensile modulus (E), shear modulus (G), and Poisson’s ratio ( $\nu$ ) are all calculated using the same procedure as recorded in Chapter I, but using the “Fine” quality setting. Compression

analysis was completed using the same stress controlled compression script obtained from Boeing.

To determine CTE ( $\alpha$ ), glass transition temperature ( $T_g$ ), density ( $\rho$ ), and the first invariant of the strain tensor ( $J_1$ ), the temperature cycle in Amorphous Cell Protocols is still employed; however, the process is changed to maximize the number of dynamics steps, thus removing error. In order to accomplish this, the temperature cycle is broken up into two steps: a heating simulation from 100K to 800K and a cooling simulation from 800K to 100K. Before starting the heating/cooling ramps, additional NPTs are run to equilibrate each cell at both 100K (for heating) and 800K (for cooling). These NPTs are completed at 0.0001GPa (1bar) using 25,000 time steps of 1fs, giving a total dynamics time of 25ps. The final structure generated in this NPT will be the structure for the heating and cooling simulations. In the temperature cycle, one simulation cools the 800K structure down to 100K, while another simulation heats the 100K structure up to 800K. For each process, the number of stages is increased to 71, which will give a simulated volume and density every 10K between 100K and 800K, the stage duration is increased to 100,000fs, and the averaging period is increased to 50,000fs. The number of data points in the V vs. T curve is increased from 28 as seen in Section I to 70 as seen in Figure 19. Glassy and rubbery CTEs,  $T_g$ , and  $J_1$  were all calculated in the same manner as reported in Chapter I. Figure 19 shows that despite the more rigorous simulation procedure, the V vs. T curve still fails to show a distinct change in slope at  $T_g$ .

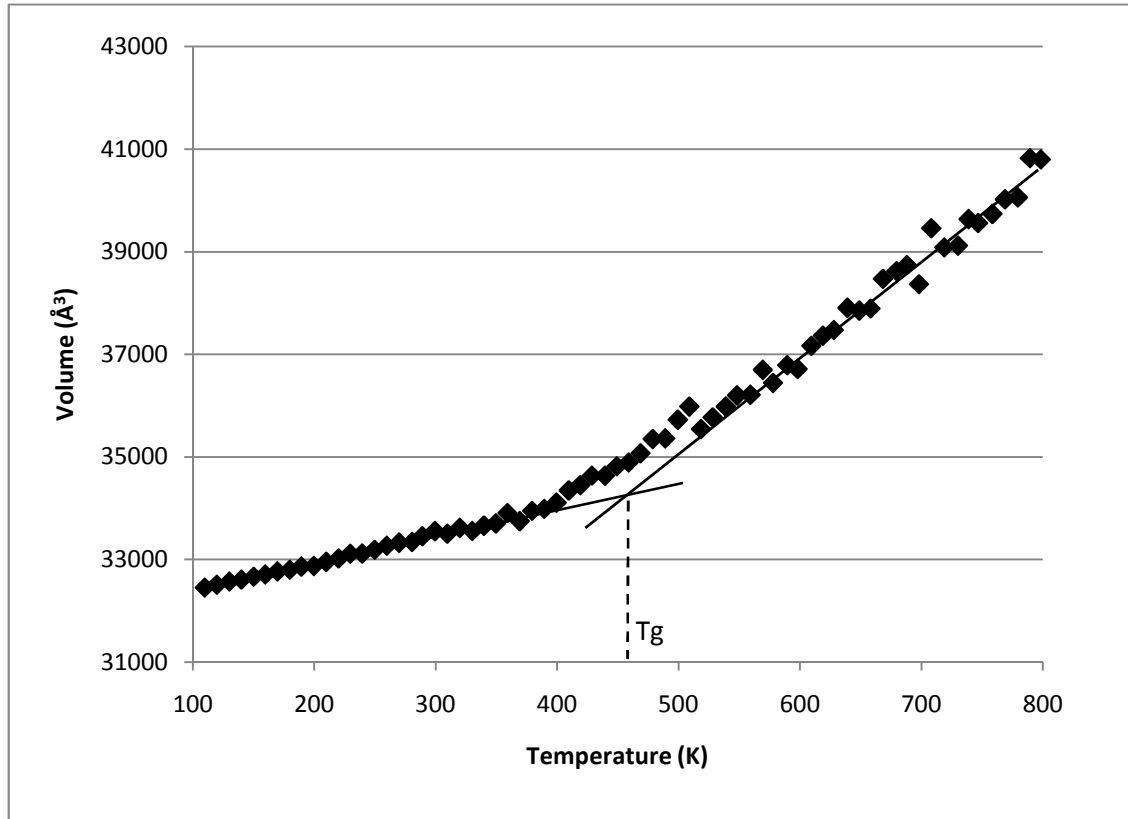


**Figure 19.** Example volume vs. temperature plot, more rigorous cycle

Similar to Section I, to determine the accuracy of simulations, experimental data for 33DDS/DGEBA and 44DDS/DGEBA are compared to simulated values. Table 5 details the five thermomechanical properties experimentally obtained, tensile modulus ( $E$ ), shear modulus ( $G$ ), glass transition temperature ( $T_g$ ), density ( $\rho$ ), and compression yield strain ( $\epsilon_y$ ). Multiple trials for each experiment were completed, and the average values and standard deviations are reported above the raw data.

**Table 5.** Experimental Properties of 44DDS/DGEBA and 33DDS/DGEBA

System	E, GPa	G, GPa	T <sub>g</sub> , °C DSC	T <sub>g</sub> , °C DMA	ρ, gm/cc	ε <sub>y</sub>
<b>44DDS/DGEBA</b>	<b>2.19</b>	<b>0.71</b>	<b>217</b>	<b>220</b>	<b>1.23</b>	<b>0.110</b>
<i>Std. Dev.</i>	<i>0.31</i>	<i>0.05</i>	<i>0.4</i>	<i>1</i>	<i>0.001</i>	<i>0.002</i>
Trial 1	1.85	0.74	217	220	1.24	0.112
Trial 2	2.26	0.70	218	220	1.23	0.109
Trial 3	2.45	0.65	217	221	1.23	
Trial 4		0.75	217		1.23	
Trial 5					1.23	
<b>33DDS/DGEBA</b>	<b>2.60</b>	<b>0.76</b>	<b>173</b>	<b>186</b>	<b>1.24</b>	<b>0.095</b>
<i>Std. Dev.</i>	<i>0.23</i>	<i>0.02</i>	<i>0.3</i>	<i>1</i>	<i>0.003</i>	<i>0.001</i>
Trial 1	2.45	0.73	174	186	1.23	0.094
Trial 2	2.48	0.78	174	187	1.23	0.096
Trial 3	2.86	0.76	174	186	1.24	
Trial 4		0.77	173		1.24	
Trial 5					1.24	

The comparison of experimental values to simulation values for 44DDS and 33DDS will be used to demonstrate the failures and successes of the revised simulation procedure in accurately predicting properties and showing trends. Tri-functional versions of the amines are simulated to observe the effect of crosslink density on properties. The structures for the four amines used and the epoxy, DGEBA, are given in Figure 19.

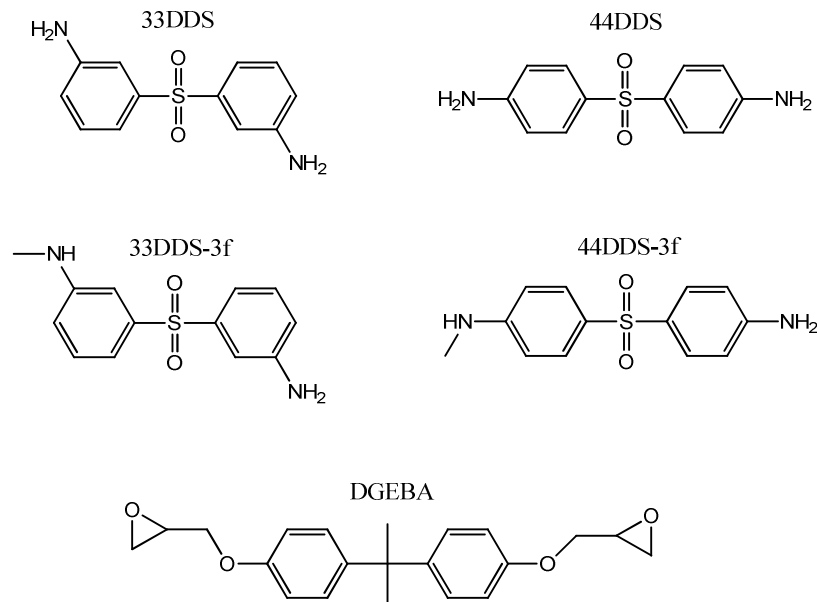


**Figure 19.** Structures of 3f and 4f 33DDS and 44DDS and DGEBA

Table 6 gives the simulation data for these four epoxy systems using the revised simulation procedure. All thermomechanical properties were simulated five times for each system, and the average values and standard deviations are recorded above the five trials for each system. The compression strain at yield is not reported due to a communication problem between software and hardware with the compression analysis at the time these tests were accomplished. The results of the simulations from Section I for 33DDS/DGEBA and 44DDS/DGEBA are tabulated in Table 7 for comparison to the new simulation technique.

**Table 6.** Simulated Properties for 33DDS/DGEBA and 44DDS/DGEBA

System	E, GPa	G, GPa	$\nu$	$\alpha$ , in/in/F $\times 10^{-6}$	$T_g$ , °C	$\rho$ , gm/cc	$J_1$
<b>44DDS</b>	<b>5.08</b>	<b>1.92</b>	<b>0.325</b>	<b>33.2</b>	<b>202</b>	<b>1.202</b>	<b>0.032</b>
<i>Std Dev:</i>	<i>1.11</i>	<i>0.45</i>	<i>0.029</i>	<i>1.3</i>	<i>27</i>	<i>0.005</i>	<i>0.006</i>
Trial 1	5.11	1.92	0.329	33.2	232	1.201	0.038
Trial 2	5.14	1.93	0.328	33.8	215	1.200	0.035
Trial 3	5.94	2.28	0.301	33.0	189	1.198	0.030
Trial 4	3.24	1.18	0.369	34.7	212	1.199	0.036
Trial 5	5.97	2.30	0.298	31.3	163	1.211	0.024
<b>33DDS</b>	<b>4.89</b>	<b>1.83</b>	<b>0.337</b>	<b>29.7</b>	<b>181</b>	<b>1.203</b>	<b>0.026</b>
<i>Std Dev:</i>	<i>0.71</i>	<i>0.29</i>	<i>0.019</i>	<i>2.6</i>	<i>44</i>	<i>0.001</i>	<i>0.009</i>
Trial 1	3.81	1.40	0.366	30.7	206	1.202	0.031
Trial 2	4.86	1.83	0.328	28.6	127	1.204	0.016
Trial 3	5.63	2.14	0.316	27.5	204	1.204	0.027
Trial 4	4.74	1.76	0.345	33.8	227	1.203	0.038
Trial 5	5.40	2.03	0.330	28.0	143	1.204	0.018
<b>3f-44DDS</b>	<b>5.00</b>	<b>1.89</b>	<b>0.324</b>	<b>30.3</b>	<b>202</b>	<b>1.207</b>	<b>0.030</b>
<i>Std Dev:</i>	<i>0.35</i>	<i>0.14</i>	<i>0.015</i>	<i>3.4</i>	<i>48</i>	<i>0.006</i>	<i>0.011</i>
Trial 1	5.62	2.14	0.314	35.1	260	1.202	0.045
Trial 2	4.82	1.80	0.337	31.9	241	1.203	0.038
Trial 3	4.94	1.89	0.303	26.4	144	1.217	0.017
Trial 4	4.84	1.82	0.332	28.1	169	1.207	0.022
Trial 5	4.79	1.80	0.335	30.1	197	1.207	0.028
<b>3f-33DDS</b>	<b>4.74</b>	<b>1.79</b>	<b>0.326</b>	<b>29.1</b>	<b>180</b>	<b>1.210</b>	<b>0.025</b>
<i>Std Dev:</i>	<i>0.35</i>	<i>0.13</i>	<i>0.021</i>	<i>2.7</i>	<i>27</i>	<i>0.005</i>	<i>0.006</i>
Trial 1	4.83	1.81	0.336	28.0	195	1.211	0.026
Trial 2	5.27	2.00	0.321	27.6	175	1.215	0.023
Trial 3	4.32	1.67	0.291	26.1	137	1.206	0.016
Trial 4	4.59	1.71	0.346	32.2	181	1.214	0.028
Trial 5	4.70	1.76	0.337	31.8	210	1.205	0.032

**Table 7.** Simulated Properties for 33DDS/DGEBA and 44DDS/DGEBA

System	E, GPa	G, GPa	$\nu$	$\alpha$ , in/inF $\times 10^{-6}$	$T_g$ , °C	$\rho$ , g/cc	$J_1$	$\epsilon_y$
<b>44DDS</b>	<b>5.07</b>	<b>1.92</b>	<b>0.322</b>	<b>32.4</b>	<b>202</b>	<b>1.196</b>	<b>0.031</b>	<b>0.14</b>
<b>33DDS</b>	<b>4.42</b>	<b>1.68</b>	<b>0.317</b>	<b>35.1</b>	<b>222</b>	<b>1.193</b>	<b>0.038</b>	<b>0.17</b>
<b>3f-44DDS</b>	<b>4.35</b>	<b>1.64</b>	<b>0.327</b>	<b>37.8</b>	<b>231</b>	<b>1.194</b>	<b>0.044</b>	<b>0.15</b>
<b>3f-33DDS</b>	<b>4.21</b>	<b>1.57</b>	<b>0.344</b>	<b>35.2</b>	<b>194</b>	<b>1.203</b>	<b>0.033</b>	<b>0.14</b>

Simulated densities for 33DDS/DGEBA and 44DDS/DGEBA were 1.203 and 1.202, respectively, a little below the experimentally determined values of 1.236 and 1.233, respectively. These densities indicate structures which are adequately minimized, but are likely not the lowest energy conformers. These densities are marginally closer to experimentally determined densities than those reported in Section I, indicating structures which are better minimized. The tri-functional amines showed a further increase in density, once again pointing toward the increased accuracy of simulations in matrices which are not fully crosslinked. The correct trend in density is observed: the 33DDS/DGEBA being slightly denser than 44DDS/DGEBA.

As in Section I, the simulated values for tensile and shear moduli do not show agreement with the experimental data. The experimental values are significantly lower than the simulated values, and the simulations fail to show the correct trend between the meta and para amine. Physical properties determined through experimentation clearly show the 33DDS possesses higher E and G than the 44DDS. The tri-functional amines show values closer to the experimentally determined values, but the trend is inaccurate once again.

The simulated  $T_g$  for 44DDS/DGEBA is 202°C, a little below the experimentally determined  $T_g$  range of 210 - 230°C. However, the simulated  $T_g$  for 33DDS/DGEBA is 180°C, right in the middle of the experimentally determined  $T_g$  range of 170 - 190°C. These  $T_g$ s are in much better agreement with experimental  $T_g$ s than those recorded in Chapter I. The tri-functional amines show no difference in  $T_g$ , giving values of 181°C and 202°C for 33DDS/DGEBA and 44DDS/DGEBA, respectively. This is a significant departure from simulations in Chapter I in which the tri-functional amines showed  $T_g$ s much closer to experimental values. One point for improvement is seen in the high variance within each averaged set. Although the averaged data give good approximations and show the correct trend (44DDS/DGEBA possessing a higher  $T_g$  than 33DDS/DGEBA), the variance is cause for some concern about the repeatability of the experiments and will be addressed in Section III.

### ***Pendant Bulky Group Simulations***

To study the effect of bulky pendant groups reacted into an epoxy matrix, methyl POSS and fluorinated pyrene were incorporated into epoxy matrices. Table 3.4 summarizes the results for incorporation of POSS into a 33DDS/DGEBA matrix at 2.5, 5.0, and 7.5 mole %, corresponding to 5, 13, and 21 wt. %, respectively. At the top of Table 8, the average results for the simulated properties of 33DDS/DGEBA are included.

**Table 8.** Simulations for 33DDS/DGEBA Matrix with Pendant Methyl POSS

System	E, GPa	G, GPa	$\nu$	$\alpha$ , in/in/F $\times 10^{-6}$	T <sub>g</sub> , °C	$\rho$ , g/cc	J <sub>1</sub>	$\epsilon_y$
33DDS	<b>4.89</b>	<b>1.83</b>	<b>0.337</b>	<b>29.7</b>	<b>181</b>	<b>1.203</b>	<b>0.026</b>	<b>0.17</b>
2.5% POSS / 33DDS	<b>5.55</b>	<b>2.14</b>	<b>0.302</b>	<b>29.6</b>	<b>188</b>	<b>1.200</b>	<b>0.027</b>	<b>0.13</b>
Std Dev:	<b>1.50</b>	<b>0.63</b>	<b>0.038</b>	<b>0.5</b>	<b>42</b>	<b>0.005</b>	<b>0.006</b>	<b>0.03</b>
Trial 1	4.49	1.69	0.329	29.9	158	1.203	0.022	0.11
Trial 2	6.61	2.59	0.275	29.2	218	1.196	0.031	0.16
5% POSS / 33DDS	<b>7.01</b>	<b>2.71</b>	<b>0.292</b>	<b>33.7</b>	<b>209</b>	<b>1.219</b>	<b>0.034</b>	<b>0.15</b>
Std Dev:	<b>0.10</b>	<b>0.05</b>	<b>0.007</b>	<b>2.3</b>	<b>25</b>	<b>0.003</b>	<b>0.003</b>	<b>0.02</b>
Trial 1	7.07	2.75	0.287	32.1	227	1.217	0.036	0.17
Trial 2	6.94	2.68	0.297	35.3	192	1.221	0.032	0.14
7.5% POSS / 33DDS	<b>10.20</b>	<b>4.05</b>	<b>0.249</b>	<b>30.5</b>	<b>217</b>	<b>1.224</b>	<b>0.032</b>	<b>0.17</b>
Std Dev:	<b>0.34</b>	<b>0.11</b>	<b>0.004</b>	<b>0.2</b>	<b>13</b>	<b>0.004</b>	<b>0.001</b>	<b>0.01</b>
Trial 1	10.44	4.13	0.246	30.3	226	1.221	0.033	0.16
Trial 2	9.96	3.98	0.252	30.6	207	1.226	0.031	0.18

The simulations for pendant POSS matrices show strong trends of increasing  $E$ ,  $G$ ,  $T_g$ ,  $\rho$ ,  $J_1$ , and  $\varepsilon_y$  and decreasing  $\nu$  with increased POSS content. This indicates a matrix which possesses both higher stiffness and greater distortional capability, making it unusual and of significant interest for validation of Onset Theory. The increased  $T_g$ , tensile modulus, and shear modulus, with only slight increase in density make this material of interest for a number of applications which demand such performance criteria.

The simulations for pendant F-pyrene matrices do not show the same clear trends as the POSS matrices (Table 9). Density increases marginally with increased F-pyrene, but other physical properties do not follow clear trends of increased performance with increased F-pyrene content.  $E$ ,  $G$ , and  $\varepsilon_y$  reach maximum values for 5% and then drop off at 7.5% F-pyrene. Poisson's ratio,  $T_g$ , and  $J_1$  reach minima at 5% and then rebound at 7.5% F-pyrene incorporation. Compared to POSS incorporation, F-pyrene shows a significantly less drastic effect on physical properties.

**Table 9.** Simulations for 33DDS/DGEBA Matrix with Pendant Fluorinated Pyrene

System	E, GPa	G, GPa	N	$\alpha$ , in/in/F $\times 10^{-6}$	T <sub>g</sub> , °C	$\rho$ , g/cc	J <sub>1</sub>	$\epsilon_y$
<b>33DDS</b>	<b>4.89</b>	<b>1.83</b>	<b>0.337</b>	<b>29.7</b>	<b>181</b>	<b>1.203</b>	<b>0.026</b>	<b>0.17</b>
<b>2.5% F-py / 33DDS</b>	<b>4.50</b>	<b>1.67</b>	<b>0.344</b>	<b>30.1</b>	<b>208</b>	<b>1.197</b>	<b>0.030</b>	<b>0.14</b>
Std Dev:	<b>0.65</b>	<b>0.27</b>	<b>0.023</b>	<b>1.1</b>	<b>19</b>	<b>0.006</b>	<b>0.003</b>	<b>0.03</b>
Trial 1	3.75	1.37	0.371	31.2	211	1.191	0.032	0.11
Trial 2	4.91	1.83	0.334	30.2	188	1.203	0.027	0.16
Trial 3	4.83	1.82	0.328	29.0	226	1.198	0.032	0.16
<b>5% F-py / 33DDS</b>	<b>4.73</b>	<b>1.78</b>	<b>0.330</b>	<b>31.1</b>	<b>180</b>	<b>1.204</b>	<b>0.026</b>	<b>0.17</b>
Std Dev:	<b>0.27</b>	<b>0.11</b>	<b>0.006</b>	<b>2.7</b>	<b>32</b>	<b>0.009</b>	<b>0.006</b>	<b>0.02</b>
Trial 1	4.98	1.88	0.326	33.4	157	1.208	0.024	0.18
Trial 2	4.44	1.66	0.336	31.8	216	1.193	0.033	0.15
Trial 3	4.78	1.80	0.327	28.2	168	1.21	0.022	0.16
<b>7.5% F-py / 33DDS</b>	<b>4.64</b>	<b>1.74</b>	<b>0.337</b>	<b>32.0</b>	<b>207</b>	<b>1.210</b>	<b>0.032</b>	<b>0.15</b>
Std Dev:	<b>0.36</b>	<b>0.15</b>	<b>0.009</b>	<b>1.2</b>	<b>25</b>	<b>0.005</b>	<b>0.004</b>	<b>0.02</b>
Trial 1	4.37	1.62	0.347	32.5	228	1.204	0.036	0.16
Trial 2	5.05	1.90	0.329	30.6	212	1.214	0.032	0.13
Trial 3	4.51	1.69	0.335	32.8	179	1.212	0.028	0.18

The primary improvement presented in this section is the increased accuracy for simulated T<sub>g</sub> of 33DDS/DGEBA in both the tri-functional and tetra-functional amine simulations. The other noticeable deviation in simulations from this section is the difference in values between the tri-functional and tetra-functional amines is negligible. The tri-functional amines marginally lowered tensile and shear moduli and increased density but showed no other significant changes. Although the simulated T<sub>g</sub> for 33DDS/DGEBA is closer to experimental values in Chapter II, the simulated T<sub>g</sub> for 44DDS/DGEBA is still low and the variances in T<sub>g</sub>

values are too high. Additionally, the modulus values still significantly overestimate experimental capability and show the reverse trend, with 44DDS possessing the higher E and G. Although Section II simulations are more accurate than those presented in Section I, the need for an improved simulation procedure is still apparent.

POSS incorporation into a 33DDS/DGEBA matrix as a pendant group showed considerable improvement in physical properties with increased POSS content, while F-pyrene only marginally affected properties. The trends observed with POSS incorporation indicate a matrix material which should be synthesized, and experimentally tested to determine whether the simulated gain in physical properties can be realized. Ongoing work in the Wiggins Research Group is focusing upon the solubilization and miscibilization of pendant POSS and other bulky groups into epoxy networks.

## **RESULTS PART III**

### **A MOLECULAR DYNAMICS APPROACH TO PREDICTING PROPERTIES OF CROSSLINKED AROMATIC POLYMERS**

#### **Objective**

The third section's sole purpose is to improve the simulation procedure such that simulations more accurately match experimental results. Once again 33DDS/DGEBA and 44DDS/DGEBA will be simulated and compared to experimental analysis. Additionally, matrices of hexamethylene diamine (HDA) and bis(hexamethylene)triamine (B-HTA) are simulated with DGEBA (Figure 20). The simulation of linear aliphatic amines provides a network with less aromaticity. High phenyl ring content complicates simulations by making the chains more rigid and therefore more difficult to relax energetically. Ring catenation also becomes a problem with such highly aromatic matrices. Additionally, 33DDS and 44DDS possess sulfone groups, which create complexities in the simulation in terms of defining secondary forces, such as hydrogen bonding, and make matrices even more rigid. Our hypothesis was that the HDA/DGEBA and B-HTA/DGEBA matrices would provide more accurate simulations due to their relative simplicity in comparison to 33DDS/DGEBA and 44DDS/DGEBA.

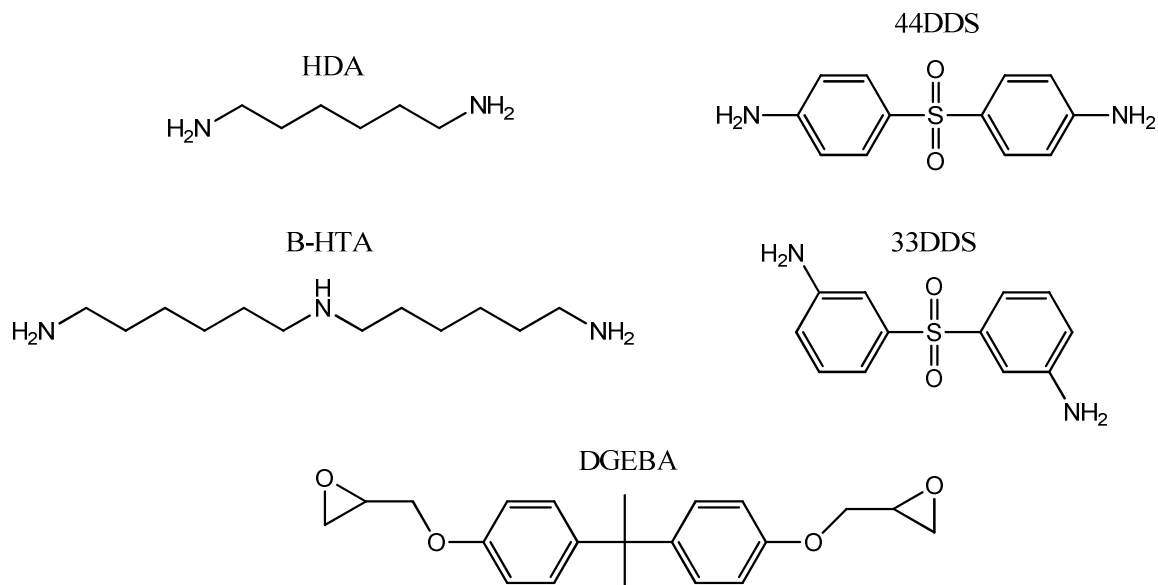


**Figure 20.** Chemical Structures of Amines and DGEBA.

To address the problems remaining in the simulation procedure from Section II, in the third round of simulations, specific attention was lent to creating more realistic polymers, performing more realistic simulations, and using more trials to average out error and obtain more accurate results. With these goals in mind, the temperature cycle was once again refined to include more dynamics steps in the temperature range of the glass transition.

Additionally, we had concerns about the dendrimer build we used to create the polymers. In previous simulations, perfect dendrimers were built assuming complete crosslinking until the last addition of epoxy or amine, which would balance stoichiometry. This perfect dendritic growth is likely not the best procedure to simulate molecular weight growth in epoxies. For the work in this section, we use a build script in which amine and epoxy monomer structures are reacted to create a randomized crosslinked network.<sup>77</sup> The protocol for compression analysis was also altered to a strain-controlled as opposed to stress-controlled compression.<sup>78</sup> Finally, a

few other small modifications to the procedure were made to ensure we were minimizing the energy in the system as much as possible.

## **Methods**

### ***MD Simulation Procedure***

Molecular dynamics calculations were completed in an updated version of Accelrys' software, Materials Studio 5.0. The Condensed Phase Optimized Molecular Potentials for Atomistic Simulation Studies (COMPASS) forcefield and group based cutoffs based on user assigned charge groups were still used. The quality used for most of the simulations is still "Medium," but this is increased to "Fine" for the elastic property determination.

### ***Build seed and structures***

The Seeds and Structures are built in exactly the same way as in Chapter I.

### ***Build polymer and amorphous cell.***

The polymer build script used in this section directs molecular weight growth through a computer-controlled randomized dendrimer build. Stoichiometry is set to 2:1 epoxies-to-amines, corresponding to 1:1 epoxides-to-reactive amine hydrogens, and the number of atoms is set to 5,000. Based on the stoichiometry and number of atoms, the script determines the number of generations and creates connect points each generation using a random number generator. This simulation polymerization procedure shares commonality with collision theory for chemical reactions. By matching the simulation procedure to our understanding of real crosslinking polymerizations, we will see an improved accuracy in thermomechanical property prediction.

For each polymer system, ten polymers were built using the build script. Each of these ten polymers was incorporated into an amorphous cell for a total of ten amorphous cells on

which the thermomechanical properties will be determined. In previous simulations in Chapters I and II, only one polymer build was accomplished and three amorphous cells were made from this one build. The amorphous cells were constructed in the same manner as in Section I, with the exception that the density was increased to  $0.5\text{g/cm}^3$ .

### ***Minimization and equilibration***

The minimization of the ten amorphous cells was made more rigorous by increasing the number of iterations to 200,000 or until convergence was reached. All amorphous cells converged before 200,000 iterations were reached. The annealing process was kept the same as described in Section I.

### ***Calculation of molecular trajectories***

The calculation of molecular trajectories is completed in the same manner as stated in the Section I.

### ***Analysis of molecular trajectories***

Tensile modulus (E), shear modulus (G), and Poisson's ratio ( $\nu$ ) are all calculated using the same procedure as recorded in Chapter I, but using the "Fine" quality setting.

Compression analysis was completed using a strain-controlled compression script obtained from Boeing. Each of the ten cells is compressed uniaxially the x, y, and z directions in separate simulations. The cells are compressed from 0 to 20% strain, in increments of 0.5% strain. The stress induced in the cells by this straining process is recorded at each of the forty increments. A stress vs. strain curve is approximated by fitting the data to a second order polynomial. The compression yield point is approximated from the maximum of the second order polynomial curve. Von Mises strain is then approximated by multiplying the compression

yield strain by 1.5. Compression modulus is calculated by taking the slope of a linear best fit curve from 0 to 2% strain.

CTE ( $\alpha$ ), glass transition temperature ( $T_g$ ), density ( $\rho$ ), and the first invariant of the strain tensor ( $J_1$ ) are determined using the temperature cycle in Amorphous Cell Protocols. As in Chapter II, the temperature cycle is broken up into two steps: a heating simulation and a cooling simulation. In order to obtain more accurate  $T_g$ s, the temperature cycle was employed in a 200K range, from 100K below the expected  $T_g$  (as determined by DSC, DMA) to 100K above  $T_g$ . Before starting the heating/cooling ramps, additional NPTs are run to equilibrate each cell at both 100K below expected  $T_g$  (for heating) and 100K above expected  $T_g$  (for cooling). These NPTs are completed at 0.0001GPa (1bar) using 25,000 time steps of 1fs, giving a total dynamics time of 25ps. The final structure generated in this NPT will be the structure for the heating and cooling simulations.

For both the heating and cooling ramps, the number of stages is 20, which will give a simulated volume and density every 10K, the stage duration is increased to 120,000fs, and the averaging period is increased to 60,000fs. The number of data points in the V vs. T curve is decreased to 19 as seen in Figure 21. Glassy and rubbery CTEs,  $T_g$ , and  $J_1$  were all calculated in the same manner as reported in Chapter I. Figure 21 shows that focusing the simulation in a small temperature window above and below  $T_g$ , and increasing the number of time steps in this window yields a V vs. T curve that shows a much more distinct  $T_g$ . If this protocol still gives results with lower accuracy than desired, the stage duration and averaging period can be increased to produce a more accurate V vs. T curve.

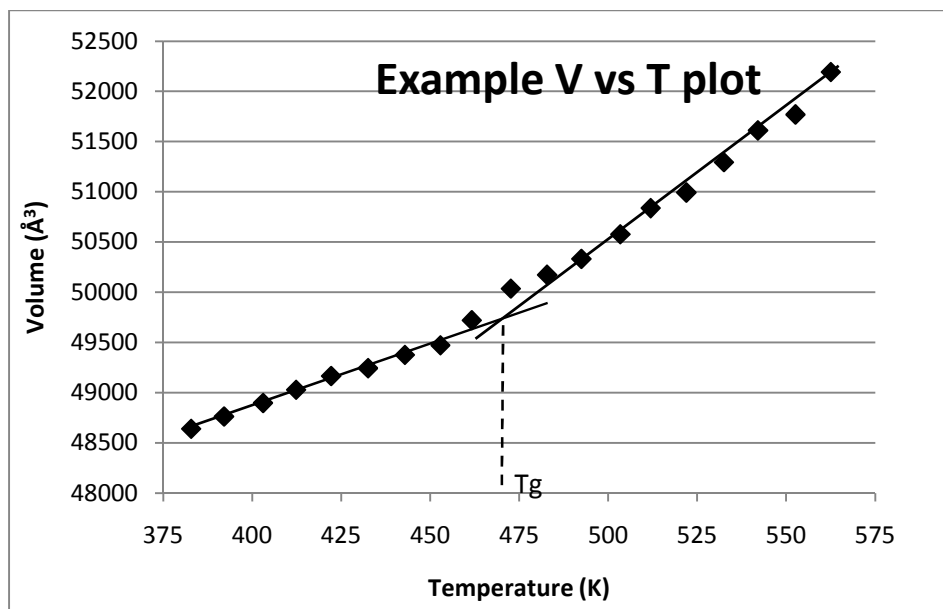


**Figure 21.** Example volume vs. temperature plot, more rigorous cycle.

### 33DDS/DGEBA and 44DDS/DGEBA Experimental vs. Simulation Comparison

Experimentally determined physical properties for 33DDS/DGEBA and 44DDS/DGEBA to be compared to simulation values are summarized in Table 10.

**Table 10.** Experimental Properties for 33DDS/DGEBA and 44DDS/DGEBA

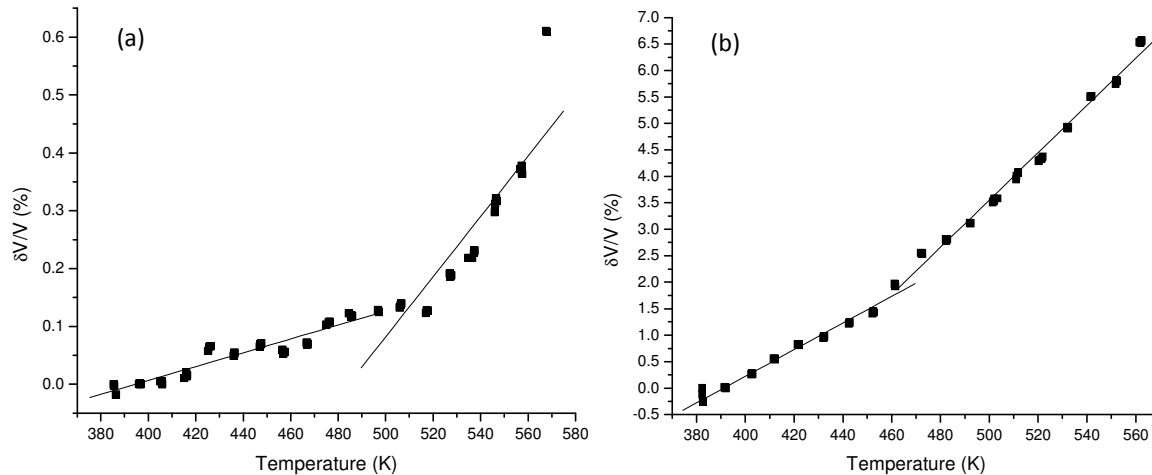
System	E, GPa	G, GPa	T <sub>g</sub> , °C DSC	T <sub>g</sub> , °C DMA	ρ, g/cc	ε <sub>y</sub>	σ <sub>y</sub>	M, Gpa
<b>44DDS</b>	<b>2.19</b>	<b>0.71</b>	<b>217</b>	<b>220</b>	<b>1.23</b>	<b>0.110</b>	<b>0.140</b>	<b>2.64</b>
<i>Std. Dev.</i>	<i>0.31</i>	<i>0.05</i>	<i>0.4</i>	<i>1</i>	<i>0.001</i>	<i>0.002</i>	<i>0.0001</i>	<i>0.05</i>
Trial 1	1.85	0.7412	217	220	1.24	0.112	0.140	2.60
Trial 2	2.26	0.69797	218	220	1.23	0.109	0.140	2.68
Trial 3	2.45	0.65104	217	221	1.23			
Trial 4		0.75179	217		1.23			
Trial 5					1.23			
<b>33DDS</b>	<b>2.60</b>	<b>0.76</b>	<b>173</b>	<b>186</b>	<b>1.24</b>	<b>0.095</b>	<b>0.143</b>	<b>2.85</b>
<i>Std. Dev.</i>	<i>0.23</i>	<i>0.02</i>	<i>0.3</i>	<i>1</i>	<i>0.003</i>	<i>0.001</i>	<i>0.0002</i>	<i>0.03</i>
Trial 1	2.45	0.73242	174	186	1.23	0.094	0.143	2.87
Trial 2	2.48	0.77713	174	187	1.23	0.096	0.143	2.83
Trial 3	2.86	0.75513	174	186	1.24			
Trial 4		0.77341	173		1.24			
Trial 5					1.24			

Table 11 shows simulated thermomechanical properties for 33DDS/DGEBA and 44DDS/DGEBA matrices. Despite improved simulation procedure, simulated tensile and shear moduli values are still far greater than experimentally determined values, and the trend still incorrectly shows 33DDS/DGEBA to possess lower E and G than 44DDS/DGEBA. Density values are still a little low, but the trend is correct, as in previous simulations. Simulated compression strain at yield is greater for simulated matrices than experiments show, and the trend is backwards.

**Table 11.** Simulated Properties for 33DDS/DGEBA and 44DDS/DGEBA

System	E, GPa	G, GPa	T <sub>g</sub> , °C	ρ, g/cc	ε <sub>y</sub>	σ <sub>y</sub> , GPa	M, GPa
<b>44DDS</b>	<b>4.85</b>	<b>1.83</b>	<b>221</b>	<b>1.204</b>	<b>0.19</b>	<b>0.322</b>	<b>2.79</b>
<i>Std Dev:</i>	<i>0.42</i>	<i>0.15</i>	<i>15</i>	<i>0.007</i>	<i>0.04</i>	<i>0.032</i>	<i>0.46</i>
Trial 1	4.88	1.85	229	1.200	0.17	0.306	3.32
Trial 2	5.16	1.94	229	1.208	0.17	0.337	2.02
Trial 3	3.89	1.49	217	1.187	0.17	0.294	3.39
Trial 4	4.73	1.78	227	1.203	0.16	0.310	2.87
Trial 5	5.18	1.95	229	1.205	0.21	0.344	2.71
Trial 6	4.58	1.71	212	1.199	0.16	0.276	3.16
Trial 7	5.16	1.95	234	1.206	0.19	0.311	2.66
Trial 8	4.60	1.73	181	1.210	0.18	0.345	2.87
Trial 9	5.17	1.96	224	1.207	0.27	0.310	2.79
Trial 10	5.16	1.95	224	1.212	0.22	0.387	2.10
<b>33DDS</b>	<b>4.53</b>	<b>1.69</b>	<b>197</b>	<b>1.208</b>	<b>0.17</b>	<b>0.331</b>	<b>3.44</b>
<i>Std Dev:</i>	<i>0.36</i>	<i>0.14</i>	<i>18</i>	<i>0.004</i>	<i>0.02</i>	<i>0.019</i>	<i>0.34</i>
Trial 1	4.36	1.62	206	1.204	0.18	0.309	3.61
Trial 2	4.89	1.85	174	1.215	0.19	0.363	3.28
Trial 3	4.60	1.72	195	1.205	0.15	0.326	3.94
Trial 4	4.76	1.77	234	1.205	0.17	0.315	2.84
Trial 5	4.75	1.77	178	1.210	0.16	0.315	3.22
Trial 6	4.32	1.61	181	1.210	0.14	0.335	3.73
Trial 7	4.32	1.61	196	1.210	0.19	0.357	3.75
Trial 8	3.71	1.37	216	1.211	0.17	0.332	3.57
Trial 9	4.90	1.85	201	1.207	0.20	0.349	3.39
Trial 10	4.65	1.74	186	1.207	0.18	0.313	3.09

However, despite the many inadequacies the simulations still possess, simulated  $T_g$ s are close to the experimentally determined range, standard deviations have been reduced, and  $V$  vs.  $T$  plots show clear  $T_g$ s, a feat which had not been accomplished in previous simulations (Figure 22).



**Figure 22.** Simulated  $V$  vs.  $T$  plots for 44DDS/DGEBA (a) and 33DDS/DGEBA (b).

Simulated compression analysis was also improved. Although yield strains were still higher than experimental determinations and still showed the incorrect trend of 33DDS/DGEBA possessing lower strain at yield, simulated compression modulus values were fairly accurate and showed the correct trend (Figure 23).

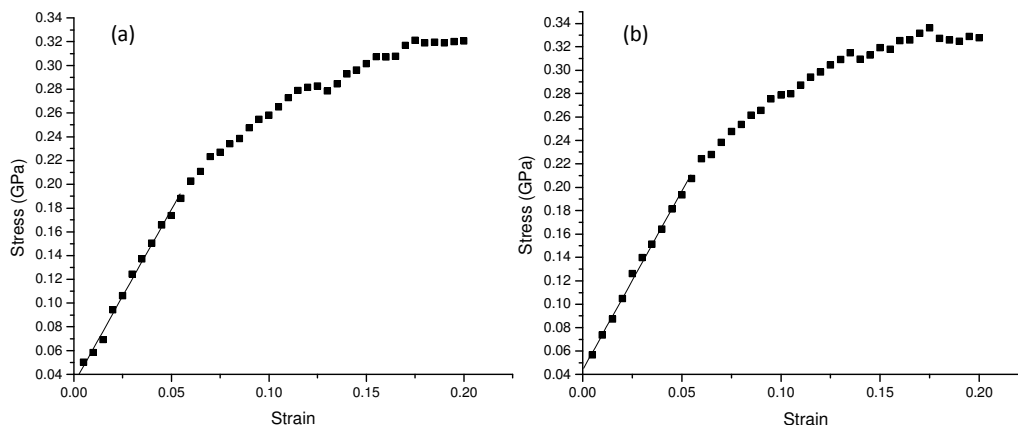


**Figure 23.** Simulated compression for 44DDS/DGEBA (a) and 33DDS/DGEBA (b).

***HDA/DGEBA and B-HTA/DGEBA Experimental vs. Simulation Comparison***

Tensile Modulus,  $T_g$ , and density of HDA/DGEBA and B-HTA/DGEBA matrices were determined experimentally and are summarized in Table 12. HDA/DGEBA possessed a higher  $T_g$  and density than B-HTA/DGEBA.  $T_g$  ranges, as determined by DSC and DMA were equivalent for the two samples. Shear modulus and compression analysis values need to be experimentally determined.

**Table 12.** Experimental Properties for HDA/DGEBA and B-HTA/DGEBA

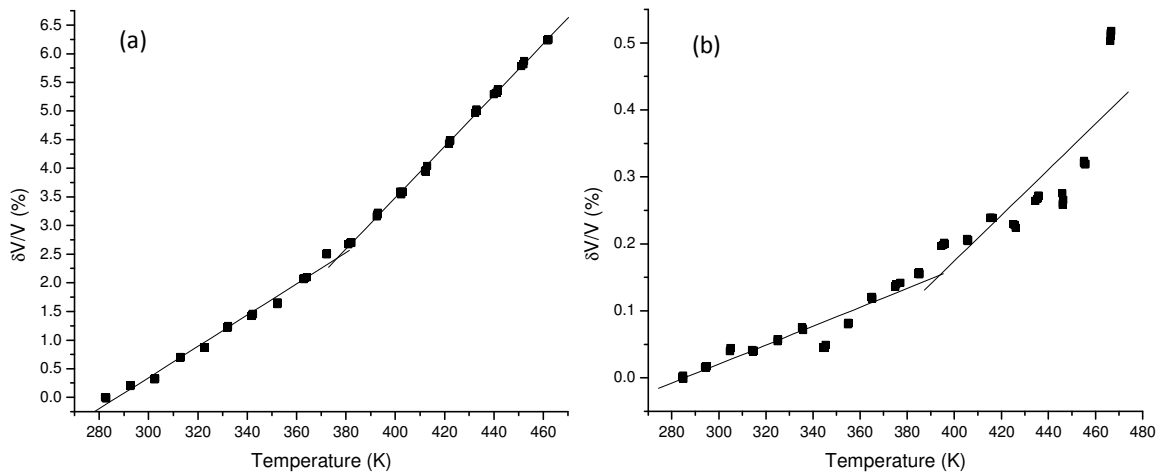
System	E, GPa	$T_g$ , °C DSC	$T_g$ , °C DMA	$\rho$ , gm/cc
<b>HDA</b>	<b>2.86</b>	<b>100</b>	<b>124</b>	<b>1.16</b>
<i>Std. Dev.</i>	<i>0.69</i>	<i>1</i>	<i>2</i>	<i>0.001</i>
Trial 1	3.62	100	126	1.16
Trial 2	2.68	101	124	1.16
Trial 3	2.27	100	121	1.16
Trial 4				1.16
Trial 5				1.16
<b>B-HTA</b>	<b>1.73</b>	<b>106</b>	<b>118</b>	<b>1.16</b>
<i>Std. Dev.</i>	<i>0.63</i>	<i>3</i>	<i>2</i>	<i>0.0004</i>
Trial 1	1.14	106	116	1.16
Trial 2	1.66	109	118	1.15
Trial 3	2.39	102	120	1.16
Trial 4				1.16
Trial 5				1.16

Table 13 summarizes properties determined via MD simulations for HDA/DGEBA and B-HTA/DGEBA matrices. Simulated properties of HDA/DGEBA and B-HTA/DGEBA showed values with similar trends as seen in previous simulations, such overestimating E by a large margin and density by a smaller margin. However, significant improvement on  $T_g$  simulation was observed.  $T_g$ s for both matrices are within the experimental range, and standard deviations have been significantly reduced.

**Table 13.** Simulated Properties for HDA/DGEBA and B-HTA/DGEBA

System	E, GPa	G, GPa	$T_g$ , °C	$\rho$ , gm/cc	$\varepsilon_y$	$\sigma_y$ , GPa	M, GPa
<b>HDA</b>	<b>4.67</b>	<b>1.75</b>	<b>103</b>	<b>1.139</b>	<b>0.17</b>	<b>0.313</b>	<b>3.36</b>
<i>Std Dev:</i>	<i>0.39</i>	<i>0.16</i>	<i>19</i>	<i>0.006</i>	<i>0.01</i>	<i>0.031</i>	<i>0.46</i>
Trial 1	4.50	1.70	100	1.142	0.16	0.297	3.57
Trial 2	5.43	2.08	105	1.145	0.15	0.372	3.09
Trial 3	5.06	1.92	96	1.135	0.18	0.313	4.03
Trial 4	4.46	1.68	78	1.139	0.18	0.318	2.87
Trial 5	4.76	1.79	122	1.149	0.17	0.348	3.10
Trial 6	4.41	1.64	136	1.138	0.17	0.304	3.20
Trial 7	4.14	1.54	120	1.136	0.16	0.291	2.74
Trial 8	5.01	1.88	82	1.147	0.17	0.329	3.95
Trial 9	4.43	1.65	107	1.133	0.18	0.295	3.87
Trial 10	4.48	1.68	82	1.130	0.16	0.262	3.21
<b>B-HTA</b>	<b>4.29</b>	<b>1.61</b>	<b>117</b>	<b>1.113</b>	<b>0.19</b>	<b>0.308</b>	<b>3.40</b>
<i>Std Dev:</i>	<i>0.53</i>	<i>0.22</i>	<i>8</i>	<i>0.006</i>	<i>0.03</i>	<i>0.055</i>	<i>0.77</i>
Trial 1	4.79	1.81	101	1.124	0.22	0.399	4.54
Trial 2	4.09	1.52	110	1.115	0.15	0.300	3.22
Trial 3	4.33	1.65	120	1.107	0.16	0.179	2.60
Trial 4	4.34	1.65	113	1.103	0.23	0.283	1.87
Trial 5	4.14	1.55	120	1.109	0.20	0.298	3.69
Trial 6	4.99	1.89	117	1.119	0.18	0.337	4.15
Trial 7	4.43	1.66	124	1.113	0.17	0.328	3.09
Trial 8	3.95	1.47	123	1.117	0.18	0.333	3.90
Trial 9	4.75	1.81	131	1.115	0.20	0.310	3.47
Trial 10	3.10	1.13	114	1.112	0.16	0.311	3.44

Additionally, V vs. T plots show distinct at  $T_g$ , a feat which had not been accomplished by previous simulations (Figure 24). Oddly, although the B-HTA/DGEBA possesses a lower standard deviation, the V vs. T plot created from the average of the 10 runs does not show a  $T_g$  as clearly as the HDA/DGEBA.



**Figure 24.** Simulated V vs. T plots for HDA/DGEBA (a) and B-HTA/DGEBA (b).

Although experimental compression analysis has not yet been completed for these samples, simulated compression tests show curves that look like compression curves should (Figure 25). This had not been accomplished in previous simulation analysis.

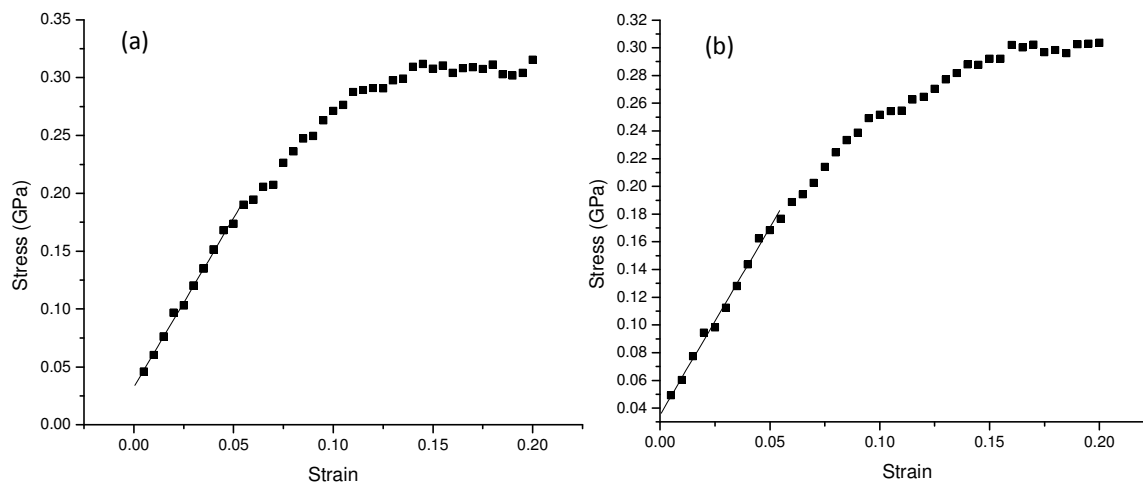


**Figure 25.** Simulated compression for HDA/DGEBA (a) and B-HTA/DGEBA (b).

Thermomechanical property simulations of amorphous networks using molecular dynamics are still in need of improvement. Tensile and shear moduli and compression strain at yield are consistently higher in simulations than experimental determinations. Progress has been made in the simulation of  $T_g$  and compression modulus by altering the simulation procedure including using the random dendrimer builder, strain controlled compression analysis, and increasing simulation rigor near  $T_g$  in the  $V$  vs.  $T$  determination. However, research still needs to be accomplished to determine the causes of error and possible solutions to help MD simulations reach their potential of accurately predicting physical properties of crosslinked polymers.

## **RESULTS PART IV**

### **INVESTIGATION OF PHENYL RING MOTIONS IN 33DDS/DGEBA AND 44DDS/DGEBA MATRICES BY DEUTERIUM NMR SPECTROSCOPY**

#### **Introduction**

Nuclear magnetic resonance (NMR) spectroscopy is a sensitive instrumental tool for studying relaxation phenomena in materials. There are numerous relaxation processes within molecules that create fluctuating dipoles, including dipole-dipole, chemical shift anisotropy (CSA), spin rotation, scalar, and quadrupolar relaxations. For polymers, the principle sources of relaxation are dipolar, CSA, and quadrupolar interactions.<sup>79</sup> Quadrupolar relaxations result directly from the quadrupolar moment of the nucleus itself, i.e., the nucleus' unsymmetrical charge. An important advantage of  $^2\text{H}$  NMR analysis, which requires  $^2\text{H}$  labeled samples, is that CSA and dipolar mechanisms do not significantly contribute to spin-lattice relaxation or lineshape. Therefore, the spectroscopic behavior of  $^2\text{H}$  atoms is almost exclusively governed by quadrupolar mechanisms. Relaxation is due to fluctuating fields created by molecular motion, thereby making deuterium NMR spectroscopy a highly sensitive probe of molecular motion. Solid-state deuterium NMR spectroscopy has been used extensively to monitor polymer mobility. The lineshape and spin-lattice relaxation ( $T_1$ ) times are sensitive to the mode and rate of motion, and these methods have been used to study phenyl ring and methylene motion in polymers.<sup>1,80</sup>

For  $^2\text{H}$  labeled phenyl rings, a distribution of motions with variability in phenyl ring flip angle and flip rate is observed. Previous work normally employs a stretched exponential, such as the Kohlrausch Williams Watts (KWW) expression, to characterize this distribution of rates.<sup>81</sup>

In addition, a simple Gaussian distribution describing the deviation of the flips from  $180^\circ$  is often used with a very fast librational motion pre-averaged into the simulated lineshape by adjusting the quadrupolar coupling constant,  $C_Q$ .<sup>4</sup> This description of ring motions is useful but introduces a higher degree of complexity in the analysis. Here, a simplistic approach was utilized to interpret  $T_1$  and lineshape data.

## **Objective**

The principle objective of this work is to describe the motional behavior of the amine and epoxy aromatic rings in 33DDS/DGEBA and 44DDS/DGEBA. To accomplish this goal, the amine and epoxy phenyl rings have been selectively deuterated, and the motions studied using  $^2\text{H}$  spin-lattice relaxation ( $T_1$ ) studies and lineshape analysis. Spin-lattice relaxation analysis is used to discriminate between ring motions possessing different rates, while lineshape analysis is used to provide information about both the types and rates of phenyl ring motions occurring. Once the basic rates of ring motions have been described using  $T_1$  studies, the contributions of each motion to lineshape can be determined by comparison of the spin-lattice relaxation data to lineshape data. By combining spin-lattice relaxation data with lineshape data, a clear picture of the types and rates of phenyl ring motion can be determined.

In this work deuterium NMR spectroscopy is used to describe the rates and types of motions of selectively labeled aromatic rings. Future work will combine  $^2\text{H}$  NMR spectroscopy with simulation results to determine activation energies and their corresponding motional correlation times. Dielectric spectroscopy (DES) and dynamic mechanical analysis (DMA) typically use a constant frequency with the temperature varied to detect relaxation processes resonant with the predetermined frequency. By combining  $^2\text{H}$  NMR spectroscopic information with DES and

DMA data, the specific moieties within the polymer responsible for sub- $T_g$  relaxations observed in DES and DMA can be determined.<sup>3,82</sup> The relationship of sub- $T_g$  motions to bulk mechanical properties, such as modulus and toughness is well documented.<sup>83,84,85</sup> The ability to connect  $^2\text{H}$  NMR spectroscopic data to DES and DMA results provides significant potential for understanding the chemistries and structures within polymers that are responsible for mechanical properties.

## **Materials**

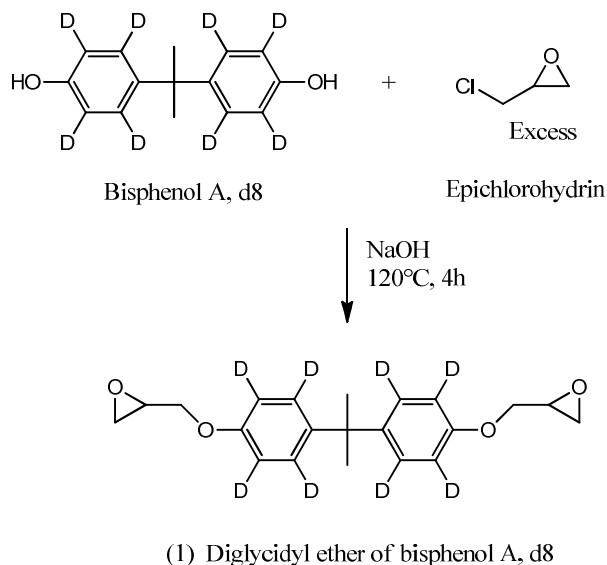
Epichlorohydrin ( $\geq 99\%$  purity), anhydrous toluene (99.8% purity), anhydrous sodium hydroxide pellets (NaOH,  $\geq 98\%$  purity), toluene ( $\geq 99\%$  purity), acetic anhydride ( $\geq 98\%$  purity), carbon disulfide ( $\geq 99\%$  purity), sulfonyl chloride ( $\geq 98\%$  purity), aluminum trichloride ( $\geq 98\%$  purity), glacial acetic acid, ammonium chloride ( $\geq 99\%$  purity), tetrahydrofuran (THF,  $\geq 99\%$  purity), hydrogen peroxide ( $\geq 98\%$  purity), hydrochloric acid (HCl,  $\geq 98\%$  purity), decolorizing carbon, methanol ( $\geq 99\%$  purity), potassium nitrate ( $\text{KNO}_3$ ,  $\geq 98\%$  purity), sulfuric acid ( $\text{H}_2\text{SO}_4$ ,  $\geq 98\%$  purity), chlorosulfonic acid ( $\geq 99\%$  purity), chloroform ( $\geq 99\%$  purity), methylene chloride ( $\geq 98\%$  purity), dimethyl formamide (DMF,  $\geq 99\%$  purity), palladium-carbon catalyst, 3,3'-diaminodiphenyl sulfone (33DDS, 97% purity), and 4,4'-diaminodiphenyl sulfone (44DDS, 97% purity) were purchased from Sigma Aldrich and used as received. The NaOH pellets were dissolved into deionized water to make a 40%wt. aqueous NaOH solution. Ring deuterated bisphenol A (d8-BPA, 98% purity), ring deuterated aniline (d5-aniline, 98% purity), and deuterated benzene (d6-benzene, 99.5% purity) were obtained from Cambridge Isotope Laboratories, Inc. and used as received. Hydrogen gas was purchased from Nordan Smith and used as received.

## Methods

### Ring Deuterated d8-DGEBA Synthesis

Ring deuterated diglycidyl ether of bisphenol A (d8-DGEBA) was synthesized by the reaction of d8-BPA and epichlorohydrin. The synthesis was accomplished in a two-neck flask fitted with reflux condenser; 3.5g (0.015 mol) of D8-BPA and 13.9g (0.15 mol) epichlorohydrin were added and heated to 120°C under magnetic stirring. 3g of 40%wt. aqueous sodium hydroxide (0.03 mol) was added to the boiling reaction mixture and allowed to reflux for 4 hours. The excess epichlorohydrin was then distilled off the reaction product. Toluene was added with stirring to precipitate off the NaCl salt. The precipitate salt was filtered off the filtrate, and additional toluene was used to wash any remaining product off the solid salt. Toluene was then distilled off the filtrate to leave the reaction product d8-DGEBA. The d8-DGEBA was then dried under vacuum at 50°C. The d8-DGEBA showed no indication of impurities using  $^{13}\text{C}$  and  $^1\text{H}$  NMR, indicating the purity is >95% (product1, Scheme 1).

**Scheme 1.** Synthesis of d8-DGEBA



### **Ring Deuterated d8-44DDS Synthesis**

Ring deuterated aniline (2g) was added to 20ml acetic anhydride and heated at reflux for 30min. After cooling to room temperature, 25ml water was added and heated at reflux for 10min. The solution was then cooled to room temperature and diluted with water to precipitate the product, N-acetylaniline. The ring deuterated N-acetylaniline was filtered, washed with water, recrystallized from water, and dried (product 1, Scheme 2).

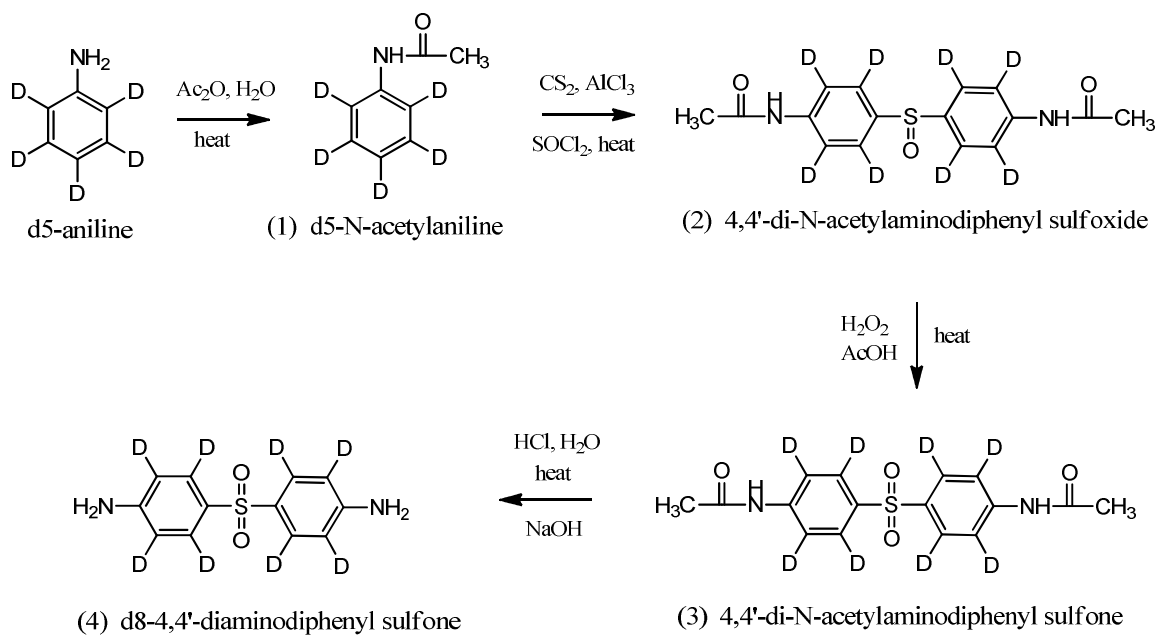
The ring deuterated N-acetylaniline was suspended in 80ml carbon disulfide (CS<sub>2</sub>), after which 15g aluminum trichloride (AlCl<sub>3</sub>) and 3ml sulfonyl chloride (SOCl<sub>2</sub>) were added. After the initial reaction subsided, the mixture was heated at reflux for 6hr, cooled to room temperature, and quenched by the addition of a 10% ammonium chloride solution in water. The mixture was filtered, and the solid was washed with water, dissolved in THF, filtered, and the filtrate concentrated under vacuum. The product, ring deuterated 4,4'-di-n-acetylaminodiphenyl sulfoxide, was recrystallized with MeOH/H<sub>2</sub>O (product 2, Scheme 2)

The ring deuterated 4,4'-di-N-acetylaminodiphenyl sulfoxide was suspended in 100ml glacial acetic acid. 10ml 30% H<sub>2</sub>O<sub>2</sub> was added to the suspension, and the mixture was allowed to stand for 3hr at room temperature. The mixture was then heated at 50°C for 2hr and subsequently refluxed until homogenous. The homogenous mixture was cooled to room temperature, 5ml 30%H<sub>2</sub>O<sub>2</sub> was added, and the mixture was stored overnight at 4°C. The mixture was concentrated under vacuum and then recrystallized with MeOH/H<sub>2</sub>O to yield ring deuterated 4,4'-di-n-acetylaminodiphenyl sulfone, (product 3, Scheme 2).

The ring deuterated 4,4'-di-n-acetylaminodiphenyl sulfone was suspended in 60ml 10% HCl, and heated at reflux for 1.5hr. At this point decolorizing carbon was added, and the mixture was

refluxed for 1hr, filtered while hot, and cooled to room temperature. A 10% NaOH solution was added to adjust the pH to 14, and the resulting precipitate was isolated by filtration, recrystallized with MeOH/H<sub>2</sub>O, and dried in a vacuum oven to yield 0.5g of the final product, ring deuterated 4,4'-diaminodiphenyl sulfone, d8-44DDS (product 4, Scheme 2).

**Scheme 2.** Synthesis of d8-44DDS



### Ring Deuterated d8-33DDS Synthesis

The preparation of 100% nitric acid by the reaction of sulfuric acid with potassium nitrate is accomplished for use later in the synthetic procedure. Vacuum distillation is used to collect the nitric acid (Scheme 3).

**Scheme 3.** Preparation of 100% Nitric Acid Via Vacuum Distillation

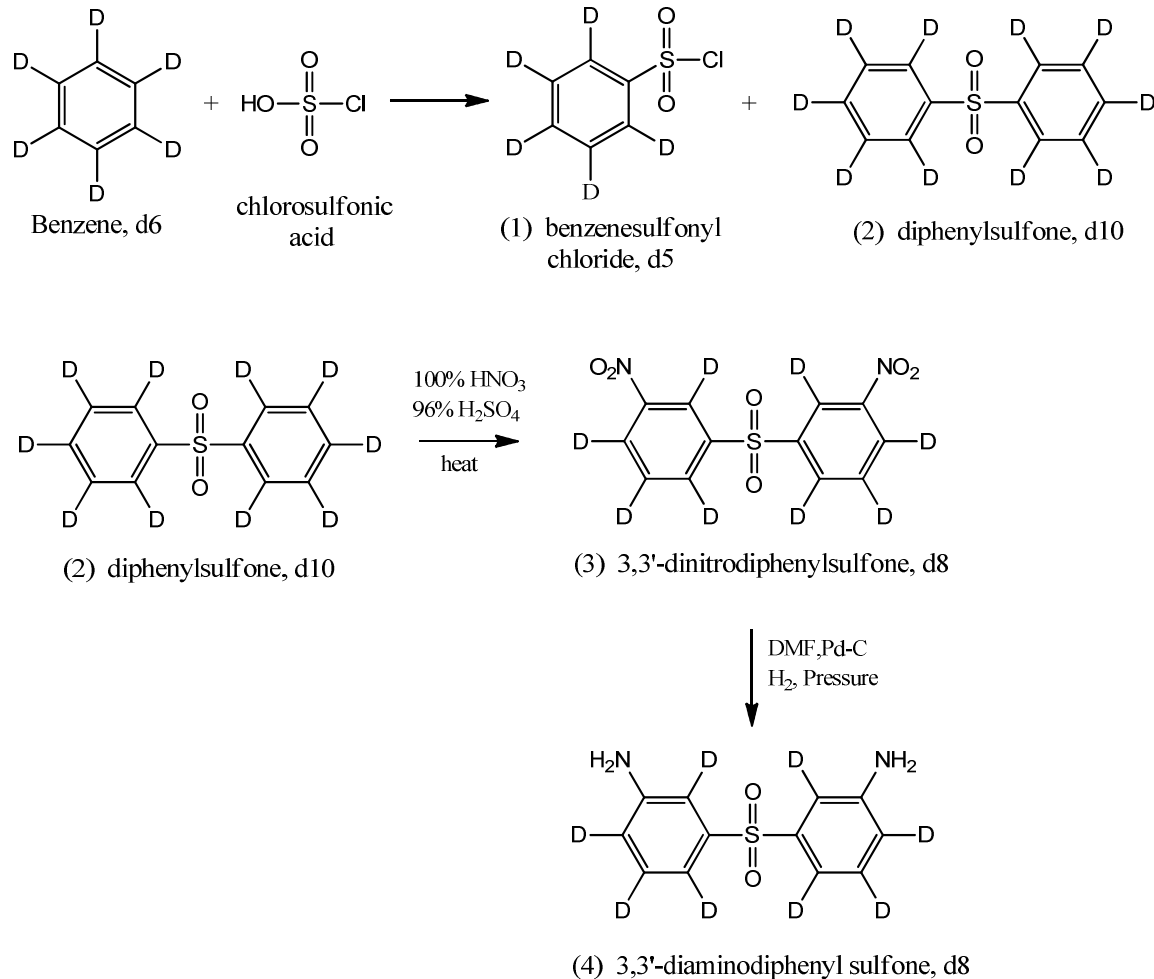


The first step in the synthesis of d8-33DDS is the dropwise addition of chlorosulphonic acid (11.65g, 0.1 mol) to ring deuterated benzene (16.82g, 0.2 mol). The reaction mixture is kept at 20°C and allowed to stir for 30min. This reaction mixture is then poured on ice and extracted with chloroform. The chloroform is distilled off the reaction mixture under reduced pressure. After distillation, the residue is filtered to leave a filtrate composed of the colorless liquid ring deuterated benzenesulfonyl chloride (product 1, Scheme 4) and a white filter cake, ring deuterated diphenyl sulfone; 75% yield, m.p. 128°C (product 2, Scheme 4).

The deuterated diphenyl sulfone (10.96 g, 0.048 mol) was suspended in 30 ml of methylene chloride and dissolved with the aforementioned 100wt.% nitric acid (7.55g, 0.117mol). 14.8g of 96wt.% sulphuric acid was then added dropwise under reflux with stirring over a period 4 hours at the boiling temperature of the solution (50°C). After cooling to 20°C, the reaction product, ring deuterated 3,3'-dinitrodiphenyl sulfone, precipitated out of solution and was filtered off, washed twice with 100 ml of methylene chloride and then once with water and dried at 100°C. The ring deuterated 3,3'-dinitrodiphenyl sulfone was then purified by recrystallized from DMF; 98% yield, m.p. 203°C (product 3, Scheme 4).

DMF was added dropwise to the ring deuterated 3,3'-dinitrodiphenyl sulfone (14.88g, 0.047mol) until fully dissolved, and 10wt.% palladium catalyst on wet carbon powder (0.74g) was added. This mixture was placed into the hydrogenation flask of a Parr apparatus to reduce the nitro groups. The hydrogenation was carried out under a pressure of 3.5atm at ambient temperature until the reaction mixture would not react further with hydrogen. The catalyst was filtered off, and the filtrate was placed in a vacuum oven at 80°C and reduced pressure to pull off the solvent, DMF. The final product, ring deuterated 3,3'-diaminodiphenyl sulfone, was a yellow solid which was purified by recrystallization from MeOH and charcoal; m.p. 174°C (product 4, Scheme 4).

#### Scheme 4. Synthesis of d8-33DDS



#### Network Synthesis

Four deuterated resin samples were prepared to selectively study the amine rings and epoxy rings in 33DDS/DGEBA and 44DDS/DGEBA matrices. The d8-DGEBA was reacted with 33DDS and 44DDS to study the effect on epoxy ring motions of the meta vs. para curative. Both of the ring deuterated amines, d8-33DDS and d8-44DDS were reacted with DGEBA to study the motions of the amine rings and compare them to one other and the epoxy rings. Due to the high cost of the deuterated starting materials, the difficulty of the syntheses, and the quantities needed for deuterium NMR analysis, only 300mg of epoxy/amine samples were

prepared. Samples were reacted stoichiometrically (2:1 epoxy:amine ratio, equaling a 1:1 functional group ratio) assuming full conversion of the amine. The amines were solubilized into the epoxies using GPC vials as reaction vessels and an oil bath to supply heat. Deuterated amines proved more difficult to solubilize into DGEBA than non-deuterated amines, and the deuterated DGEBA acted as a less efficient solvent for the amines. Thus, temperatures of up to 150°C were required to solubilize the amines. Once the amines were solubilized into the epoxies, the samples were cured 5 hours at 125°C and 2 hours at 225°C. The deuterated monomers cured more slowly than nondeuterated amines, requiring post cures of multiple days at 200°C and 225°C for fully cured networks. The deuterated amines underwent particularly slow cures, exhibiting changes in deuterium lineshape until fully cured.

## **Deuterium Solid State Nuclear Magnetic Resonance Methods**

### **Instrumentation and pulse sequences**

Solid state NMR spectra were acquired on a Varian <sup>UNITY</sup>INOVA NMR spectrometer operating at a frequency of 61.4 MHz for deuterium and equipped with a Tecmag wideband <sup>2</sup>H probe. The standard quadrupolar-echo pulse sequence was employed with 90° pulse widths of 2.5µs and a delay of 25µs between pulses. A dwell time of 0.25µs, corresponding to a spectral width of 2.0MHz was used. The number of time domain points sampled during acquisition was 1024, with the data zero-filled to 16,384 points prior to application of Fourier transformation. The number of scans collected for spectra varied depending upon signal strength, which is effected by a number of variables, including temperature and quantity of deuterium present in the sample. The recycle delay between scans was varied from 1-10s, depending upon the spin-lattice relaxation time of the slowest deuterium motion at that particular temperature. Temperature

control was attained by placing a thermocouple directly into the sample chamber and adjusting heater power until the desired temperature was reached.

Solid state deuterium spin-lattice relaxation data was obtained using the saturation-recovery method with a recycle delay of 500ms for all analyses. Here a series of ten 90° pulses separated by 1ms was applied prior to the quadrupolar echo sequence in order to suppress initial magnetization, with signal recovery monitored as a function of time. Spin-lattice relaxation values were obtained by curve fitting the integral areas.

### **Quadrupolar echo lineshape analysis**

Routine spectra were obtained using the standard quadrupolar echo delay sequence.

Quadrupolar echo spectra were obtained at 25, 50, 75, 100, 125, 140, 160, 180, and 200°C for all four samples, 33DDS/d8-DGEBA, 44DDS/d8-DGEBA, d8-33DDS/DGEBA, and d8-44DDS/DGEBA. Information concerning type and rate of motion is obtained from the comparison of experimental data to spectral simulation. In this work, simulated lineshapes are calculated using EXPRESS software.<sup>86</sup>

### **Deuterium NMR spin-lattice relaxation analysis**

Spin-lattice relaxation studies were implemented in order to discriminate various motional rates of motion for the selectively deuterated phenyl rings. Experiments were performed at 25, 50, 75, 100, 125, 140, 160, 180, and 200°C for 33DDS/d8-DGEBA, 44DDS/d8-DGEBA, and d8-44DDS/DGEBA. Two experiments were obtained at each temperature for each sample, and the results averaged.

Figure 26 shows an example of a saturation recovery experiment for 44DDS/d8-DGEBA at room temperature. For clarity, only 11 delay times are shown; typically 23-24 delay times are measured to ensure a sufficient number of data points for fitting. Note that a distinct lineshape change can also be observed. Initially, only the inner splittings are present at short delay times, with the outer splittings appearing as the delay time increases.

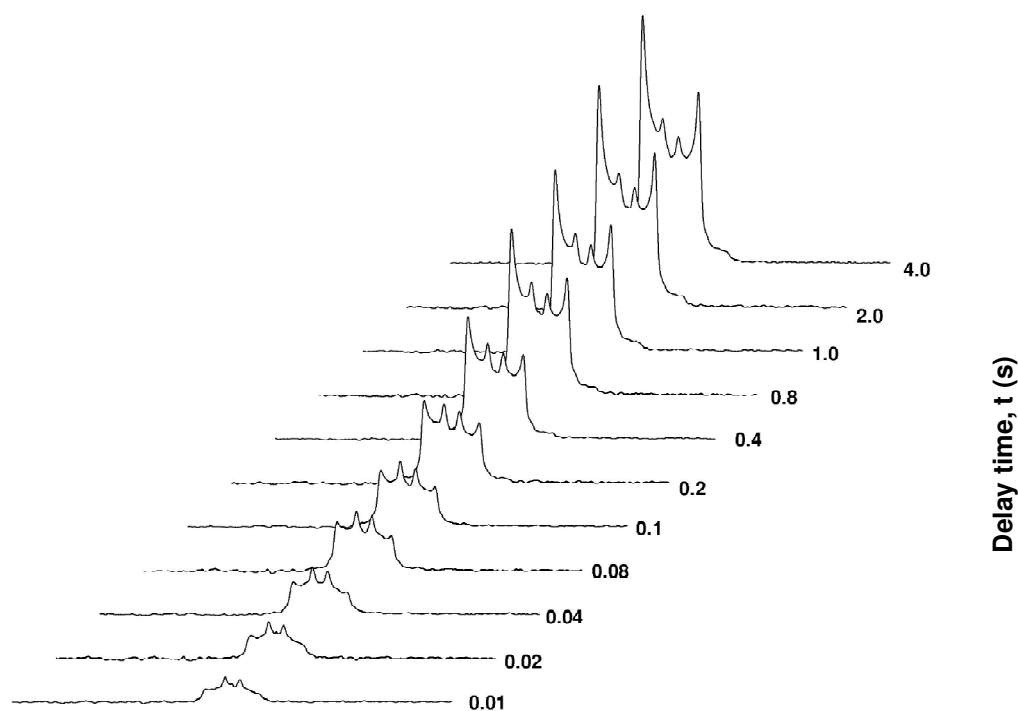


**Figure 26.** 44DDS/ d8-DGEBA saturation recovery spectra

The data was fitted to an exponential expression in order to determine spin-lattice relaxation times for phenyl ring motion. Equation 11 shows the relationship between integral area, delay time, and spin-lattice relaxation time:

$$M(t) = M_0 * (1 - e^{\frac{-t}{T_1}})$$

where:  $M(t)$  = signal (or integral area) as a function of delay time,  $t$

$M_0$  = equilibrium signal at infinite time

$t$  = delay time

$T_1$  = spin-lattice relaxation time

**Equation 11.** Theoretical exponential equation relating  $T_1$  time to integral area.

Equation 11 assumes only one rate of motion, and therefore only one spin-lattice relaxation time. Here the data was fitted to one component, two component, and three component exponentials; it was determined that a two component exponential fit was sufficient to describe spin-lattice relaxation behavior. A modified two component exponential equation used for fitting is shown in Equation 12. The red line in Figure 27 shows the fit produced by Equation 12. Chi squared values were 0.999 – 0.997 for all samples at all temperatures.

$$M(t) = M_1 * \left( e^{\frac{-t}{T_{11}}} \right) + M_2 * \left( e^{\frac{-t}{T_{12}}} \right) + y_0$$

where:  $M(t)$  = signal (or integral area) as a function of delay time,  $t$

$M_1$  = equilibrium signal due to the first motion

$M_2$  = equilibrium signal due to the second motion

$t$  = delay time

$T_{11}$  = spin-lattice relaxation time of first motion

$T_{12}$  = spin-lattice relaxation time of second motion

$y_0$  = fitting factor

**Equation 12.** Modified two component exponential equation used for curve fitting.

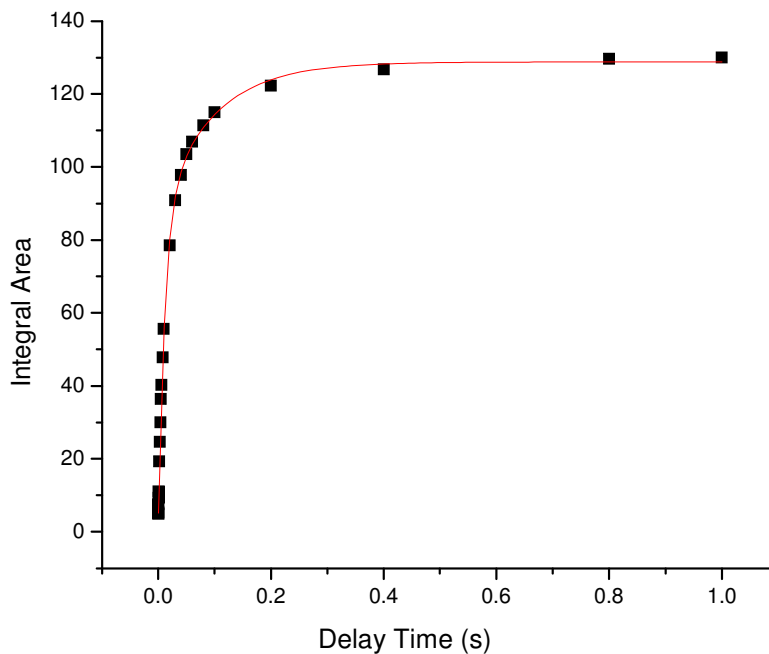


**Figure 27.** Two component curve fitting for saturation recovery experiment.

### *Spin-lattice Relaxation Analysis*

Spin-Lattice relaxation ( $T_1$ ) studies were performed to identify basic motional contributions to lineshape. A two component fit closely matches the spin-lattice experimental data, confirming the presence of two distinct phenyl ring with significantly different rates of motion. These ring motions can be explained in terms of a fast  $180^\circ$   $\pi$ -flipping motion and a slow or restricted phenyl ring flip motion possessing a small flip angle. The spin-lattice relaxation times are summarized in Table 14.

**Table 14.** Spin-Lattice Relaxation Times Calculated from Two Component Fitting for Slow and Fast Phenyl Ring Motions 25 – 200°C

T (°C)	33DDS/d8-DGEBA		44DDS/d8-DGEBA		d8-44DDS/DGEBA	
	fast	slow	fast	slow	fast	slow
<b>25</b>	0.049	0.83	0.059	0.99	0.42	1.95
<b>49</b>	0.026	0.55	0.032	0.69	0.32	1.39
<b>75</b>	0.020	0.38	0.022	0.49	0.14	0.81
<b>100</b>	0.015	0.20	0.016	0.29	0.071	0.58
<b>123</b>	0.012	0.090	0.012	0.13	0.045	0.39
<b>140</b>	0.011	0.042	0.011	0.08	0.039	0.34
<b>160</b>	0.013	N/A	0.013	0.11	0.028	0.31
<b>180</b>	0.011	N/A	0.013	0.12	0.019	0.14
<b>200</b>	0.0087	N/A	0.012	0.14	0.015	0.10

Excluding behavior of the slow motional component above 160°C, the spin-lattice relaxation values indicate that the motion of the epoxy rings is similar regardless of amine. The epoxy rings in the 33DDS/d8-DGEBA sample exhibit slightly faster motions than the 44DDS/d8-DGEBA sample with similar trends for both fast and slow motions. At 160°C, a one component fit is sufficient to characterize  $T_1$  behavior of the 33DDS/d8-DGEBA sample. At this temperature, all the epoxy rings appear to undergo identical ring motions. Since the  $T_g$  of 33DDS/DGEBA is 180°C, it is likely that upon approaching  $T_g$ , restriction of ring motion is eliminated.

In the 44DDS/d8-DGEBA sample, the  $T_1$  values of the slow motion display the same behavior observed in 33DDS/d8-DGEBA, decreasing from 25°-140°. However, above 140°C, the spin-lattice relaxation time unexpectedly increases. One possible explanation for this  $T_1$  anomaly is a change in motional mode.

The d8-44DDS/DGEBA sample exhibits two distinct spin-lattice values, i.e., motions, throughout the temperature range analyzed. As expected, the  $T_1$  times of both increase with increasing temperature. It is important to note the relaxation behavior of the 44DDS rings is substantially slower than the DGEBA rings, indicating the amine rings experience more hindrance to bond rotation than the epoxy rings. This is clearly demonstrated by comparing the behavior of the epoxy and amine rings in d8-44DDS/DGEBA and 44DDS/d8-DGEBA. The difference in motional behavior in the epoxy and amine rings is likely due to the presence of ether and quaternary carbon groups adjacent to the DGEBA ring as opposed to amine and sulfone groups adjacent to the 44DDS ring. Ether bonds are well known for allowing facile ring flipping in adjacent phenyl rings.<sup>87 88 89</sup> Additionally, the amine group on 44DDS is most likely a tertiary amine, which increases steric hindrance (Figure 28).

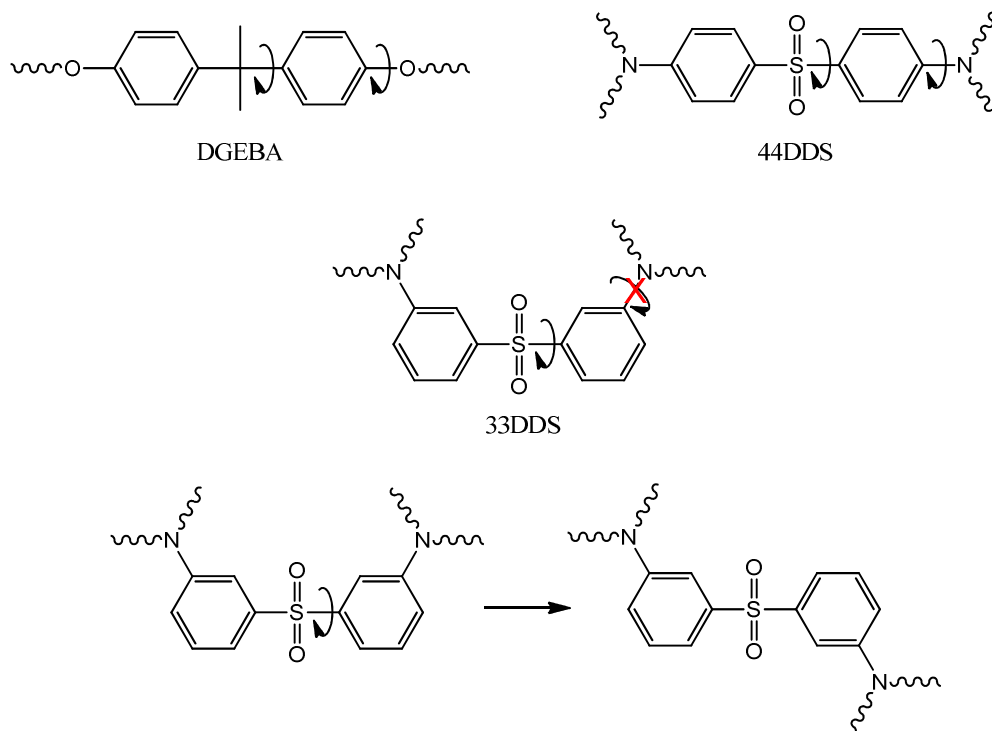


**Figure 28.** DGEBA rings possess more facile phenyl ring  $\pi$ -flipping than 44DDS rings. 33DDS lacks an axis of symmetry making phenyl ring  $\pi$ -flips impossible.

Figures 28, 30, and 32 show plots of  $\log T_1$  time vs. inverse temperature. Here linear, i.e., Arrhenius, behavior indicates that no major changes in the type of motion are occurring. In some studies, such as  $^1\text{H}$  solid state NMR spectroscopy, the activation energy of the motion may be obtained directly from the slope of the  $\log T_1$  time vs.  $1/T$  plot.<sup>90</sup> However, in deuterium studies, the actual correlation time,  $\tau_c$ , obtained with spectral simulation, is necessary to create an Arrhenius plot of  $\log \tau_c$  vs.  $1/T$ . This work is currently underway.

In the  $\log T_1$  time vs.  $1/T$  plot for 33DDS/d8-DGEBA (Figure 28), the slow motion shows fairly linear behavior at low temperatures (25-75°C), but starts to deviate at 100°C and disappears by 180°C. The fast motion is linear up to 140°C but shows a slight increase at 160°C, the same temperature at which the slow/restricted motion disappears. This behavior is most likely due to a combination of (1) Decreasing contribution of the slow motional component to the point that it can no longer be accurately determined by data fitting, and (2) The introduction of additional motion as temperature approaches  $T_g$ . The decreasing contribution of the slow motional component is shown in Figure 29.

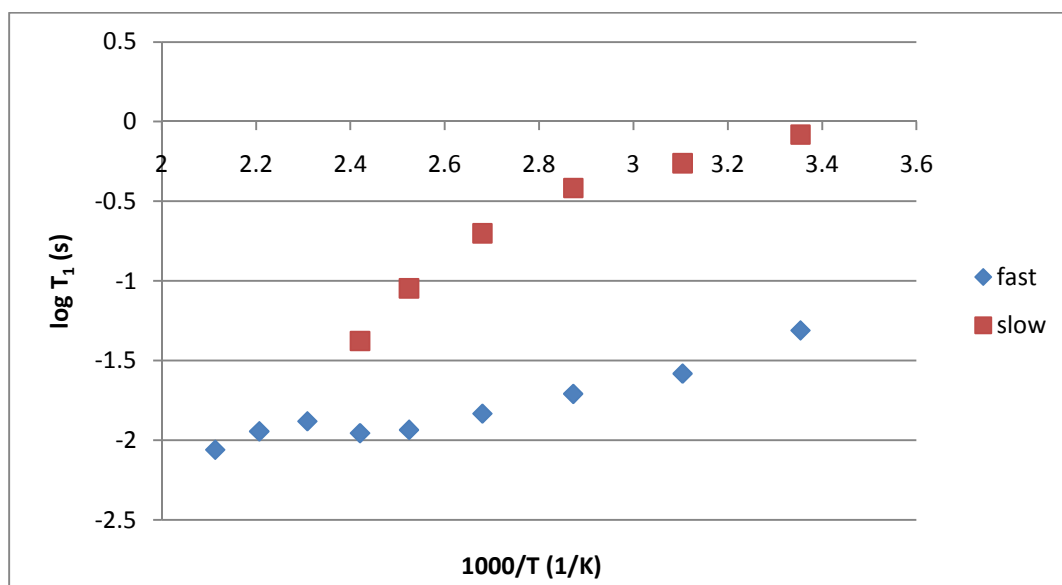


**Figure 28.** Log  $T_1$  time vs. inverse temperature plot for 33DDS/d8-DGEBA.

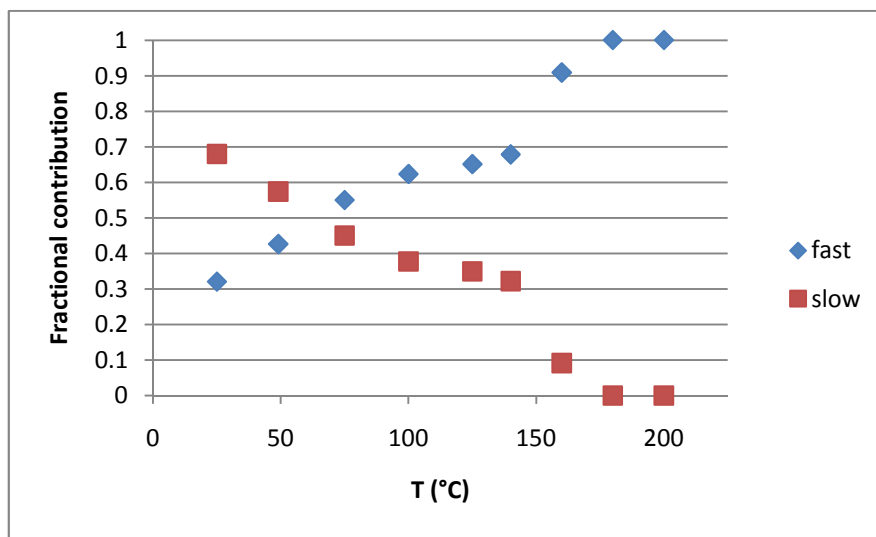


**Figure 29.** Fractional contribution of fast and slow motion in 33DDS/d8-DGEBA

The log  $T_1$  time vs.  $1/T$  plot of 44DDS/d8-DGEBA is shown in Figure 30. The slow component shows similar behavior to the 33DDS/d8-DGEBA sample, decreasing linearly from 25-100°C, then dropping significantly, due to less restricted motion. As noted previously, the slow component exhibits odd behavior above 140°C, with  $T_1$  values increasing with increasing temperature. As previously stated, this anomaly may be due to a change in the motional mode. However, unlike 33DDS/d8-DGEBA, 44DDS/d8-DGEBA is still well below  $T_g$  at these temperatures ( $T_g = 225^\circ\text{C}$ ); thus, this behavior cannot be regarded as a  $T_g$  effect.

Figure 31 shows the fractional contribution of fast and slow motions based on the integral area for 44DDS/d8-DGEBA. As observed in the 33DDS/d8-DGEBA sample, the contribution of the slow motion decreases while the fast motion increases with increasing temperature. However, for 44DDS/d8-DGEBA, the slow motion never completely disappears due to its distance from  $T_g$  at 225°C.

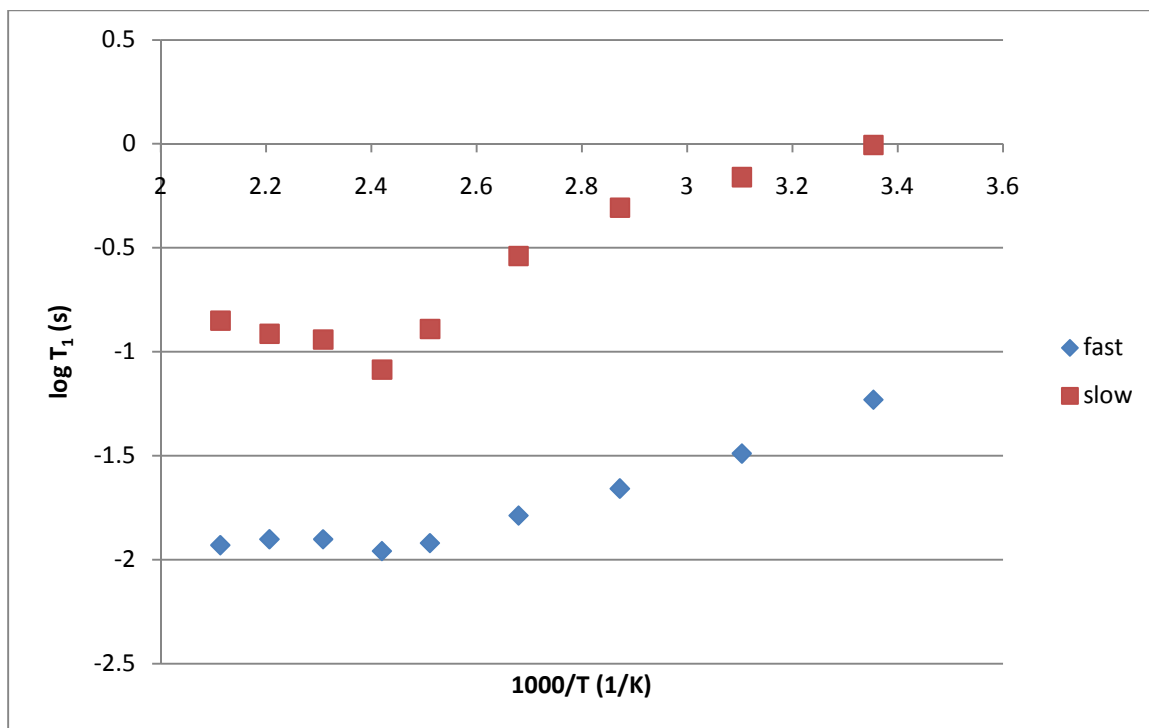


**Figure 30.** Log T<sub>1</sub> time vs. inverse temperature plot for 44DDS/d8-DGEBA

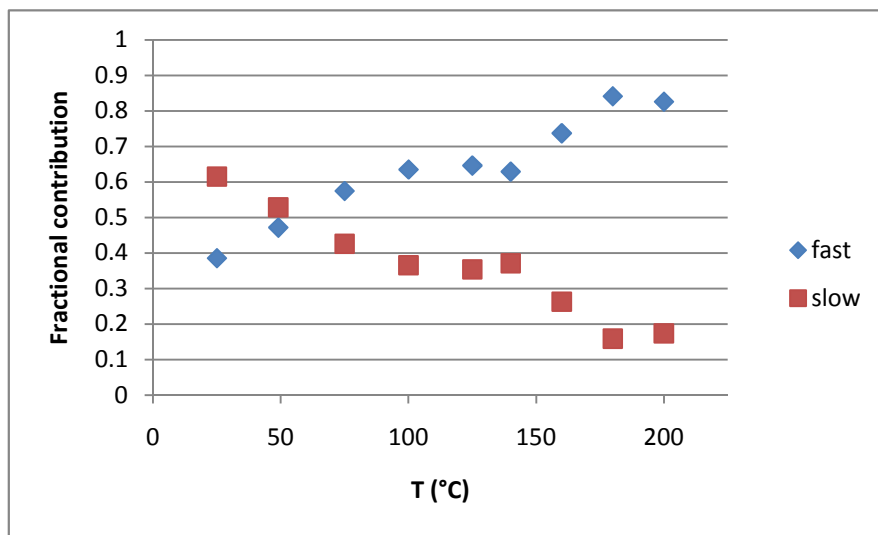


**Figure 31.** Fractional contribution of fast and slow motion in 44DDS/d8-DGEBA

Figure 32 shows the log T<sub>1</sub> time vs. 1/T plot for d8-44DDS/DGEBA. Both fast and slow motional components show Arrhenius behavior throughout the temperature range studied, with

the slower component motion remaining linear in the  $\log T_1$  time vs.  $1/T$  plot up to  $200^\circ\text{C}$ . This is strong evidence that the amine rings are significantly more restricted than the epoxy rings.

The motional contribution of the fast and slow motions based on integral area is seen in Figure 33. Although an irregularity exists at  $50^\circ\text{C}$ , the trend clearly shows the decrease of the slow motion's contribution as temperature is raised. However, unlike the epoxy rings in which the slow, restricted motion continually decreased as temperature increased, the contribution of the slow motion in the 44DDS rings levels off at  $160^\circ\text{C}$  at a level of about 40%. This supports the hypothesis that the amine rings possess greater motional hindrance than the epoxy rings.

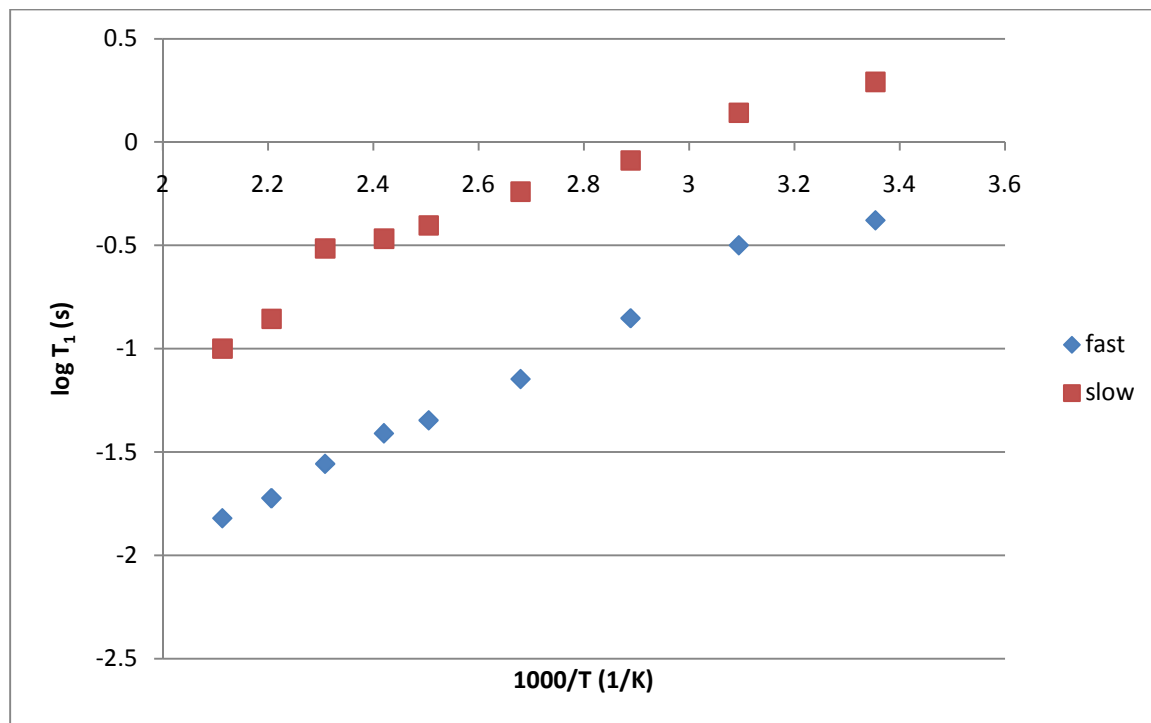


**Figure 32.** Log  $T_1$  time vs. inverse temperature plot for d8-44DDS/DGEBA

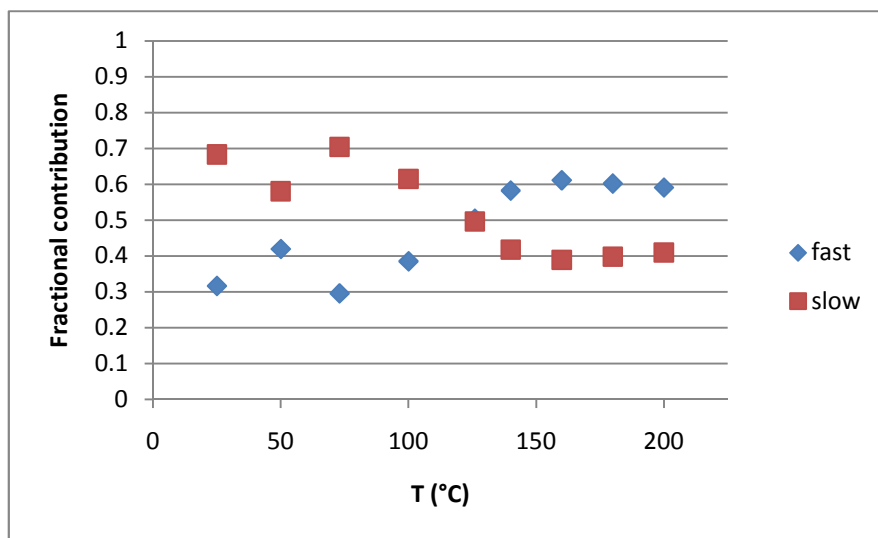


**Figure 33.** Fractional contribution of fast and slow motion in d8-44DDS/DGEBA

### ***Quadrupolar Echo Lineshape Analysis***

Solid state deuterium NMR spectral lineshapes were used to study the motional behavior of d8-33DDS/DGEBA, 33DDS/d8-DGEBA, d8-44DDS/DGEBA, and 44DDS/d8-DGEBA.

Deuterium NMR lineshapes provide relevant information concerning the modes and rates of molecular motion present in the matrices. The asymmetry of the lineshapes is due to a distortion caused by the presence of phase transients. However, this distortion is a common spectroscopic artifact in solid state  $^2\text{H}$  NMR spectroscopy and does not affect the validity of the results.

In  $^2\text{H}$  lineshape analysis, static or restricted phenyl ring motions yield spectra in the form of a Pake doublet; the spectral splitting between the main peaks, or “horns,” is  $\frac{3}{4}$  the quadrupolar coupling constant.<sup>3,91,92</sup> The presence of motion will dramatically alter this lineshape, based both on the rate and type of motion. Facile phenyl ring  $\pi$ -flipping is typically observed as a collapsed Pake pattern with closely separated horns located between upfield and downfield shoulders.<sup>93</sup> A static lineshape is observed in the d8-44DDS/DGEBA sample at 25°C; however, as the

temperature increases, both a static and motionally averaged lineshape can be discerned in the spectrum up to 200°C. This overlapping spectral behavior is most clearly observed in the d8-44DDS/DGEBA lineshape at 125°C.

Two other types of motions are also observed. The appearance of a single narrow peak at 0kHz is indicative of a fully motionally averaged system, whereby sufficient mobility exists so that the effective quadrupolar coupling ( $C_Q$ ) is averaged to approximately zero. This behavior is observed in liquids or polymers at temperatures above glass transition. In addition, a nondescript, “very fast” motion, termed libration, is also present, which effectively reduces  $C_Q$ . In essence, the libration is the summation of all motions in the polymer which affect the phenyl ring other than phenyl ring flipping. Motions that create small amplitude main chain motions, which, in turn, affect phenyl rings, are the main source of libration.

Figure 34 compares the  $^2\text{H}$  spectra of the ring-deuterated amine (left) and ring-deuterated epoxy (right) in the 33DDS/DGEBA matrix. The deuterated 33DDS cured with DGEBA shows a Pake pattern consistent with restricted ring motion until reaching 180°C ( $T_g$ ), at which point a narrow peak in the center of the Pake pattern appears. This center peak indicates a small amount of highly mobile rings. The center peak becomes significantly more prominent at 200°C, as the sample is heated to well above  $T_g$ . The prominence of the outer splittings above  $T_g$  indicates most 33DDS rings remain restricted. 33DDS rings between crosslinks cannot undergo rapid ring flipping due to their meta substitution, which prevents their possessing an axis of symmetry about which to flip. For this reason, even at 200°C, the broad splittings at  $\pm 63.5\text{kHz}$  never collapse into narrow splittings. The growth of the center peak above  $T_g$  could be indicative of 33DDS molecules on chain ends, which have increased mobility above  $T_g$ .

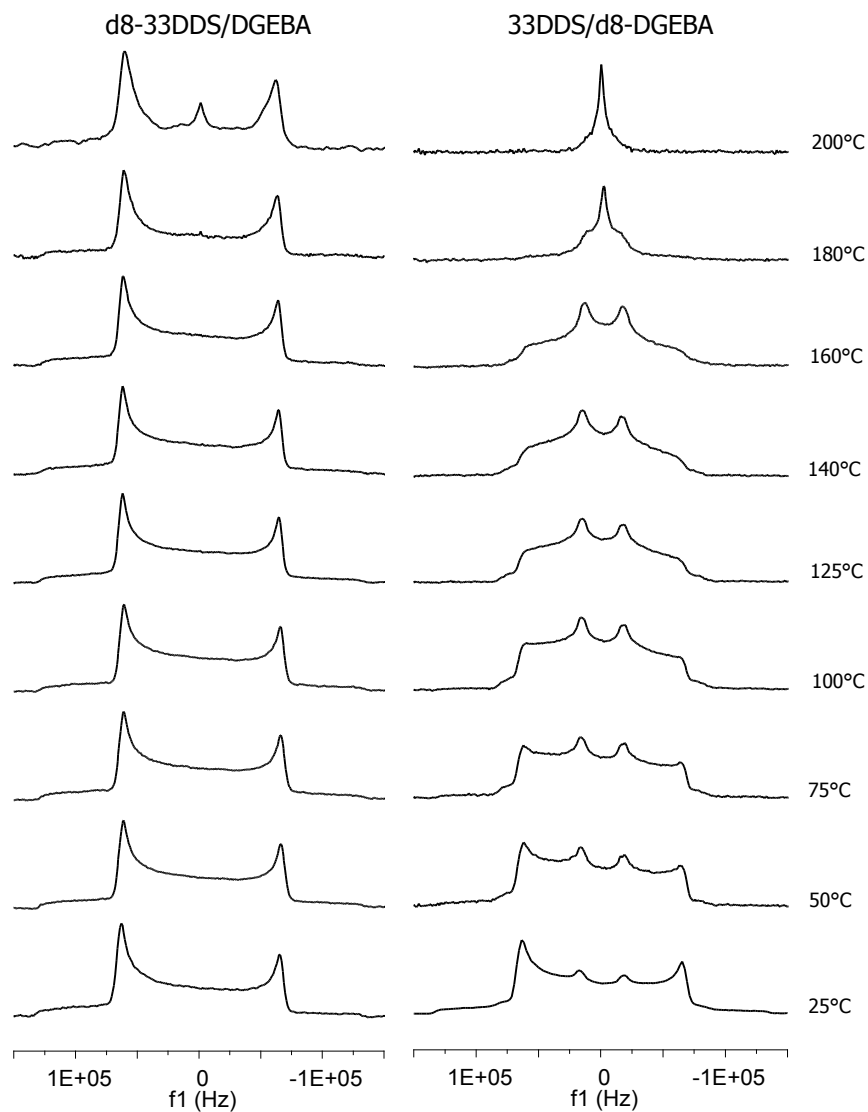


**Figure 34.**  $^2\text{H}$  NMR spectra of d8-33DDS/DGEBA (left) and 33DDS/d8-DGEBA (right)

Evidence of librational averaging is observed in the d8-33DDS/DGEBA sample by the reduction of the splittings from  $\pm 63.5\text{kHz}$  at  $25^\circ\text{C}$  to  $\pm 61.75\text{kHz}$  at  $200^\circ\text{C}$ . Since the d8-33DDS/DGEBA  $^2\text{H}$  lineshapes do not undergo significant motional averaging throughout the entire temperature range, this sample provides the best opportunity to study libration. The relationship between the quadrupolar coupling constant ( $C_Q$ ) and the spectral splitting of the Pake doublet is given by Equation 13.

$$C_Q = \frac{4}{3} * S$$

where:  $C_Q$  = quadrupolar coupling constant

$S$  = the frequency difference between the outer splittings

**Equation 13.** Calculation of quadrupolar coupling constant based on outer splitting.

The theoretical  $C_Q$  for a completely static C-D phenyl ring bond is 180kHz, which corresponds to a spectral separation of 135kHz between the outer splittings. At room temperature in the d8-33DDS/DGEBA sample, this spectral separation is 127kHz, indicating a significant amount of libration is occurring at room temperature. The spectral separation between splittings for d8-33DDS/DGEBA decreases from 127kHz to 123.5kHz as temperature is raised from 25°C to 200°C, corresponding to a decrease in  $C_Q$  from to 169.5kHz to 164.5kHz. The effective amplitude of the librational motion can be calculated from Equation 14.

$$\langle C_Q \rangle = C_Q * \frac{3\cos^2(\theta)}{2}$$

where:  $\langle C_Q \rangle$  = the average quadrupolar coupling constant observed

$C_Q$  = the theoretical coupling constant for static phenyl C-D bonds (180kHz)

$\theta$  = librational amplitude

**Equation 14.** Relation of  $C_Q$  to librational amplitude.

For d8-33DDS/DGEBA, the librational amplitude changes from 37° to 39° as the temperature changes from 25°C to 200°C. This value is in good agreement with a librational amplitude of 37° for similar aromatic crosslinked epoxies observed by Ingelfield and coworkers.<sup>3</sup>

It is clear from Figure 34 that the epoxy rings in 33DDS/d8-DGEBA display a substantially different behavior than the amine rings of d8-33DDS/DGEBA. At 25°C the outer splittings at  $\pm 63$ kHz and shoulders at  $\pm 136$ kHz are prominent, with the inner splittings at  $\pm 18$ kHz also present at room temperature, indicating some fast 180° ring flips are occurring at 25°C. As temperature is increased, the restricted lineshape diminishes while the fast motion increases until a lineshape indicative of facile ring flipping is observed at 140°C. At 160°C, the lineshape has narrowed even further, and has changed appearance, indicating an additional mode of motion is occurring. At 180°C, a narrow line is observed, and by 200°C, 20°C above  $T_g$ , the lineshape has fully collapsed to a single peak attributed to long range cooperative (liquid-like) motions occurring above  $T_g$ .

Figure 35 shows the deuterium lineshape of the amine rings (left) and epoxy rings (right) for 44DDS/DGEBA. The d8-44DDS rings initially display restricted motional behavior at 25°C, with outer splittings at  $\pm 63.5$ kHz and shoulders at  $\pm 140$ kHz. However, at 50°C, inner peaks at  $\pm 19$ kHz are visible, indicating  $\pi$ -flipping motions. These inner peaks continue to grow while the outer peaks decrease up to 200°C; at this temperature the lineshape is indicative of facile ring flipping motions. It should be noted that 200°C is the upper temperature limit of the NMR probe and is 25°C below the  $T_g$  of 44DDS/DGEBA. This prevents studies above  $T_g$  whereby liquid-like behavior could be observed.

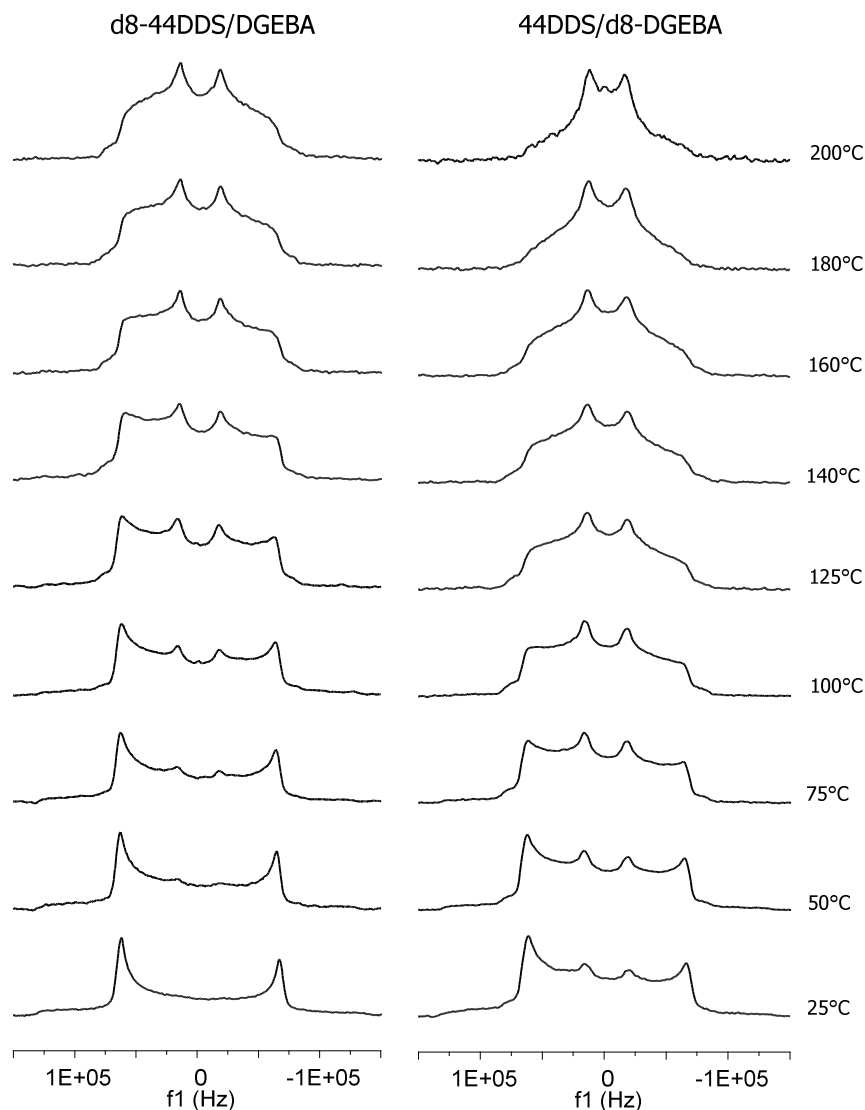
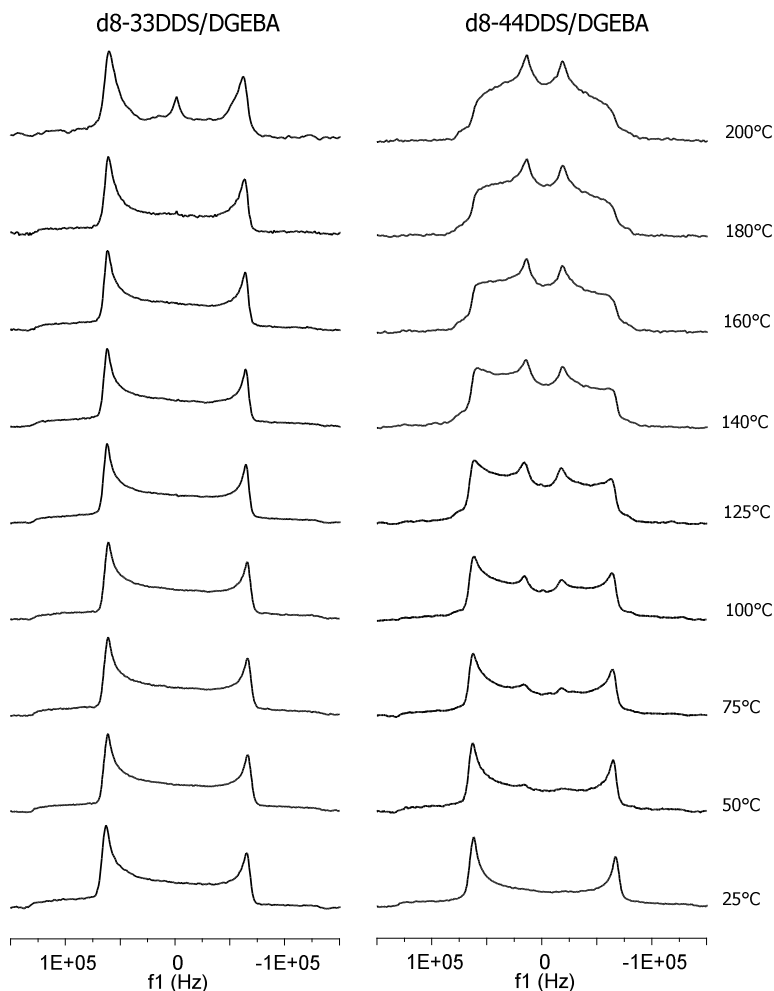


**Figure 35.**  $^2\text{H}$  NMR spectra of d8-44DDS/DGEBA (left) and 44DDS/d8-DGEBA (right).

The motions of epoxy rings in 44DDS/d8-DGEBA are shown on the right side of Figure 35. At 25°C, both outer ( $\pm 63$ kHz) and inner ( $\pm 18$ kHz) splittings are seen, indicating restricted  $\pi$ -flipping motions are present. The outer splittings and shoulders ( $\pm 136$ kHz) decrease and inner splittings become the dominant lineshape as temperature is increased to 125°C. Above 125°C, additional lineshape changes are observed due to additional modes of motion and increased rate of motion.

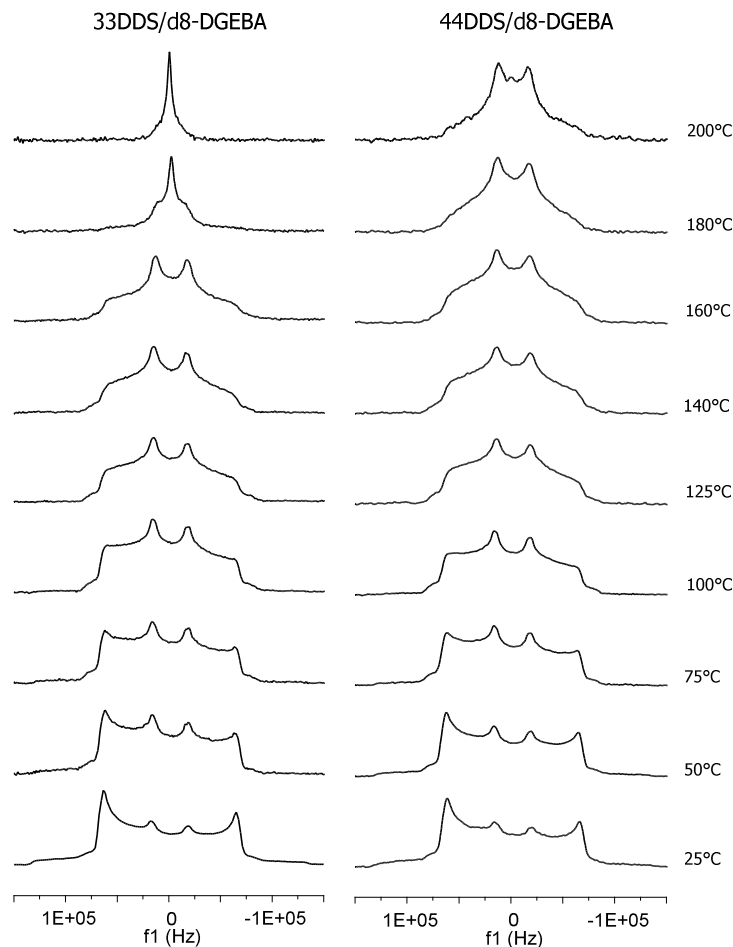
Interestingly, the peak shape of the epoxy rings in 44DDS/d8-DGEBA at 25°C closely matches that of the amine rings in d8-44DDS/DGEBA at 100°C. This delta of 75°C between the lineshapes of the epoxy and amine holds throughout the lineshape analysis, such that ring motions in the amine are observed at temperatures 75°C higher than in the epoxy. Since both the epoxy and amine phenyl rings possess an axis of rotation, this increased activation energy for the amine rings is likely due to the sulfone group hindering motion, as evidenced by the  $T_1$  experiments.

Figure 36 compares the  $^2\text{H}$  spectra of the meta-substituted amine (33DDS) vs. the para-substituted amine (44DDS) when both have been reacted with DGEBA. As observed previously, 33DDS exhibits no ring flipping, but does show the presence of some sites undergoing rapid, isotropic motion, i.e., the narrow center peak, above  $T_g$ . The amine rings of 44DDS show phenyl ring flipping, but no evidence of rapid, near isotropic motion since the matrix never reaches  $T_g$ .



**Figure 36.**  $^2\text{H}$  NMR spectra of d8-33DDS/DGEBA (left) and d8-44DDS/DGEBA (right).

The effect of meta vs. para curative substitution on the epoxy ring motions are examined by comparing the solid-state  $^2\text{H}$  lineshapes of 33DDS/d8-DGEBA (left) vs. 44DDS/d8-DGEBA (right), Figure 37. The epoxy lineshapes are almost identical between 25°C and 125°C; however at 140°C, 33DDS/d8-DGEBA begins to show a larger reduction of the outer splittings. This lineshape change is accentuated at 160°C. Above 160°C, the lineshapes for the two epoxies completely differ, with the 33DDS/d8-DGEBA narrowing into a single peak, while the 44DDS/d8-DGEBA material exhibits a solid-state pattern characteristic of rapid ring motion.



**Figure 37.**  $^2\text{H}$  NMR spectra of 33DDS/d8-DGEBA (left) and 44DDS/d8-DGEBA (right).

Linear trends in  $\log T_1$  time vs.  $1/T$  plots are observed for the fast motional component in all three samples (Figures 28, 30 and 32) with the exception of a small deviation from linearity in the deuterated epoxy ring samples at 160°C. In 33DDS/d8-DGEBA, this is attributed a small contribution of the slow motion being averaged in with the fast component or a change in motional mode due to the proximity to  $T_g$  (180°C). In 44DDS/d8-DGEBA, the change in slope of the slow motional component is explained by a change in motional mode; however, as the sample is still well below  $T_g$ , the cause of this change is unknown.

Further deuterium NMR experimentation at low temperatures is required to further investigate the motional behavior of these systems. Of particular interest is to determine whether the librational motion can be frozen out such that the theoretical value of  $C_Q = 180$  for a static C-D phenyl ring bond is observable. Additionally, spin-lattice relaxation studies for the d8-33DDS/DGEBA should be obtained in the 25-200°C temperature range to compare to data already obtained for the other systems. Due to the highly static nature of the 33DDS rings, we would expect to see evidence of slow, restricted motions for most of the temperature range. Low temperature  $T_1$  analysis on all four samples would provide interesting information on the rate of motions at low temperatures and temperature at which various motions became “frozen out.”

In future  $^2\text{H}$  lineshape simulation work, ring flipping motions will be more accurately described using a stretched exponential equation (KWW) to account for a range of motional rates and a simple Gaussian distribution of flip angles. Librational motions will be pre-averaged in to the lineshape by adjusting the quadrupolar coupling constant. The completion of these complex simulated lineshapes will allow experimental lineshapes to be accurately replicated, thus describing the complex motions of the phenyl rings.

Additionally,  $^2\text{H}$  lineshape simulations will provide correlation times for the motions at different temperatures. From this data it is possible to calculate activation energies as well as permit comparison of NMR results to relaxations observed with dynamic mechanical analysis and dielectric spectroscopy. This comparison can provide evidence regarding the correlation between phenyl ring motions and the sub- $T_g$  transitions responsible for bulk mechanical properties of matrices such as modulus, toughness, and strength,<sup>5,6,7</sup> and thus further our understanding of the relationship between chemical composition and mechanical properties in polymers.

## **RESULTS PART V**

### **INVESTIGATION OF MOLECULAR MOTIONS OF EPOXY NETWORKS VIA $^{13}\text{C}$ NMR SPECTROSCOPY**

#### **Introduction**

Solid state NMR spin-lattice relaxation studies give ideal opportunity to study molecular motions in crosslinked glassy solids. Carbon spin-lattice relaxation ( $T_1$ ) times are a function of both the rate and type of motions at the carbon site. Generally in the solid state,  $T_1$  times are directly related to molecular motions, with shorter  $T_1$  times indicating faster motions and longer  $T_1$  times indicating slower motions. Proton spin-lattice relaxation values do not offer information about specific molecular level motions because proton spin diffusion homogenizes  $T_1$  times. However,  $^{13}\text{C}$  atoms are isolated from one another due to their 1.1% natural abundance. Since the rate and type of molecular motions influence  $T_1$  values, spin-lattice relaxation experiments should provide information concerning molecular motion at  $^{13}\text{C}$  sites.

In deuterium NMR spectroscopy, spin-lattice relaxation is dominated by the quadrupolar moment; however, mechanisms available for spin-lattice relaxation are more numerous in  $^{13}\text{C}$  experiments. Dipole-dipole interactions are the largest contributors to  $^{13}\text{C}$  spin-lattice relaxation for protonated sites, while chemical shift anisotropy (CSA) contributes substantially to the relaxation mechanism in quaternary aromatic carbon sites. For  $^{13}\text{C}$   $T_1$  studies to provide information on molecular motion, contributions from dipolar and CSA interactions must be separated.

## Objective

The goal of this chapter is to determine the molecular mobility of select carbon sites within 33DDS/DGEBA and 44DDS/DGEBA matrices using  $^{13}\text{C}$  variable temperature solid state NMR spin-lattice relaxation ( $T_1$ ) studies. By combining  $^{13}\text{C}$  spin-lattice relaxation behavior as a function of temperature with  $^2\text{H}$  NMR results, it is hoped that processes contributing to sub- $T_g$  transitions will be identified.

## Materials

All reagents were used without further purification. 33DDS and 44DDS were purchased from Aldrich. DGEBA resin, EPON 825, was donated by Hexion. 33DDS and 44DDS were solubilized in DGEBA at  $110^\circ\text{C}$ , and the resins were cured at  $125^\circ\text{C}$  for 5hrs and  $225^\circ\text{C}$  for 2hr.

Figure 38 shows the chemical structures for 33DDS, 44DDS, and DGEBA.

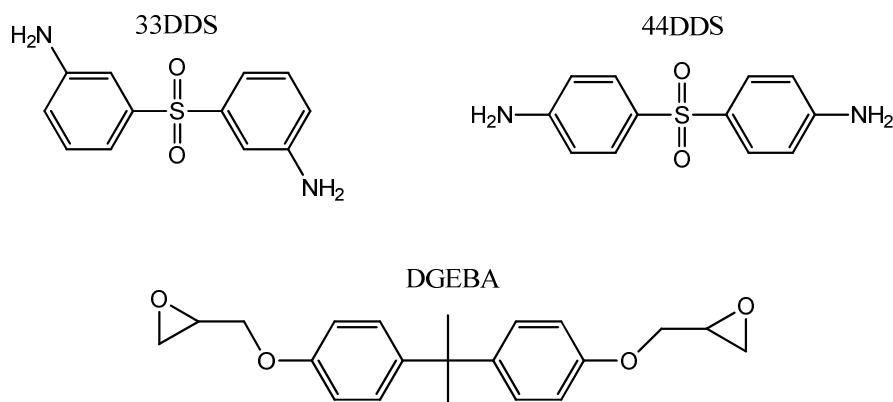


**Figure 38.** Structures of 44DDS, 33DDS, and DGEBA

## Methods

### *Carbon-13 NMR Spectroscopy*

Solid-state NMR spectroscopy was performed on a Varian <sup>UNITY</sup>INOVA 400 spectrometer using a standard Chemagnetics 7.5mm PENCIL<sup>TM</sup>-style probe. Samples were loaded into zirconia rotor sleeves, sealed with Teflon<sup>TM</sup> caps, and spun at rate of 4.0kHz. Carbon spectra were obtained using the standard cross-polarization/magic angle spinning (CP/MAS) technique with high-power proton decoupling implemented during data acquisition.<sup>94</sup> In addition, the TOSS technique was implemented to remove spinning side bands.<sup>95</sup> Acquisition parameters were as follows: The <sup>1</sup>H 90° pulse width was 5.5μs, the cross-polarization contact time was 1ms, the dead time delay was 6.4μs, and the acquisition time was 45ms. A recycle delay of 3.0s between scans was utilized. Spectral processing included Gaussian line broadening as well as fitting the baselines to a 20<sup>th</sup> order polynomial to remove spectral distortion

Spin-lattice relaxation (T<sub>1</sub>) inversion recovery experiments were performed by applying a <sup>13</sup>C 90° pulse immediately after cross polarization, thereby “flipping” the <sup>13</sup>C spins along the -z axis. After a variable delay, another 90° pulse is used to acquire signal, and thus monitor magnetization recovery. Spin-lattice values are calculated by fitting peak values using the Varian VNMR6.1C software.

### *Spectral Assignments*

<sup>13</sup>C CP/MAS solid state spectra were obtained for both the 44DDS/DGEBA and 33DDS/DGEBA samples (Figure 39). In addition to literature assignments, small molecule solution NMR studies, pre-gel melt state NMR studies, and the MNOVA® Modgraph NMRPredict package were used to make spectral assignments.<sup>96</sup>

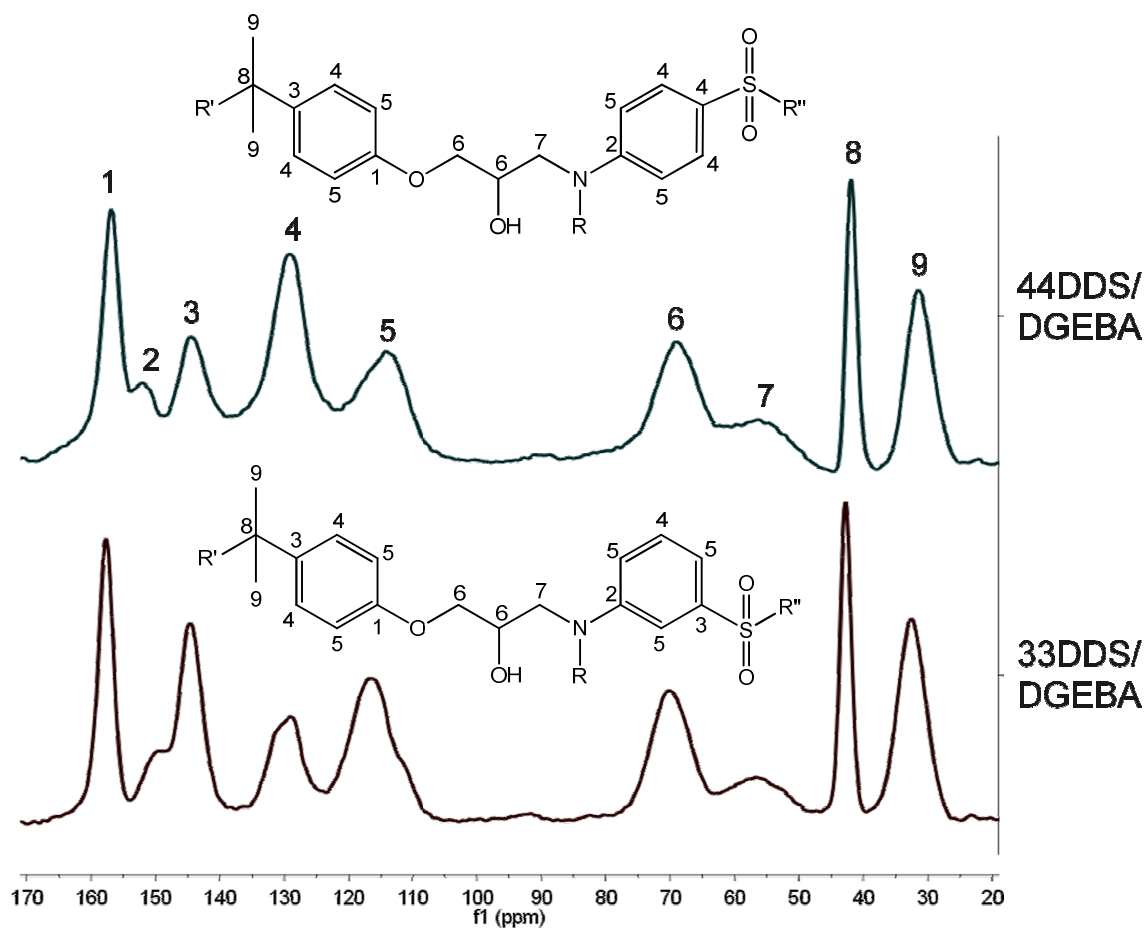


**Figure 39.** Carbon solid state CP/MAS NMR spectra of 44DDS/DGEBA and 33DDS/DGEBA with spectral assignments correlating to the carbon sites labeled.

The upfield shifts, peaks 6-9, are due to aliphatic carbon resonances. Here the shapes and chemical shifts of these peaks are similar for 33DDS and 44DDS systems, since these sites are well removed from the aromatic moieties. The downfield shifts, peaks 1-4, reflect aromatic carbon resonances. The peaks for DGEBA aromatic carbons are the same in both samples. However, the amine sites, peaks 2-5, are all noticeably different in shape and size due to the differences in meta vs. para connectivity. For instance, peak 2 appears as a shoulder on the upfield side of peak 1 in the 44DDS/DGEBA sample, but is observed as a downfield shoulder of peak 3 in the 33DDS/DGEBA sample. Peak 4 intensity is greater than peak 5 in the

44DDS/DGEBA sample, while peak 5 is the more intense than peak 4 in the 33DDS/DGEBA sample. It is important to note the resonances of the DDS carbons closest to the sulfone have different shifts. In the 44DDS/DGEBA spectrum, these are three aromatic carbons on the amine ring that contribute to peak 4, while in the 33DDS/DGEBA spectrum, these sites are observed as peaks 3, 4, and 5.

### **Comparison of $T_1$ Times between 44DDS/DGEBA and 33DDS/DGEBA**

A representative inversion-recovery experiment for 33DDS-DGEBA is shown in Figure 40. Spectra have been selected so that the null points for many of these peaks can be examined. At a delay of 0.01s, all peaks are inverted. Peak 9 exhibits its null at about 0.08s, peak 8 at 4s, etc.

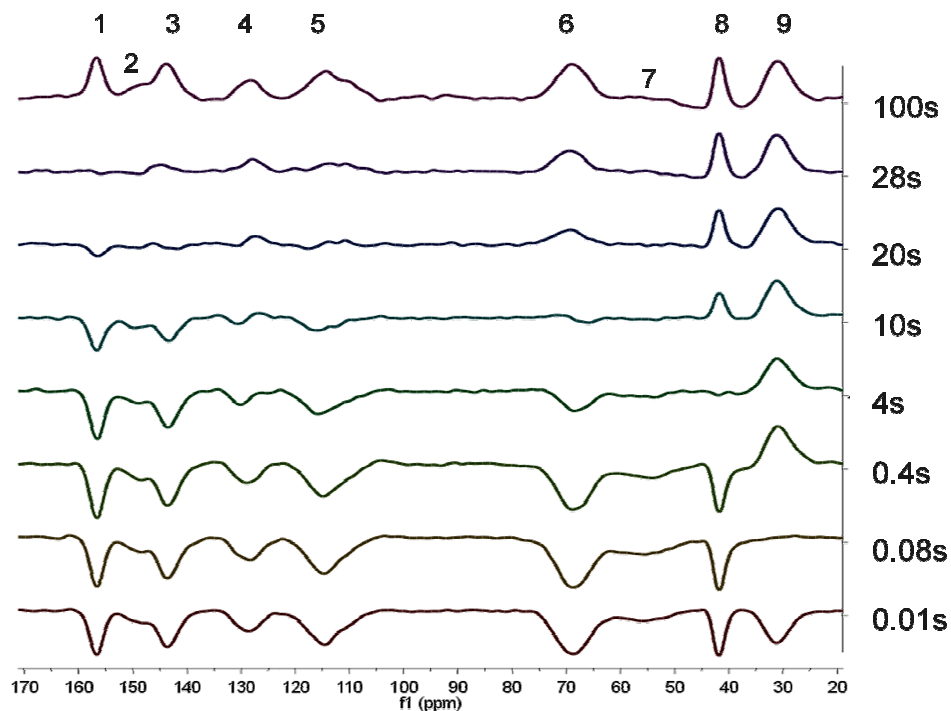


**Figure 40.** Carbon  $T_1$  inversion recovery experiment on 33DDS/DGEBA

Figure 41 is a plot of peak intensity versus delay time for the data presented in Figure 6.3. A one component curve fitting analysis was used to determine  $T_1$  values. Note that peaks 3-6 are composite resonances of two or more different carbon sites, and that differing carbon sites in 44DDS/DGEBA and 33DDS/DGEBA contribute to peaks 3-5. Using a one component curve fit is valid only if all carbon sites responsible for the peak possess the same motional behavior. The odd behavior of peak 9 (the methyl resonance) is due to a transient NOE phenomenon often associated with methyl groups.

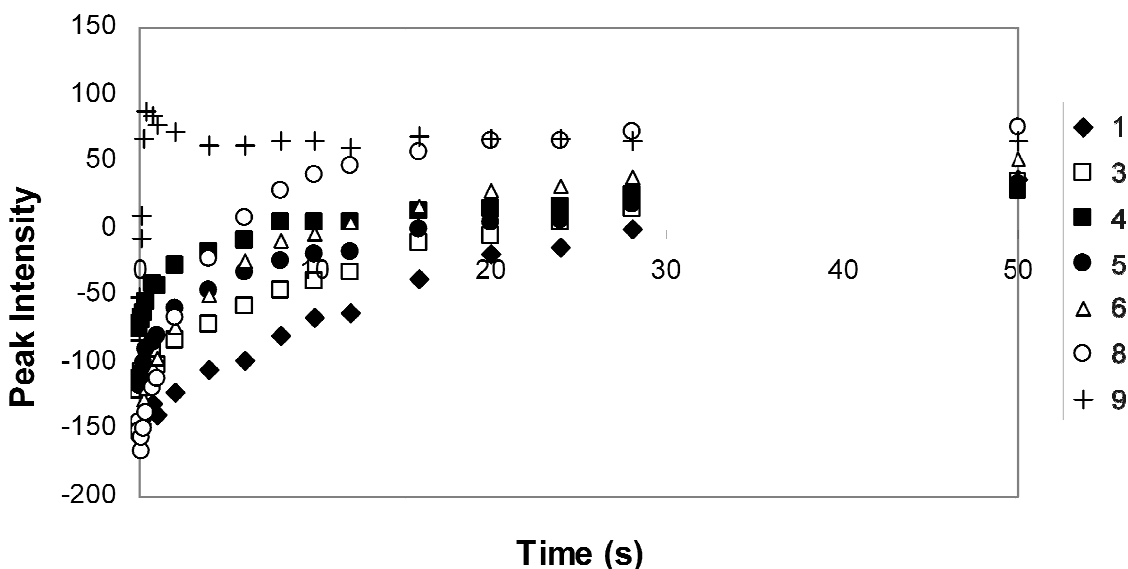


**Figure 41.** Inversion-recovery data for the spectra shown in Figure 40

The tabulated data for variable temperature  $T_1$  analysis of 33DDS/DGEBA and 44DDS/DGEBA is summarized in Table 15. The intensities of peaks 2 and 7 were not adequate for accurate fitting. Peaks 1 and 3, the quaternary aromatic sites in DGEBA and the quaternary aromatic site adjacent to the sulfone in 33DDS, possess long  $T_1$  times even at 200°C, 20°C above the  $T_g$  of 33DDS/DGEBA. Peaks 8 and 9 show increasing  $T_1$  values as temperature is increased

due to the very fast rotation of the methyl group (peak 9), which makes its spin-lattice behavior liquid-like.

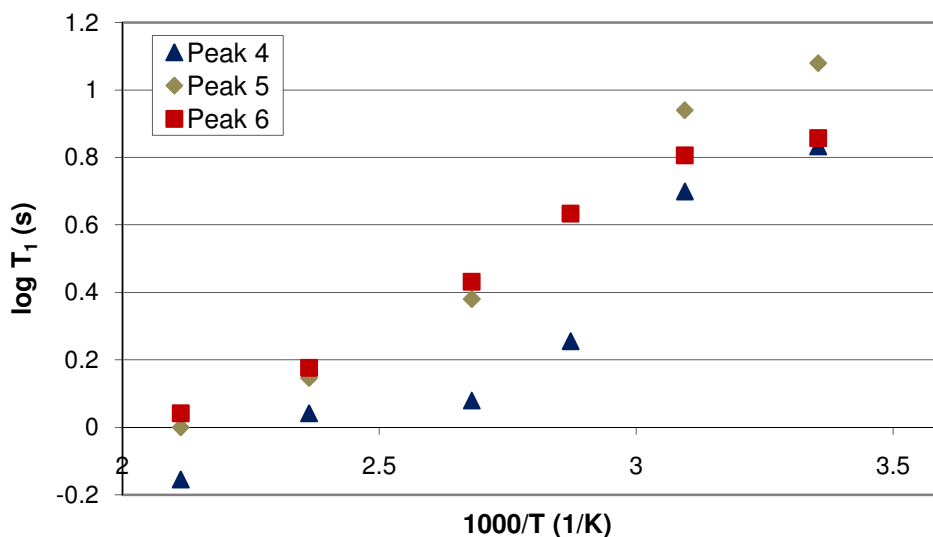
**Table 15.** Comparison of  $^{13}\text{C}$   $T_1$  Times for 33DDS/DGEBA and 44DDS/DGEBA

Spin-Lattice Relaxation Times for 33DDS/DGEBA							
T (°C)	Peak 1	Peak 3	Peak 4	Peak 5	Peak 6	Peak 8	Peak 9
25	25	19	6.8	12	7.2	4.4	0.076
50	16	12	1.6	5.9	4.3	4.4	0.071
75	19	18	1.8	4.3	4.3	4.7	0.073
100	18	15	1.2	2.4	2.7	5.3	0.084
150	18	19	1.1	1.4	1.5	7.1	0.099
200	16	14	0.70	1.0	1.1	5.5	0.090

Spin-Lattice Relaxation Times for 44DDS/DGEBA							
T (°C)	Peak 1	Peak 3	Peak 4	Peak 5	Peak 6	Peak 8	Peak 9
25	22	14	13.0	7	5.9	3.9	0.072
50	18	13	11.0	5.4	5.3	4.0	0.071
75	18	12	8.6	4.6	4.9	4.6	0.076
100	18	14	7.3	3.2	3.5	4.7	0.077
150	15	13	5.5	1.7	2.3	4.8	0.086
200	15	11	1.70	1.1	1.7	5.8	0.098

Figures 42 and 43 display the  $\log T_1$  time vs.  $1/T$  plots for peaks 4, 5, and 6 of 33DDS/DGEBA and 44DDS/DGEBA, respectively. Peaks 1, 3, 8, and 9 were excluded from the plots. For carbon sites 1 and 3, due to the location on the axis of symmetry, only small changes in  $T_1$  time were observed across the temperature range. Peaks 8 and 9 were excluded due to the transient NOE phenomenon associated with methyl groups. Peaks 4 and 5 comprise the  $sp^2$ -hybridized phenylene ring carbons. Peak 6 is composed of two of the aliphatic carbons formed by the ring opening of the epoxide group.



**Figure 42.** Log  $T_1$  time vs.  $1/T$  plot for peaks 4,5, and 6 of 33DDS/DGEBA.

The behavior of peaks 4, 5, and 6 is approximately linear from 25 to 200°C in 33DDS/DGEBA, indicating a single mode of motion, i.e., Arrhenius behavior. The nonlinearity of peak 4 at 75°C and 100°C is not understood at this time. This anomaly may be due to experimental error.

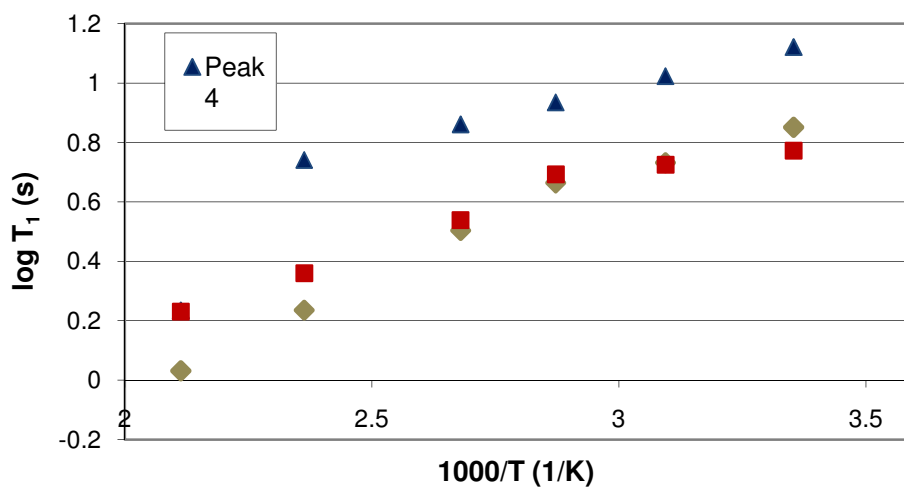


**Figure 43.** Log  $T_1$  time vs.  $1/T$  plot for peaks 4,5, and 6 of 44DDS/DGEBA.

In the 44DDS/DGEBA sample, linearity of the data points indicates the motions follow Arrhenius behavior. Additionally, peak 4 shows a sharp drop in slope at 150°C, around the same temperature as a slope change in the deuterium log  $T_1$  time vs.  $1/T$  plot for the epoxy phenyl rings in that sample is observed. Peak 5 shows the change in  $T_1$  at a lower temperature because the carbons contributing are close to amine and ether linkages, which provide a greater deal of ring flexibility than the sulfone.

Carbon CP/MAS  $T_1$  experiments were largely inconclusive due to broad peaks, resonances shifting in the 33DDS vs. 44DDS samples, and multiple modes of relaxation which contribute to  $T_1$  behavior, including dipolar effects and chemical shift anisotropy. However, some interesting information could still be gleaned. Quaternary aromatic sites, peaks 1 and 3, exhibited small changes in  $T_1$  values with increasing temperature due to their location on the axis of symmetry. At this location, even when phenyl rings are moving, these atoms are remaining in the same place. Peaks 4, 5, and 6 display generally Arrhenius behavior in the log  $T_1$  time vs.  $1/T$  plots. Peak 4 in 44DDS/DGEBA shows a discontinuity in Arrhenius behavior at 150°C, approximately the same temperature this same phenomenon is seen in the  $^2\text{H}$  NMR log  $T_1$  time vs.  $1/T$  plot. The proximity of aromatic carbons to the sulfone group appears to increase spin-lattice relaxation times of the carbon sites. This evidence supports the hypothesis proposed in Chapter IV that the sulfone limits phenyl ring mobility. Future work should include multi-component fitting to separate carbon sites resonating in the same peaks and to determine if multiple modes of relaxation can be observed.

## RESULTS PART VI

### REACTION KINETICS OF PRE-GEL CROSSLINKED EPOXIES BY SOLID STATE NMR SPECTROSCOPY

#### Objective

In this section, variable temperature in situ NMR spectroscopy (VT-NMR) is used to study the kinetics of network formation of two amine/epoxy matrices. The kinetics of the meta amine curative 3,3'-diaminodiphenyl sulfone (33DDS) and epoxy diglycidyl ether of bisphenol A (DGEBA) are probed with  $^{13}\text{C}$  VT-NMR spectroscopy. DGEBA is also reacted with a  $^{15}\text{N}$ -labeled para amine 4,4'-diaminodiphenyl sulfone (44DDS), and  $^{15}\text{N}$  VT-NMR is used to track the kinetics of cure. The monomers used are shown in Figure 44.

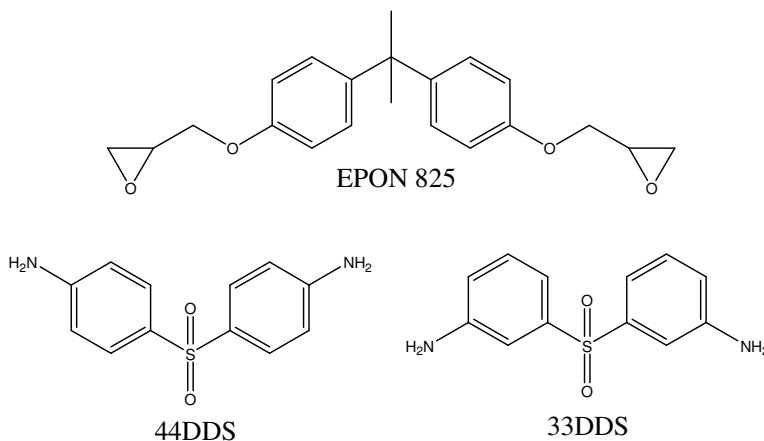


**Figure 44.** DGEBA, 44DDS, and 33DDS

## **Materials**

Anhydrous sodium hydroxide pellets (NaOH,  $\geq 98\%$  purity), toluene ( $\geq 99\%$  purity), acetic anhydride ( $\geq 98\%$  purity), carbon disulfide ( $\geq 99\%$  purity), sulfonyl chloride ( $\geq 98\%$  purity), aluminum trichloride ( $\geq 98\%$  purity), glacial acetic acid, ammonium chloride ( $\geq 99\%$  purity), tetrahydrofuran (THF,  $\geq 99\%$  purity), hydrogen peroxide ( $\geq 98\%$  purity), hydrochloric acid (HCl,  $\geq 98\%$  purity), and decolorizing carbon, methanol ( $\geq 99\%$  purity) were purchased from Sigma Aldrich and used as received. The NaOH pellets were dissolved into deionized water to make a 40%wt. aqueous NaOH solution.  $^{15}\text{N}$ -labeled aniline, 98% purity was obtained from Cambridge Isotope Laboratories, Inc. and used as received.

## **Methods**

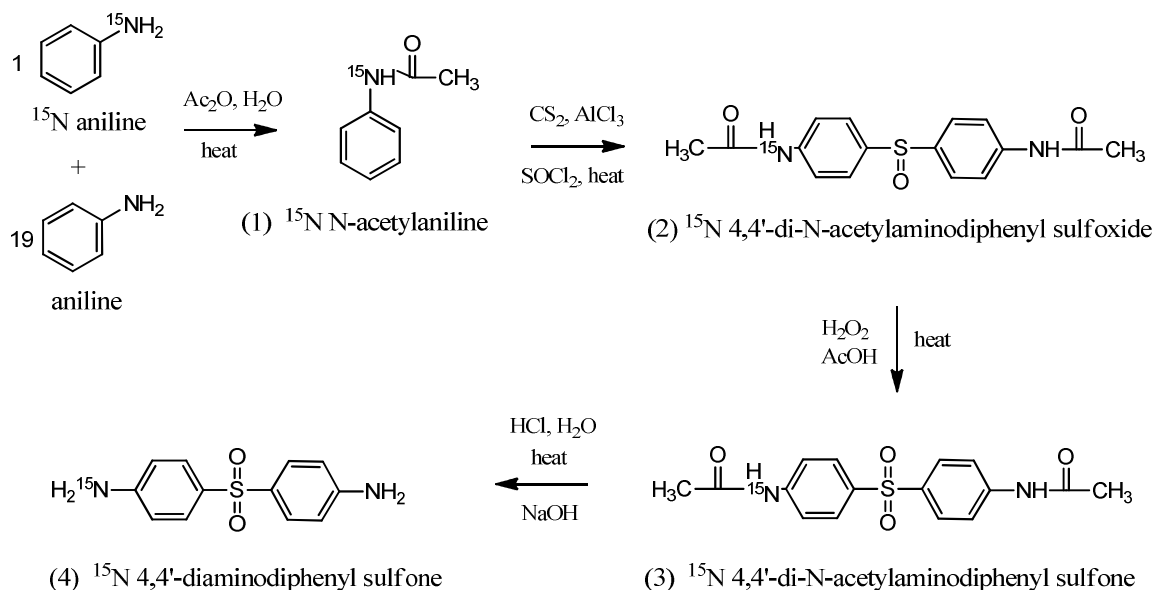
NMR studies for the solid-state require benchmark control (non-labeled) studies to optimize the spectrometer for each resin system. As necessary, isotope-labeled networks are synthesized as model compounds to fully resolve resonance shifting patterns for a specific matrix and NMR technique. For the  $^{13}\text{C}$  study, 33DDS was chosen due to its greater solubility in DGEBA. For the  $^{15}\text{N}$  study,  $^{15}\text{N}$ -labeled 44DDS was chosen due to its ease of synthesis in comparison to 33DDS. The detailed synthetic procedure for creating  $^{15}\text{N}$  labeled 44DDS is included below. The  $^{13}\text{C}$  VT-NMR study accomplished on 33DDS/DGEBA did not require isotope-labeled synthesis as signal-to-noise was acceptable.

### **Synthesis of $^{15}\text{N}$ Labeled 4,4'-Diaminodiphenyl Sulfone (44DDS)**

The natural abundance of  $^{15}\text{N}$  is 0.4%, making facile NMR studies difficult. In order to obtain higher signal-to-noise (S/N)  $^{15}\text{N}$  NMR spectra, labeling samples with  $^{15}\text{N}$  is often required. In

this work, 44DDS/DGEBA samples were cured with  $^{15}\text{N}$ -labeled 44DDS incorporated into the matrix at a level of ~5% enrichment.

### Scheme 5. Synthesis of $^{15}\text{N}$ 44DDS



#### *N*-acetylaniline

Aniline (6g  $^{15}\text{N}$ -labeled + 54g unlabeled) was added to 150ml acetic anhydride and heated at reflux for 30min. After cooling to room temperature, 180ml water was added and heated at reflux for 10min. The solution was then cooled to room temperature and diluted with water to precipitate the product, *N*-acetylaniline. The *N*-acetylaniline was filtered, washed with water, recrystallized from water, and dried to yield 45 g; mp: 109-111°C (NMR Figure 45).

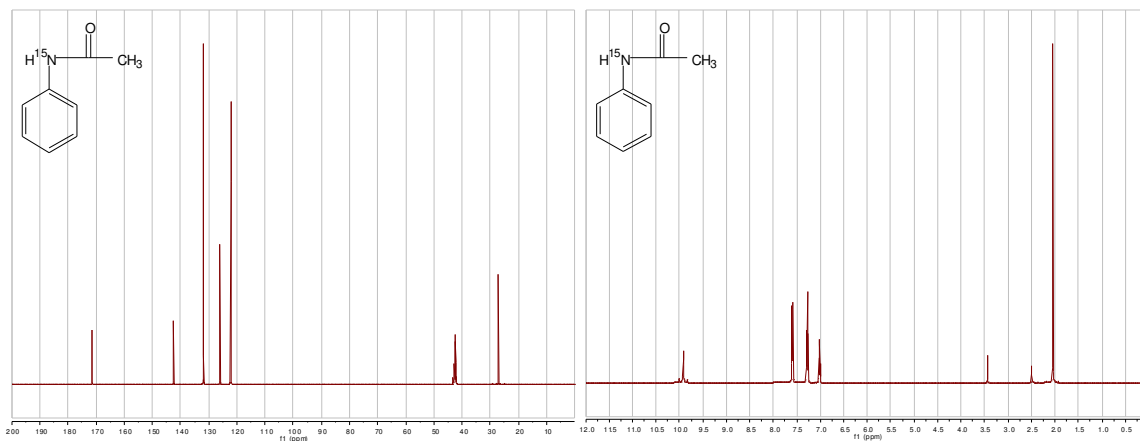


**Figure 45.**  $^1\text{H}$  and  $^{13}\text{C}$  NMR spectra of  $^{15}\text{N}$ -labeled N-acetylaniline.

#### **4,4'-Di-N-acetylamino-diphenyl Sulfoxide**

43g N-acetylaniline was suspended in 437ml  $\text{CS}_2$ , after which 80g  $\text{AlCl}_3$  and 17.5ml  $\text{SOCl}_2$  were added. After the initial reaction subsided, the mixture was heated at reflux for 6hr, cooled to room temperature, and quenched by the addition of a 10% ammonium chloride solution in water. The mixture was filtered, and the filter cake was washed with water. The filter cake was then dissolved in THF, filtered, and the filtrate concentrated under vacuum to yield 42g of product. The product, 4,4'-di-n-acetylamino-diphenyl sulfoxide, was recrystallized with  $\text{MeOH}/\text{H}_2\text{O}$ ; mp:  $304^\circ\text{C}$  (NMR Figure 46).

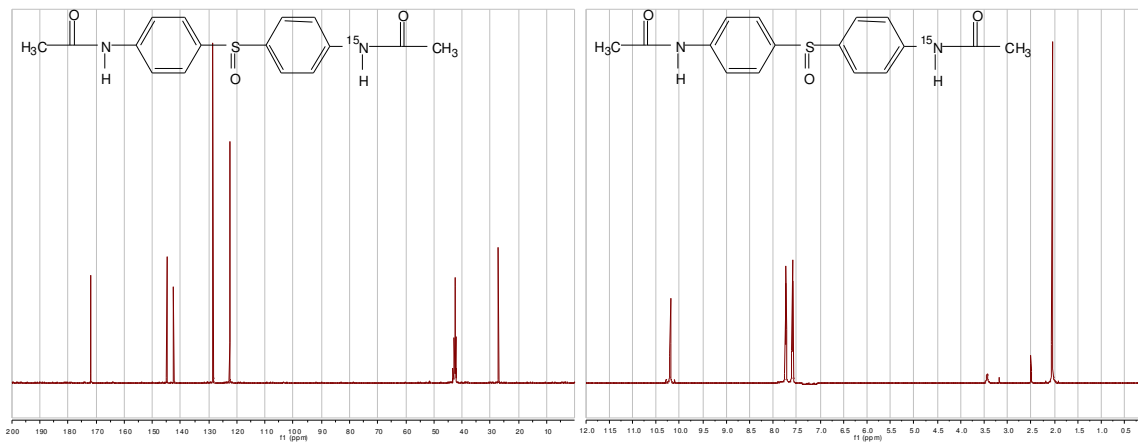


**Figure 46.**  $^1\text{H}$  and  $^{13}\text{C}$  NMR of  $^{15}\text{N}$  4,4'-di-n-acetylaminodiphenyl sulfoxide.

#### 4,4'-Di-N-acetylaminodiphenyl Sulfone

41g 4,4'-di-N-acetylaminodiphenyl sulfoxide was suspended in 525ml glacial acetic acid. 52.5ml 30%  $\text{H}_2\text{O}_2$  was added to the suspension, and the mixture was allowed to stand for 3hr at room temperature. The mixture was then heated at  $50^\circ\text{C}$  for 2hr and subsequently refluxed until homogenous. The homogenous mixture was cooled to room temperature, 31.5ml 30% $\text{H}_2\text{O}_2$  was added, and the mixture was stored overnight at  $4^\circ\text{C}$ . The mixture was concentrated under vacuum to yield 38g and then recrystallized with  $\text{MeOH}/\text{H}_2\text{O}$  to yield 37g 4,4'-di-n-acetylaminodiphenyl sulfone; mp:  $281^\circ\text{C}$  (NMR Figure 47).

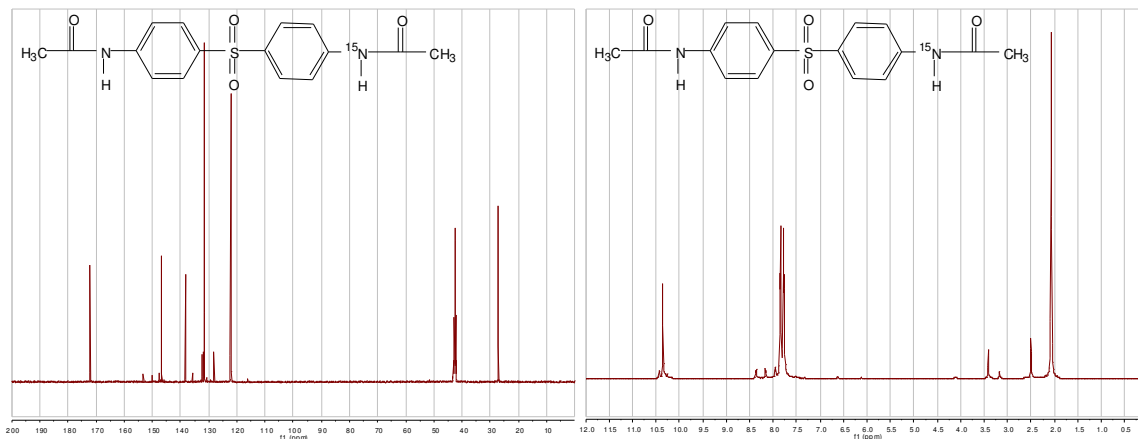


**Figure 47.**  $^1\text{H}$  and  $^{13}\text{C}$  NMR of  $^{15}\text{N}$  4,4'-di-n-acetylaminodiphenyl sulfone.

#### **4,4'-Diaminodiphenyl Sulfone**

36g 4,4'-di-n-acetylaminodiphenyl sulfone was suspended in 360ml 10% HCl, and heated at reflux for 1.5hr. At this point decolorizing carbon was added, and the mixture was refluxed for 1hr, filtered while hot, and cooled to room temperature. 10% NaOH was added to adjust the pH to 14, and the resulting precipitate was isolated by filtration, recrystallized with MeOH/H<sub>2</sub>O, and dried in a vacuum oven to yield 15g of the final product,  $^{15}\text{N}$  labeled 44DDS; mp: 178°C (NMR Figure 48).

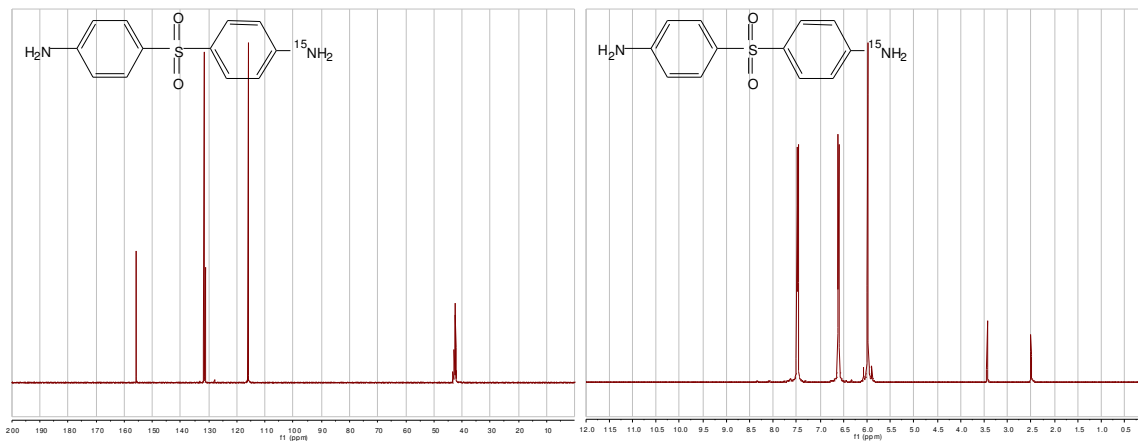


**Figure 48.**  $^1\text{H}$  and  $^{13}\text{C}$  NMR of  $^{15}\text{N}$  4,4'-diaminodiphenyl sulfone.

## NMR Analysis

Solid-state NMR spectroscopy was performed on a Varian <sup>UNITY</sup> INOVA 400 spectrometer using a standard Chemagnetics 7.5 mm PENCIL™-style probe. Samples were loaded into zirconia rotor sleeves and sealed with Teflon™ caps. The standard solid state magic angle spinning (MAS) technique was used with high-power proton decoupling implemented during data acquisition.<sup>97</sup> In addition, the TOSS technique was implemented on the  $^{13}\text{C}$  data acquisition to remove spinning side bands.<sup>98</sup>

For liquid conditions, a modified Bloch decay sequence was used. Here instead of a simple  $90^\circ$  pulse acquisition, a DEPTH sequence was implemented in order to reduce background  $^{13}\text{C}$  signal. For vitrified samples, a standard cross-polarization / magic angle spinning (CP/MAS) sequence was used, with a cross polarization pulse of 1ms. High-power proton decoupling during acquisition was employed in both sequences.

## **Sample Preparation**

33DDS and 44DDS are crystalline solids with melting temperatures of 170-173°C and 175-177°C, respectively. DGEBA is a viscous liquid in which both 33DDS and 44DDS are marginally soluble. VT-NMR samples are prepared by sonicating the amine and the epoxy together for 20 minutes at 50°C. This amount of heat does not initiate reaction but does solubilize some amine into the epoxy. The sample is then placed in a solid state NMR rotor and data acquisition using Bloch decay is started. Samples are prepared stoichiometrically assuming full reaction of the amine and epoxy. Since each amine can react twice, once to form a secondary amine and a second time to form a tertiary amine, samples are prepared at a 2:1 epoxy:amine molar ratio (corresponding to a 1:1 ratio of reactive groups).

## **Variable Temperature NMR (VT-NMR)**

Variable temperature experiments were performed by obtaining a room temperature spectrum for the unreacted specimen, then heating to 125°C and obtaining spectra via Bloch decay until the signal broadened and resolution was lost. At this point, cross polarization was employed. After this, the samples were heated up to 200°C and spectra were obtained using cross polarization. Samples were then cooled to 25°C to obtain a final CP spectrum. For <sup>13</sup>C data, previously reported spectral assignments, in addition to small molecule solution NMR studies and the MNOVA® Modgraph NMRPredict package were used to make validated spectral assignments.<sup>99</sup>

### **Carbon Acquisition Parameters**

The  $^1\text{H}$   $90^\circ$  pulse width was  $5.25\ \mu\text{s}$ , the cross-polarization contact time was 1 ms, the dead time delay was  $6.4\ \mu\text{s}$ , and the acquisition time was 45 ms. A recycle delay of 3 seconds between scans was utilized.

### **Nitrogen Acquisition Parameters**

The  $^1\text{H}$   $90^\circ$  pulse width was  $6.5\ \mu\text{s}$ , the cross-polarization time was 2 ms, the dead time delay was  $6.4\ \mu\text{s}$ , and the acquisition time was 45 ms. The recycle delay was 3 or 5 seconds, and a  $^1\text{H}$  decoupling field of 61.9 kHz was implemented during data acquisition.

### **Carbon VT-NMR Analysis of 33DDS/DGEBA**

The  $^{13}\text{C}$  VT-NMR Bloch decay spectra of the 33DDS/DGEBA system consists of narrow line widths, with new resonances appearing upon heating to  $125^\circ\text{C}$ . These can be integrated which can be integrated in order to identify the kinetics of the cure (Figure 49).

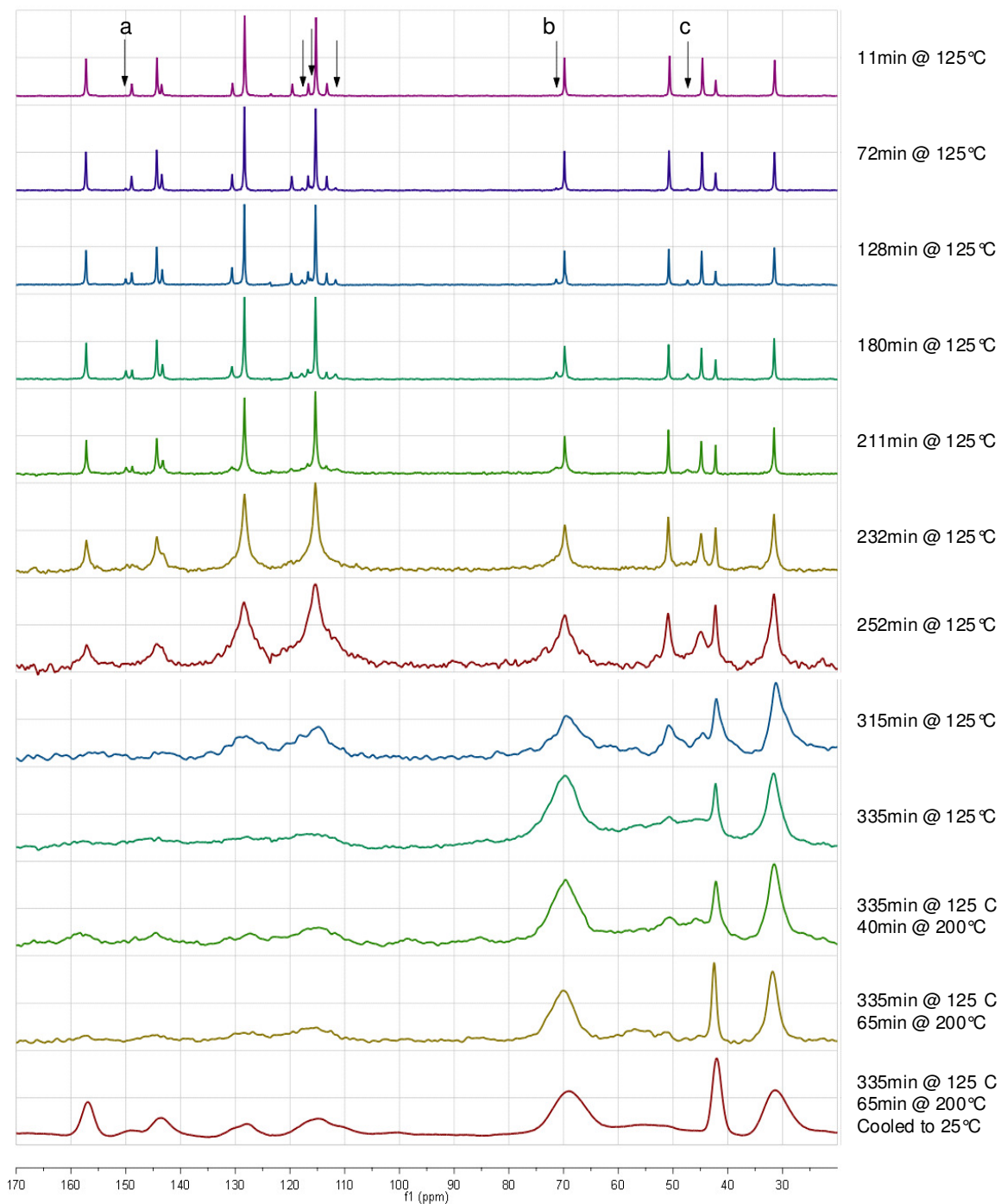


**Figure 49.** Variable temperature  $^{13}\text{C}$  NMR spectra of 33DDS/DGEBA cure

The resonances of interest are labeled (a), (b), and (c) at 150, 71.5, and 47.5ppm, respectively (Figure 49). Site (a) exhibits a new peak for the aromatic carbon on 33DDS



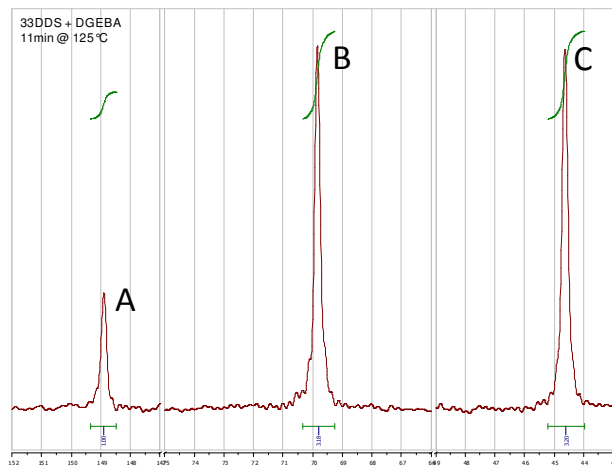


**Figure 51.** 33DDS and DGEBA after 11min at 125°C; no observable reaction

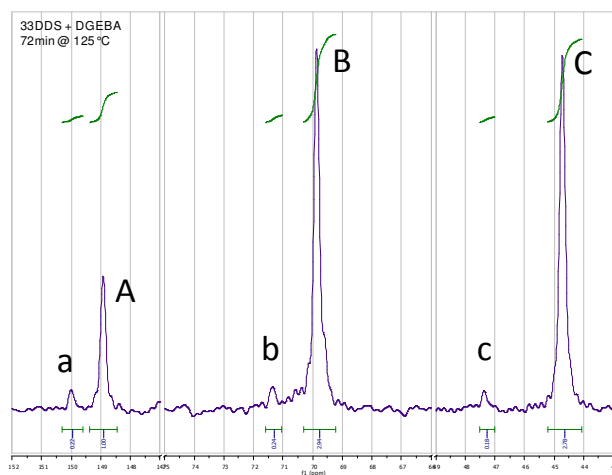


**Figure 52.** 33DDS and DGEBA after 72min at 125°C.

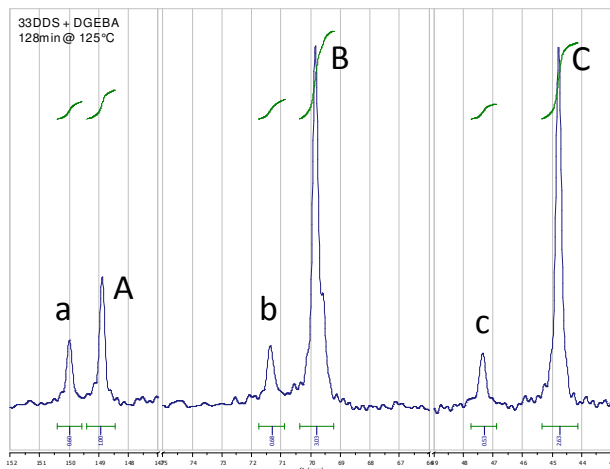


**Figure 53.** 33DDDS and DGEBA after 128min at 125°C.

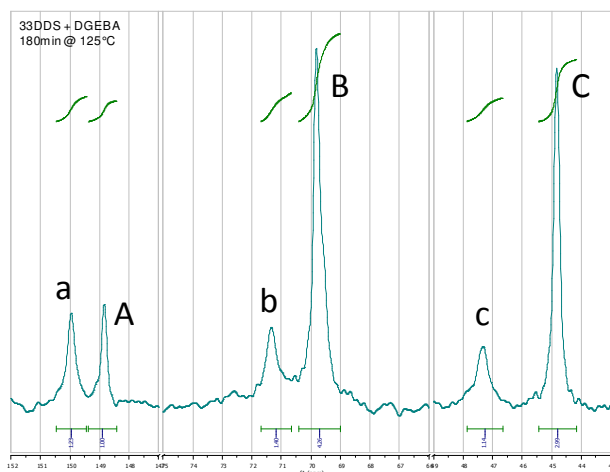


**Figure 54.** 33DDDS and DGEBA after 180min at 125°C.

The peaks corresponding to the reacted species, (a), (b), and (c), can be compared to those corresponding to the unreacted species, (A), (B), and (C) to determine percent conversion of epoxide and amine (Table 16).

**Table 16.** Reaction of 33DDS and DGEBA as Shown by NMR

Time at 125°C (min)	Conversion (A→a)	Conversion (B→b)	Conversion (C→c)
11	0%	0%	0%
72	18%	8%	6%
128	37%	18%	17%
180	55%	25%	27%

Table 16 summarizes the conversion by showing four snapshots along the cure pathway; however, between 0min and 180min after reaching 125°C, 11 spectra were taken and integrated. The complete data is shown in a conversion versus time plot in Figure 55.

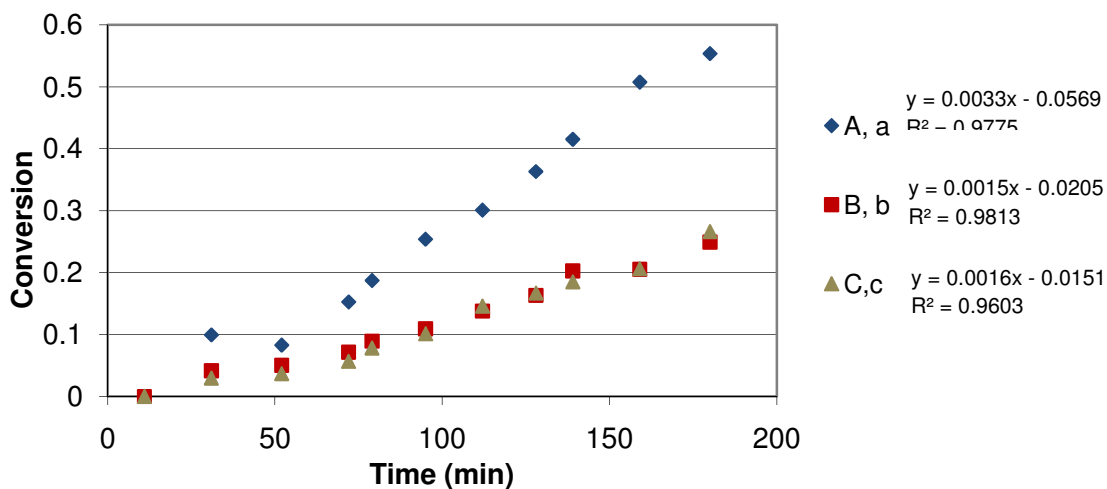


**Figure 55.** <sup>13</sup>C VT-NMR results of 33DDS/DGEBA conversion vs. time plot.

Figure 55 shows all three conversions plotted linearly versus time. The plot for the amine carbon possesses a slope approximately twice that of the two epoxide carbon sites. Therefore, approximately twice as much amine as epoxide is being consumed during the reaction. The stoichiometry in the reaction is set at two epoxides for every amine so that at 100% conversion all epoxide rings have reacted once and all amines have reacted twice to form secondary amines. Making the assumptions that epoxides are only consumed by amines and primary amines only react with epoxides, the data shows that virtually no tertiary amines are being formed while the matrix has sufficient mobility to be effectively probed by Bloch decay techniques. This explains why only two amine peaks are observed.

Oddly, the reaction rates are slower than expected based on near IR measurements.<sup>100</sup> This is likely because of difficulties in fully solubilizing the 33DDS deu to the centrifugal force of sample spinning. To address this issue, the amine was further solubilized before acquiring spectra in later experimentation. However, the window of opportunity before peaks broaden is narrow, and further solubilization results in further reaction, and no useful kinetic data could be obtained.

### **<sup>15</sup>N NMR Analysis of 44DDS/DGEBA**

A sample incorporating 5% <sup>15</sup>N-labeled material was used for <sup>15</sup>N NMR VT analysis of 44DDS/DGEBA. The top two spectra in Figure 56 show the solution <sup>15</sup>N NMR of unlabeled 44DDS (red) and 5% labeled <sup>15</sup>N 44DDS (green), illustrating the significant S/N increase obtained via isotopic labeling.

An amine peak in addition to the primary amine was observed at 256min at 125°C, obtained using the CP/MAS method (Figure 56). Although the spectrum possesses poor S/N two peaks are nevertheless clearly observed. Spectra taken after 256min only showed one broad peak. It is likely that the peak forming at 256min is the secondary amine appearing, while the broad peak observed after 1hr at 200°C is due to the formation of tertiary amine. This is consistent with the  $^{13}\text{C}$  data, which indicates that secondary amines do not form until after all primary amines have been consumed. At this point, peaks are too broad to resolve secondary/tertiary amine sites.

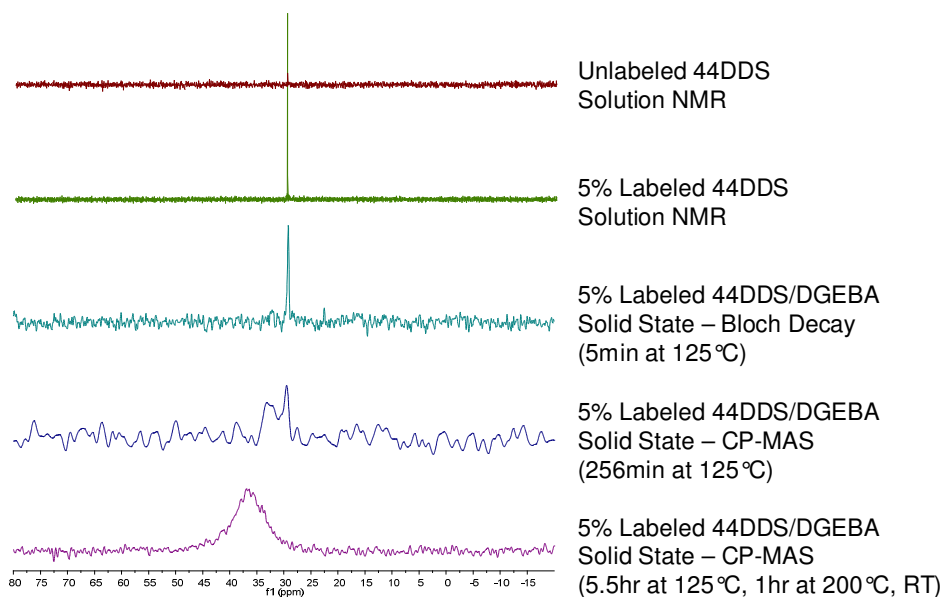


**Figure 56.** Variable temperature  $^{15}\text{N}$  NMR study of 33DDS/DGEBA cure

Unfortunately, this work suffered the same problem with amine solubility during magic angle spinning as in the  $^{13}\text{C}$  work, and further solubilization once again resulted in the inability to acquire kinetic data. Additionally, these experiments, 5%  $^{15}\text{N}$  labeling was not sufficient to

see the appearance of an integratable secondary or tertiary amine peak appear using the Bloch decay sequence.

Solid state magic angle spinning NMR spectroscopy does not provide a facile and accurate method for determining reaction kinetics of 33DSS/DGEBA or 44DDS/DGEBA. Spectral distances between resonances of unreacted and reacted species are not sufficient to be individually integrated after the sample begins to gel and peaks broaden. Additionally, the magic angle spinning technique appears to centrifuge the amine out of the epoxy, thus artificially slowing reaction kinetics.

## **RESULTS PART VI**

### **CHAIN DYNAMICS OF EPOXY-BASED COMPOSITES AS INVESTIGATED BY BROADBAND DIELECTRIC SPECTROSCOPY**

#### **Introduction**

Polymer networks based DGEBA cured by the simple aromatic amines 33DDS and 44DDS were considered good model systems for studying epoxy networks since investigation of the chemistry of reactions and side reactions had been carefully established, structural models of networks in the rubbery state were produced, and polymers showed a high level of mechanical properties in the glassy state. These properties facilitate understanding important aspects of structural-properties relationship of the polymers when compared to more complex epoxy systems.<sup>101</sup>

Generally, many aspects of glassy network cannot be understood without considering the chemistry of their formation, degree of crosslinking and behavior in the rubbery state. Crosslink density has a significant effect on behaviors of a network. In general, a higher density of crosslinks, which means a “tighter” network, results in a higher modulus of a material.<sup>102</sup> The crosslink density of a network is dependent upon the molecular weight between crosslinks and the extent of reaction as a higher conversion results in higher crosslink density. Full conversion of functional groups in an epoxy network is usually unattainable due to network vitrification, and the final structure is a combination of a majority of tertiary amines and a small amount of secondary amines. Meanwhile, the molecular weight of the monomers determines the molecular weight between crosslinks. At a theoretically full conversion, the crosslink density of a network is inversely proportional to the average molecular weight of segments between junctions,  $M_c$ .

Longer segments, due to less constraint of junctions, display more mobility and flexibility, which leads to a network with a smaller modulus.<sup>103</sup>

The work here investigates the dynamics of the glass transitions ( $T_g$ ) and secondary relaxations of epoxy networks formed from the reaction of diglycidyl ether of bisphenol A (DGEBA) with the 4,4'-diaminodiphenyl sulfone (44DDS) vs. 3,3'-diaminodiphenyl sulfone (33DDS) curatives. Although secondary and  $T_g$  related motions for 44DDS/DGEBA networks were studied in details by other researchers,<sup>104,105</sup> to the best of our knowledge, no reports mention the use of 33DDS/DGEBA networks.

Here, modern broadband dielectric spectroscopy (DES) was used to interrogate the molecular dynamics of these resin networks. Recently, Mauritz et al. used DES to characterize chemical degradation in polylactides<sup>106</sup> and Nafion ionomers<sup>107</sup> as well as to accurately define and confirm the true glass transition temperature of Nafion membranes.<sup>108</sup>

Dielectric spectroscopy is a powerful tool because information over a broad frequency range is attainable,<sup>109</sup> so motional processes that occur over broad time and distance scales can be investigated vs. temperature. In addition to polymer relaxations, significant differences in dielectric permittivity and/or electrical conductivity across phase boundaries can cause fluctuating interfacial polarization that manifest at low frequency ( $f$ ) on loss permittivity ( $\epsilon''$ ) vs.  $f$  plots.<sup>110</sup>

Dielectric spectroscopy deals with the interaction of an applied alternating electric field with the orientable dipoles on a polymer that account for overall polarizability. Conformational fluctuations on different distance scales affect dipole reorientation and the long range chain segmental mobility that is affected at the glass transition is a cooperative process. The dielectric spectrum of an amorphous polymer generally shows multiple relaxations at different

temperatures, where each relaxation is indicated by a peak in loss permittivity  $\epsilon''$  and an associated step decrease in storage permittivity ( $\epsilon'$ ) versus frequency at a fixed temperature.

## **Objective**

The principle goal of this work is to study the dynamics of the secondary (sub- $T_g$ ) and glass transition relaxations of 33DDS/DGEBA and 44DDS/DGEBA using broadband dielectric spectroscopy (DES). To determine the polymeric chemical structures responsible for sub- $T_g$  relaxations, relationships between dielectric relaxations and molecular motions observed with deuterium NMR spectroscopy can be established. Firstly, the temperature at which a motion of a certain frequency occurs in DES can be related to a calculated temperature from deuterium NMR Arrhenius plots. Next, correlation times of the dielectric relaxations and motions observed with  $^2\text{H}$  NMR can be compared. Finally, if sub- $T_g$  dielectric relaxations are small scale motions, Arrhenius plots of the LOG correlation time versus inverse temperature can be created and activation energy can be calculated. This activation energy can be compared to activation energies determined by  $^2\text{H}$  NMR lineshape simulations. In this work, the temperatures, correlation times, and activation energies of sub- $T_g$  relaxations are determined via dielectric spectroscopy.

## **Materials**

### ***Preparation of Cured Epoxy Resins***

All reagents were used without further purification. 33DDS and 44DDS were purchased from Aldrich. EPON 825, DGEBA resin, was donated by Hexion. 33DDS and 44DDS were

solubilized in DGEBA at 110°C under vacuum, and the resins were cured at 125°C for 5hrs and 225°C for 2hrs (Figure 57).

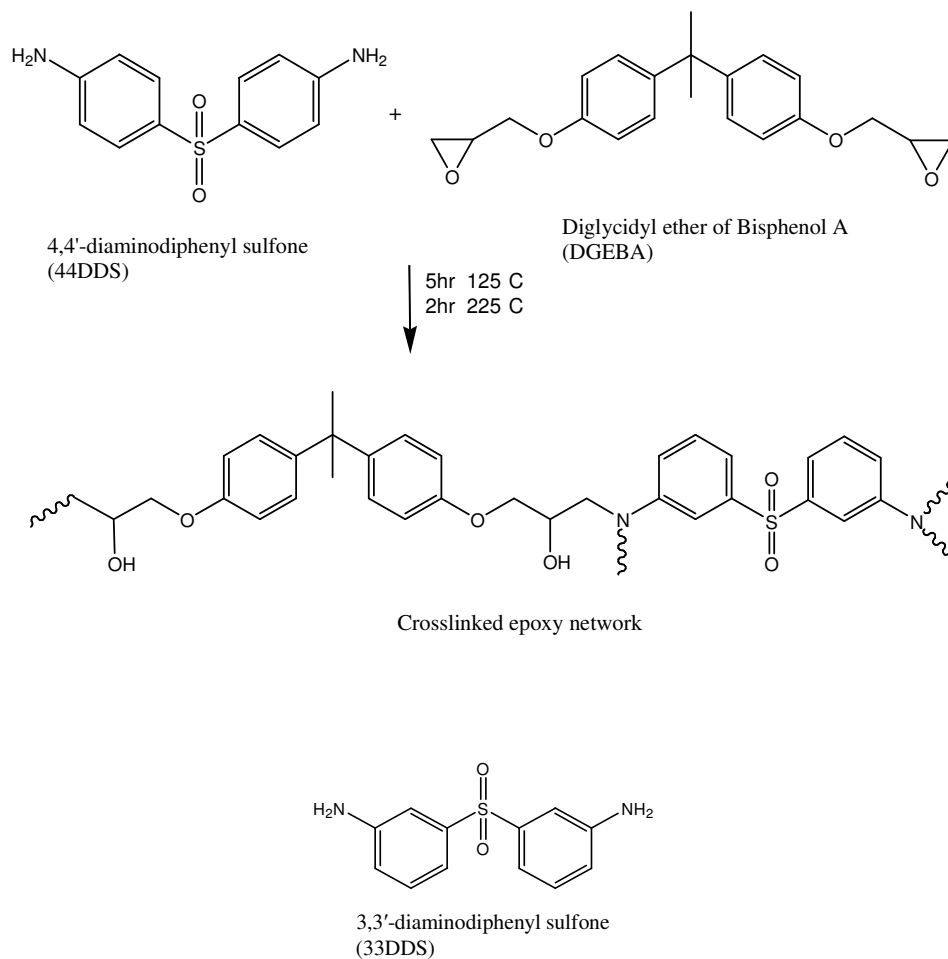


**Figure 57.** Reaction between DGEBA and 44DDS. 33DDS is reacted in the same manner

## Methods

### *Dynamic Mechanical Analysis (DMA)*

The dynamic storage modulus ( $E'$ ) and  $\tan \delta = E''/E'$  vs. temperature (T) curves for samples were generated using a DMA Thermal Analysis Q800 instrument. All samples were run

in tensile mode with a frequency of 1 Hz and oscillation amplitude of 20  $\mu\text{m}$ . The experiments were performed over the temperature range of -120 to 300°C at a heating rate of 2°C/min.

### ***Broadband Dielectric Spectroscopy (DES) Measurements***

Dielectric spectra were collected isothermally using a Novocontrol GmbH Concept 80 Broadband Dielectric Spectrometer over the frequency range 0.1 Hz - 3 MHz and temperature range of -80 - +300°C. Temperature stability was controlled to within  $\pm 0.2^\circ\text{C}$ . Resin sample was cured between two stainless steel discs with the lower one of 4 cm diameter and the upper one of 2 cm diameter. Thickness of both discs was determined before and after enclosure of the resin to determine the thickness of each sample. Those discs with samples were preconditioned in a humidity chamber with controlled 19% RH for one week before performing DES experiments. Electrodes with sample were then transferred to the instrument for data collection.

### ***Dynamic Mechanical Analysis (DMA)***

Figure 58a shows the dynamic loss tangent ( $\tan \delta$ ) vs. temperature for 33DDS/DGEBA and 44DDS/DGEBA. Molecular motions in networks are shown by three distinct peaks, with different intensities and degrees of broadening. The first transition is broad with a peak maximum at  $\approx -50^\circ\text{C}$  for both samples and will be called the  $\gamma$ -transition. The second transition is a weak one with peak maxima at  $\approx 40^\circ\text{C}$  and will be called  $\beta$ -transition. The third transition represents the glass transition temperatures ( $T_g$ ) of the networks and will be called  $\alpha$ -transition.

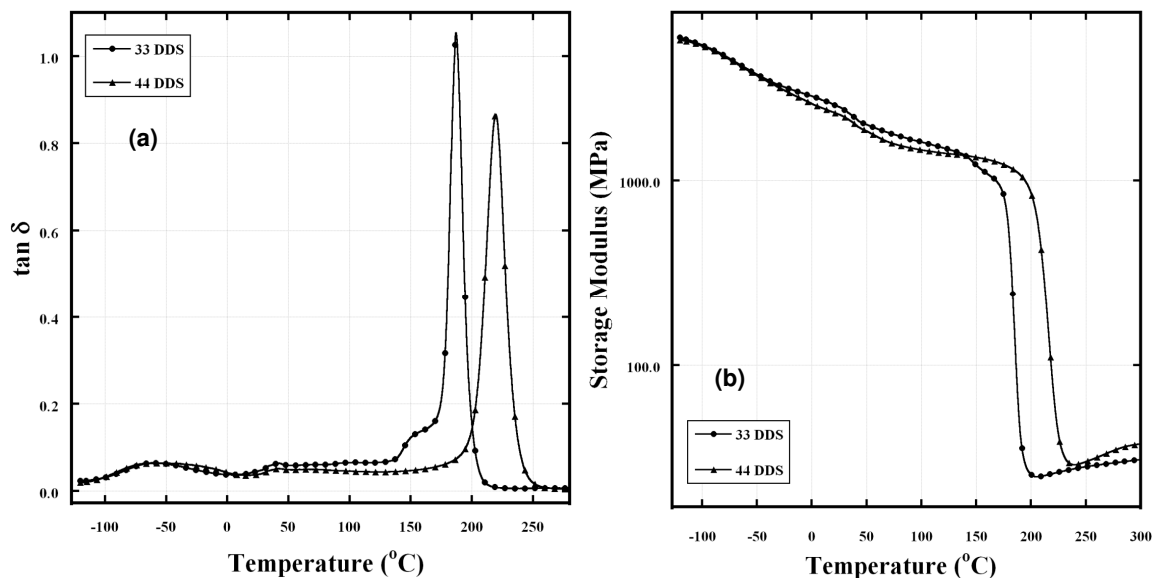


**Figure 58.** DMA curves showing  $\tan \delta$  (a) and storage modulus (b) vs. temperature at 1 Hz for 33DDS/DGEBA and 44DDS/DGEBA.

Assignments of the  $\gamma$  and  $\beta$ -transitions will be discussed in detail in the next section. The  $T_g$  peak is clearly higher for the 44DDS/DGEBA sample comparing to the 33DDS/DGEBA by about  $50^\circ\text{C}$ . Interestingly, as shown in Figure 58a, the 33DDS/DGEBA network shows a shoulder at the lower temperature part of the  $\tan \delta$  curve for the  $T_g$ . Keenan et al. reported a split in the  $\tan \delta$  vs. temperature curve for networks formed by curing tetraglycidyl 4,4'-diaminodiphenyl methane epoxy with small amounts of 4,4'-diaminodiphenyl sulfone.<sup>111</sup> This split was thought to result from additional cure in the sample occurring during the DMA run. This additional cure was evidenced by an increase in storage modulus vs. temperature curves around the same range of the glass transition splitting. The storage modulus vs. temperature curve for sample shown in Figure 58b, however, did not show any increase around the temperature of the  $T_g$  shoulder but only a two stage drop. This would reflect inhomogeneous

crosslinking or differences in the molecular weight of chains between crosslinks ( $M_c$ ) rather than additional cure during the DMA run.

### *Analysis of the Dielectric Spectra*

#### *Secondary relaxations in cured networks.*

Figure 59 shows change in  $\tan \delta$  ( $\epsilon/\epsilon'$ ) and the dielectric loss permittivity ( $\epsilon$ ) vs. temperature at different frequencies for 33DDS/DGEBA and 44DDS/DGEBA. The  $\tan \delta$  vs. temperature curves show two distinct transitions. As depicted in the DMA curves in Figure 58a; two secondary relaxations, named  $\gamma$ - and  $\beta$ -peaks plus the glass transition were observed in the dielectric  $\tan \delta$  vs. temperature curves. A detailed explanation of the assignment of these peaks and the effect of variation in the crosslink structure on the motions associated with them will be given in this section.

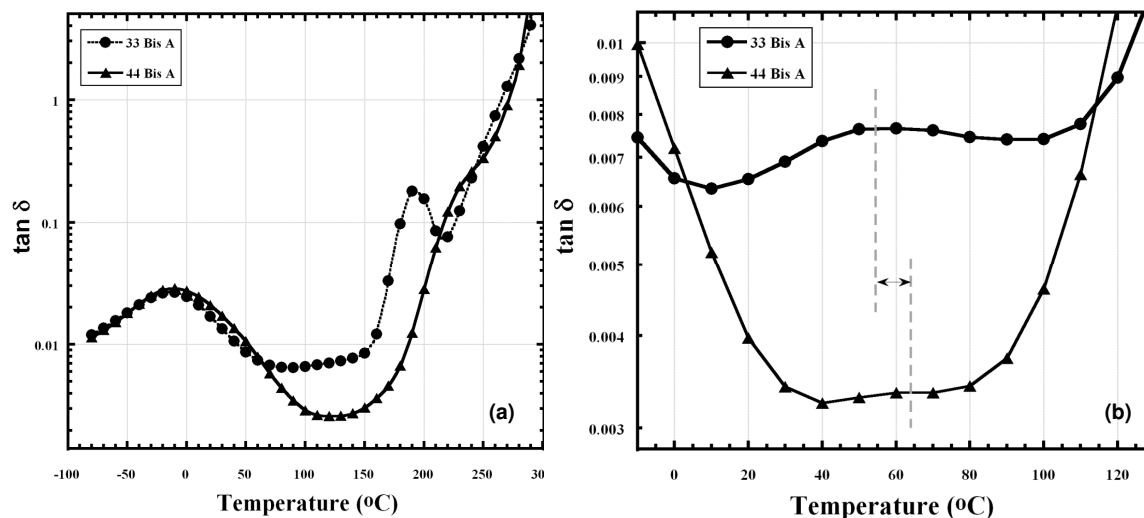


**Figure 59.** Dielectric  $\tan \delta$  vs. temperature at (a) 1 kHz and (b) 1 Hz, to show the  $\beta$  relaxation, for 33DDS/DGEBA and 44DDS/DGEBA. Dashed lines in (b) are used to show the  $\beta$  relaxation peak maxima.

### ***The $\gamma$ Peak***

The  $\gamma$ -transition peak was observed in cured epoxy networks having similar structures to those reported in previous work.<sup>112</sup> Johari and Mangion assigned this peak to be due to local motions of dipoles that remain as the unreacted components during the curing of the thermosets. The dipoles may be parts of the DGEBA polymer chain including the unreacted epoxy groups and/or free amino-diphenyl or primary amine groups. Ochi et al. proposed the mechanically observed  $\gamma$  transition to be due to the local motion of polymer segments consists of at least four carbon atoms.<sup>113</sup>

For the epoxy samples reported here, well-resolved  $\gamma$ -transition peaks for both the 33DDS and 44DDS crosslinkers are clearly shown. To characterize these transitions to the type of molecular motion and the chemical moieties responsible for this motion, static deuterium NMR ( $^2\text{H}$ ) experiments were conducted at different temperatures on selectively deuterated phenyl rings in the polymer. The necessary information to relate  $^2\text{H}$  NMR spectroscopy to DES includes the correlation time, from which Arrhenius plots can be created and activation energies and temperatures of 1Hz frequency motions can be calculated. This work involves complex simulated lineshape studies and is currently underway.

The same relative intensities of  $\tan \delta$  curves for both 33DDS/DGEBA and 44DDS/DGEBA could indicate that the flexible fragments of these polymers even in the glassy state have an equilibrium conformational structure. Thus, chains might exist in the form of an unperturbed coil in a densely crosslinked epoxy-aromatic amine glasses.<sup>114</sup> Therefore, high packing density is determined by the aromatic fragments of the polymer and the flexible aliphatic chains, created during the glycidyl rings opening during the cure process, helping the network

realize the highest possible packing density. To extract relaxation parameters of the  $\gamma$ -transition peaks, the Havriliak-Negami (HN) equation<sup>115</sup> was fitted to experimental data (Equation 15):

$$\epsilon^*(\omega) = \epsilon' - i\epsilon'' = -i \left( \frac{\sigma_{dc}}{\epsilon_0 \omega} \right)^N + \sum_{k=1}^3 \left[ \frac{\Delta \epsilon_k}{(1 + (i\omega\tau_{HN})^{\alpha_k})^{\beta_k}} + \epsilon_{\infty k} \right]$$

where:  $\epsilon_0$  = vacuum permittivity and  $\omega = 2\pi f$

The three relaxation terms in the sum and the term on the left account for D.C. conductivity. For each relaxation term  $k$ ,  $\Delta \epsilon_k = (\epsilon_R - \epsilon_{\infty})_k$ , the dielectric strength, is the difference between  $\epsilon'$  at very low and very high frequencies, respectively. In the first term  $\sigma_{dc}$  is the D.C. conductivity and the exponent  $N$  characterizes conduction in terms of the nature of charge hopping pathways and mobility constraints.  $\alpha$  and  $\beta$  characterize the breadth and degree of asymmetry, respectively, of  $\epsilon$  vs.  $\omega$  peaks.  $\tau_{HN}$  is the Havriliak-Negami (HN) relaxation time.

**Equation 15.** Havriliak-Negami expression.

The Havriliak-Negami (HN) relaxation ( $\tau_{HN}$ ) is related to the actual relaxation time at loss peak maximum at  $f_{max}$ , i.e.,  $\tau_{max}$ , by Equation 16:<sup>116</sup>

$$\tau_{max} = \tau_{HN} \left[ \frac{\sin\left(\frac{\pi\alpha\beta}{2(\beta+1)}\right)}{\sin\left(\frac{\pi\alpha}{2(\beta+1)}\right)} \right]^{\frac{1}{\alpha}}$$

**Equation 16.** Relation of  $\tau_{HN}$  to  $\tau_{max}$ .

The D.C. term accounts for inherent or unintended charge (impurity) migration that is often subtracted to uncover loss peaks or make them more distinct. The Havriliak-Negami (HN) equation was fitted to the data in Figure 60 and the relaxation time at peak maximum ( $\tau_{\max}$ ) extracted at each temperature. As shown in Figure 60, the frequency at loss permittivity ( $\epsilon''$ ) peak maximum,  $f_{\max}$ , shifts to higher values with increasing temperature in the usual fashion reflecting faster motions and smaller relaxation times, relaxation time  $\tau = 1/(2\pi f_{\max})$ .

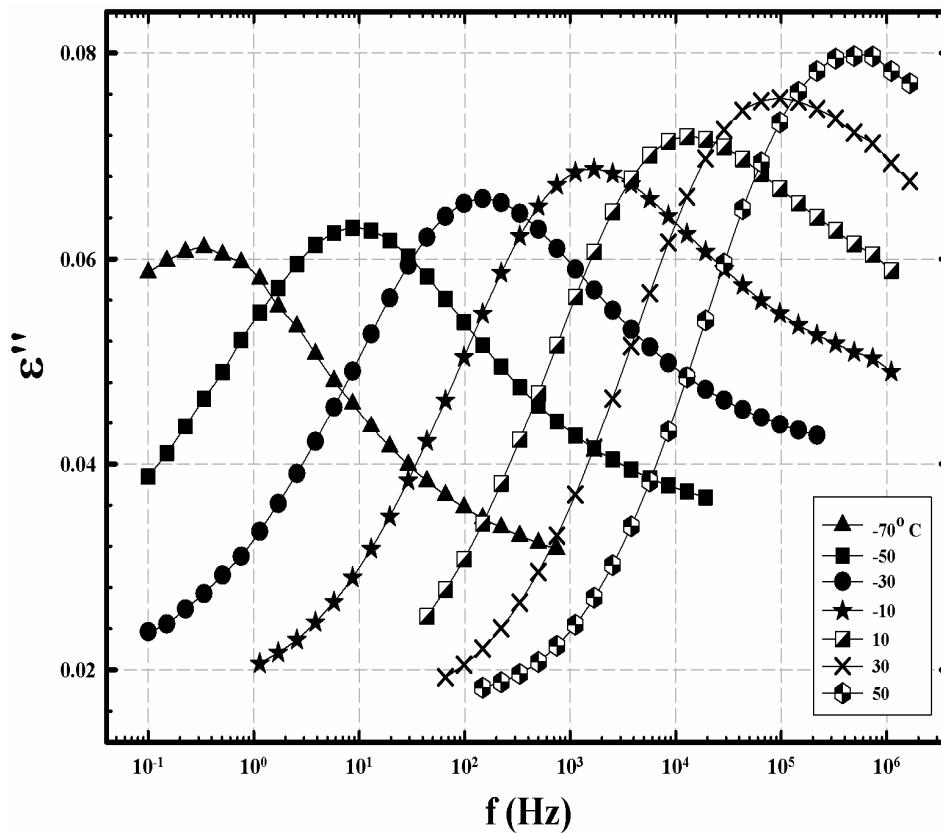


**Figure 60.**  $\epsilon''$  vs. frequency for different temperatures for 33DDS/DGEBA.

The  $\tau_{\max}$  was then plotted against temperature ( $T$ ) to show Arrhenius behavior for the  $\gamma$ -transition (Equation 17):

$$\tau(T) = \tau_0 \exp\left(\frac{E_a}{RT}\right)$$

where:  $\tau_0$  is the pre-exponential factor, R is the universal gas constant, and  $E_a$  is the activation energy for this transition.

**Equation 17.** Arrhenius expression for calculation activation energy

The analysis of this local motion shows that it has an Arrhenius type behavior with the same value of activation energy, 24.5 kJ/mol, for both 33DDS/DGEBA and 44DDS/DGEBA samples, as depicted in Figure 61. This fact strongly supports the idea that the internal rotation barriers in the considered fragments local motions are not sensitive to the presence of crosslinks in the polymer structure.

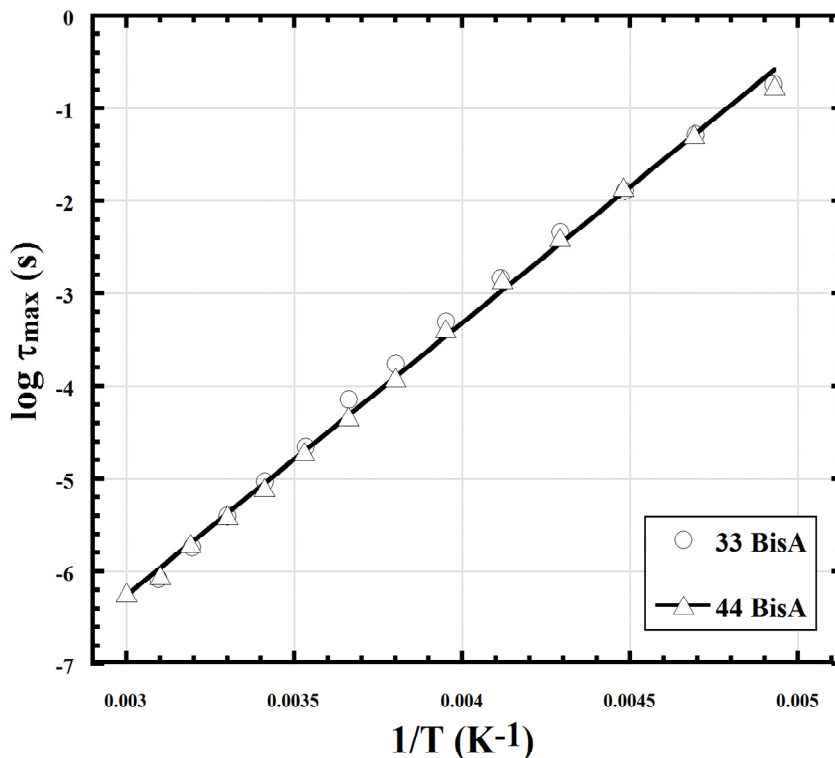


**Figure 61.** Arrhenius plots for 33DDS/DGEBA and 44DDS/DGEBA.

### ***The $\beta$ -Peak***

The  $\beta$  relaxation peak was assigned to the local motion of the dipolar groups which are created during the crosslinking reactions as previously reported.<sup>117</sup> Those groups include the hydroxyl ether and the secondary or tertiary amine groups.  $\beta$  relaxation peaks for the 33DDS/DGEBA and 44DDS/DGEBA networks are shown in Figure 59b. The comparison of  $\tan \delta$  vs. temperature curves had to be made at 1 Hz instead of at 1 kHz, the frequency used to clearly show the trends of the  $\alpha$  and  $\gamma$  relaxations. Perhaps this is related the nature of the dynamics of each of the three motions.

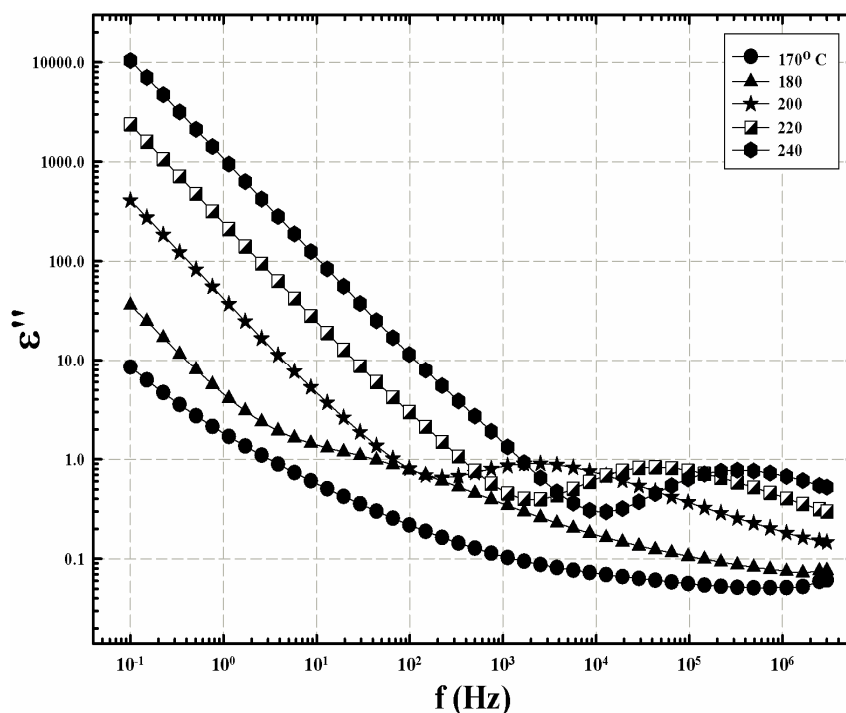
Two features can be clearly observed for the  $\beta$  relaxation peaks in Figure 59b, peak position and resolution.  $\beta$  relaxation peak strength, or resolution, is related to the number of active molecules or dipoles contributing to the relaxation. Therefore, the strength of this relaxation is affected by the nature of molecular packing in glassy state as well as nature of disorder in its rigid matrix.<sup>118</sup> Johari and Mangion reported that the rate of the  $\beta$  relaxation (its peak position) is less affected by the growth of a polymer chain or of a polymer network during first step of curing than is the rate of the  $\alpha$  relaxation; however, the strength of the  $\beta$  relaxation is more affected. As a consequence, the  $\beta$  relaxation becomes more prominent as the number of crosslinks and chain length increases during the curing process.<sup>119</sup> This conclusion suggests that 33DDS/DGEBA networks have higher number of crosslinks; consequently higher number of hydroxyl groups formed, and increased chain length compared to 44DDS/DGEBA.

Although it is difficult to compare both peak positions because of peak broadening and lower resolution in case of the 44DDS/DGEBA networks as shown in Figure 59b, peak position seems to shifts to *somewhat* lower temperature for 33DDS/DGEBA comparing to 44DDS/DGEBA networks. The  $\beta$  relaxation peak position is more sensitive to difference in

distribution of local volume within the network or the local space surrounding the mobile dipolar segments. Thus, different distributions of local volume within the network formed from 33DDS/DGEBA compared to 44DDS/DGEBA are apparent.

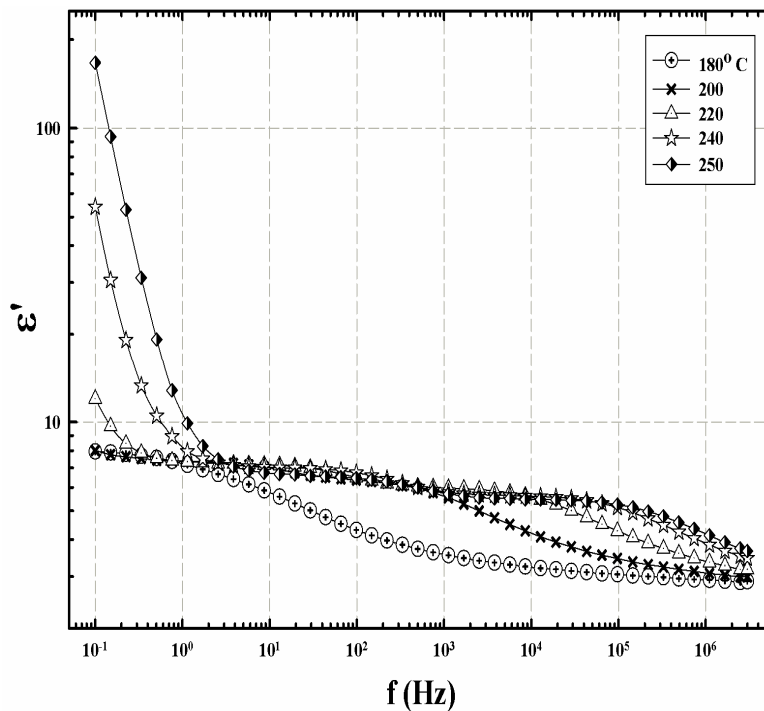
### *Glass Transition Dynamics in Cured Networks*

The glass transition or  $\alpha$  relaxation is associated with long range chain segmental mobility.  $T_g$  is closely related to the structure and crosslink density of the cured epoxy resins. The frequency at loss permittivity ( $\epsilon''$ ) peak maximum ( $f_{max}$ ) for the 33DDS/DGEBA sample shifts to higher values with increasing temperature in the usual non-Arrhenius fashion, as shown in Figure 62.



**Figure 62.**  $\epsilon''$  vs. frequency at different temperatures for 33DDS/DGEBA showing the glass transition related peak ( $\alpha$ -transition).

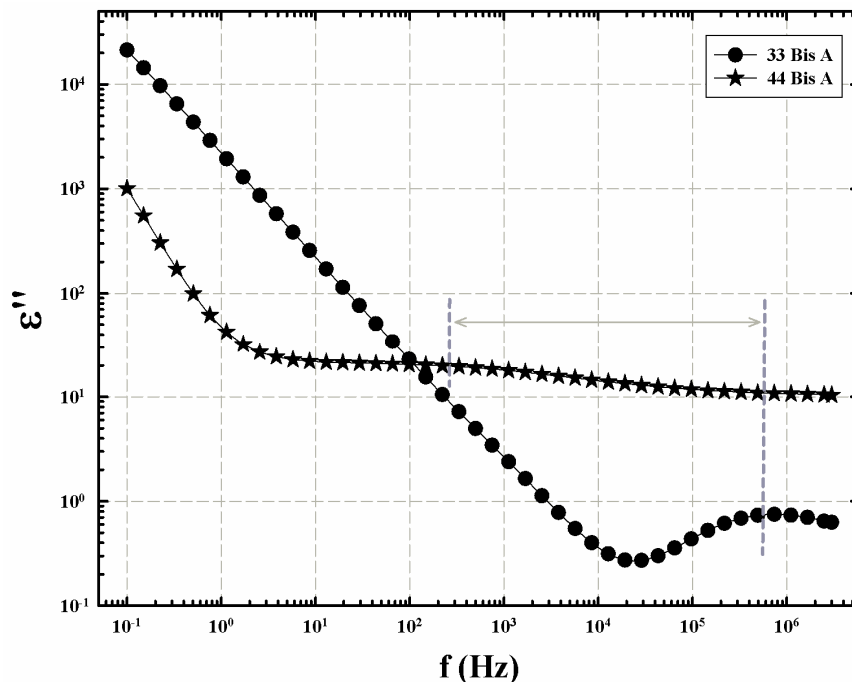
The upswing in  $\epsilon''$  at low  $f$  region of Figure 62 accounts for the presence of electrode polarization and D.C. conduction processes effects. The electrode polarization effect arises in resins from the ionic conductivity resulting from either intrinsic ions or residual impurity ions. When those ions become relatively mobile, due to larger chain mobility at the onset of the  $T_g$ , they have enough time to accumulate at the electrode-resin interface during one-half cycle of applied electric field at low frequencies.<sup>120</sup> The accumulated ion layers produce charged layers at both electrodes. The ion layers can have much greater charge per unit area than those produced from the actual material dipole orientation. Therefore, the measured sample capacitance becomes much greater than that produced by material dipoles and thus the dielectric storage permittivity ( $\epsilon'$ ) becomes much greater than the actual bulk permittivity. A large increase in  $\epsilon'$  values starting at 220°C is clearly seen in Figure 63 for the 33DDS/DGEBA sample. This increase is also observed for 44DDS/DGEBA.



**Figure 63.**  $\epsilon'$  vs. frequency at different temperatures for 33DDS/DGEBA showing the electrode polarization effects at high temperatures.

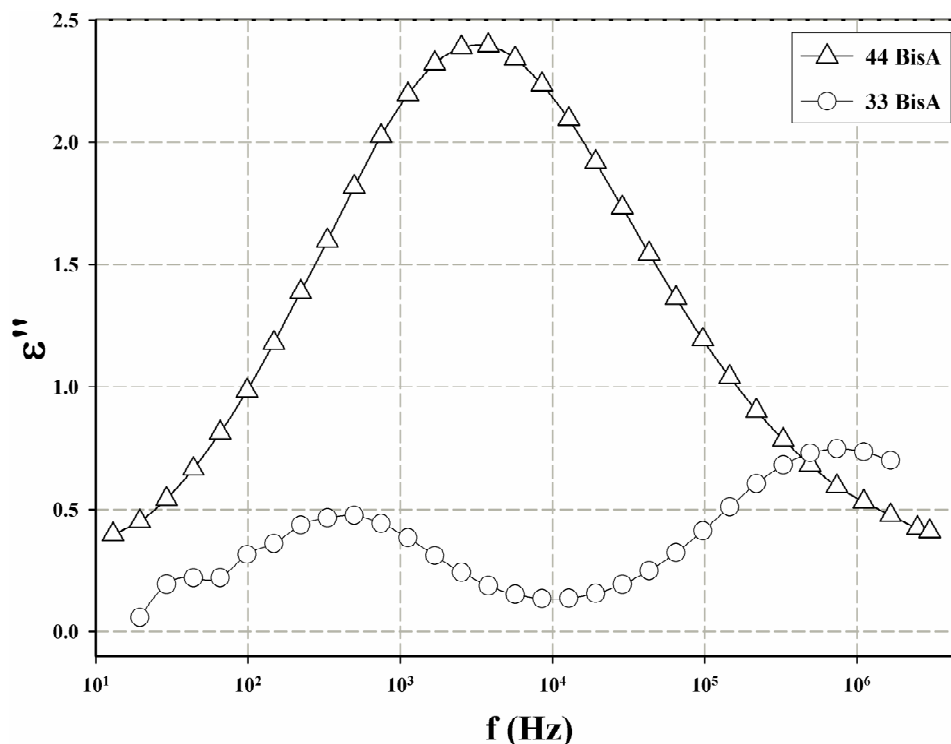
The second effect accounting for the upswing in  $\epsilon''$  at the low  $f$  region is the D.C. conduction effect which is expressed by the first term of the right side of the HN equation (Equation 15). D.C. conductivity in this context involves the instrumental sampling of charge hopping pathways that become progressively longer at increasingly lower frequencies. As the experimental time scale, or half period of oscillation  $= (2f)^{-1}$ , increases, charge carriers, likely intrinsic ions or residual impurity ions in this case, can execute more elementary hops before the applied field reverses. In this frequency region for  $T > T_g$ , LOG  $\epsilon''$  vs. LOG  $f$  plots are linear such that the slopes are slightly less than 1.0.<sup>121</sup>

Figure 64 shows  $\epsilon''$  vs.  $f$  at 250°C for 44DDS/DGEBA and 33DDS/DGEBA, showing the glass transition related peak. Dashed lines and the arrow are used to show the shift in relaxation peaks maxima. The  $\alpha$  relaxation peak maxima, although very broad, for the 44DDS/DGEBA sample shifts downward compared to 33DDS/DGEBA. This indicates a slower chain motion in the case of 44DDS/DGEBA, thus higher relaxation time (relaxation time  $\tau = 1/2\pi f_{\max}$ ). This result confirms the DMA results shown earlier in which the  $T_g$  is almost 50°C higher for 44DDS/DGEBA than 33DDS/DGEBA. Also, this same conclusion can be seen when comparing the dielectrically measured  $\tan \delta$  at 1 kHz shown in Figure 58a.



**Figure 64.** Comparison of  $\epsilon''$  vs. frequency curves at 250°C for 33DDS/DGEBA and 44DDS/DGEBA, showing the glass transition related peak ( $\alpha$ -transition). Dashed lines and the arrow to show the shift in relaxation maxima.

The  $T_g$  related relaxation spectra at different temperatures for the 33DDS/DGEBA and 44DDS/DGEBA samples were fitted to the HN equation. Then, the D.C. conductivity term was subtracted for the purpose of uncovering loss peaks corresponding to macromolecular motions. D.C. - subtracted loss spectra at 250°C for 33DDS/DGEBA and 44DDS/DGEBA are shown in Figure 65. Subtraction of the D.C. contribution causes the peaks to be more distinct and their shifts to higher or lower frequencies (shorter relaxation times) are more clearly seen. The nature of the  $T_g$  peak for the 33DDS/DGEBA network is bimodal, while the 44DDS/DGEBA glass transition appears as a very broad peak.



**Figure 65.** Comparison of  $\epsilon''$  vs. frequency curves at 250°C for 33DDS/DGEBA and 44DDS/DGEBA. The dc-conductivity term in eq. 1 is subtracted to resolve the  $T_g$  related relaxation peak.

The peak maximum for the 44DDS/DGEBA sample is shifted to lower frequency, indicating slower chain motion, when compared to one of the two peaks that appear for 33DDS/DGEBA. To further understand the nature of this bimodal  $T_g$  peak of the 33DDS/DGEBA sample, D.C. conductivity subtracted spectra at different temperatures are shown in Figure 66.  $T_g$  related transition shows two peaks, the first peak has its onset at 180°C, and peak maximum shifts to higher frequencies as temperature increases. The second peak has an onset at about 200°C and tracks with the aforementioned peak in moving to higher frequencies as temperature is increased. This behavior typically reflects an inhomogeneous network structure or differences in molecular weight of chains between crosslinks.

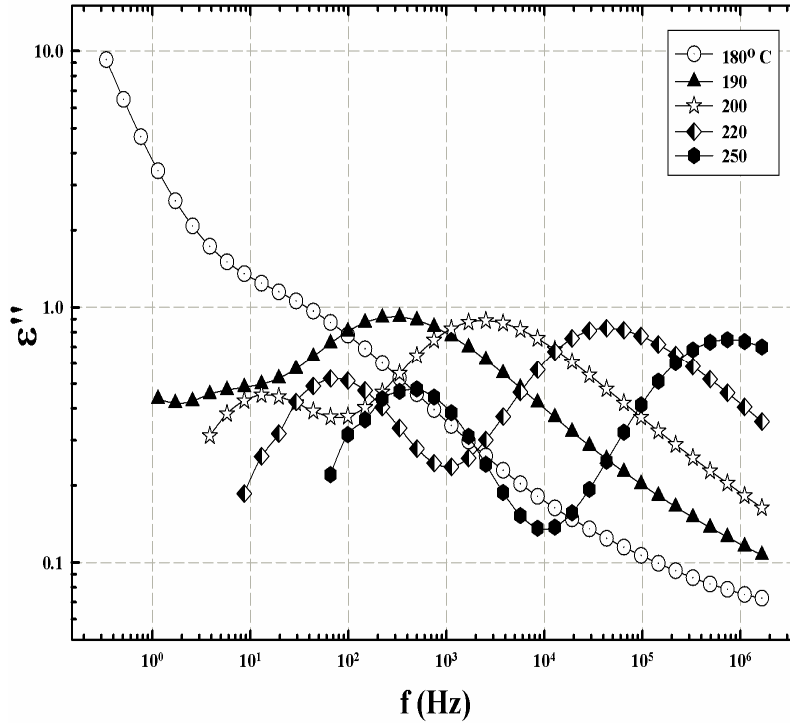


**Figure 66.** D.C. - conductivity subtracted spectra at different temperatures of  $T_g$  related relaxation peak for the 33DDS/DGEBA.

The HN equation was fitted to the data for both networks and the relaxation time at peak maximum extracted. The Vogel-Fulcher-Tammann-Hesse (VFTH) equation was then fitted to  $\tau_{\max}$  vs. Temperature ( $T$ ) data<sup>122</sup> as shown in Equation 18:

$$\tau(T) = \tau_0 \exp\left(\frac{E_a}{k_B(T - T_v)}\right)$$

where:  $k_B$  is the Boltzmann constant,  $\tau_0$  is a hypothetical relaxation time at infinite temperature.  $E_a$ , while having units of energy, is a ubiquitous quantity that it is not associated with an activated process in the usual sense.  $T_v$ , the Vogel temperature, is the temperature at which chain segments become frozen in a hypothetical situation in which a polymer is cooled quasi-statically from the rubbery state.

**Equation 18.** Vogel-Fulcher-Tammann-Hesse (VFTH) expression.

Figure 67 shows VFTH plots for networks of the two isomers, but each of the two peaks observed for the 33DDS/DGEBA sample, as shown in Figure 66, were fitted separately. The plots are quite nonlinear which implies that this is not a relaxation that can be described in terms of activated rate theory but is related to glass formation. The curve for the mean peak of the  $T_g$  of 33DDS/DGEBA is significantly vertically down-shifted relative to the 44DDS/DGEBA, indicating that chain motions become faster, and  $T_g$  is decreased in the 33DDS/DGEBA. It is interesting to note that the second  $T_g$  related peak for the 33DDS/DGEBA moves a little faster than the 44DDS/DGEBA peak until  $230^\circ\text{C}$  when they cross. This behavior is not clear at this point.

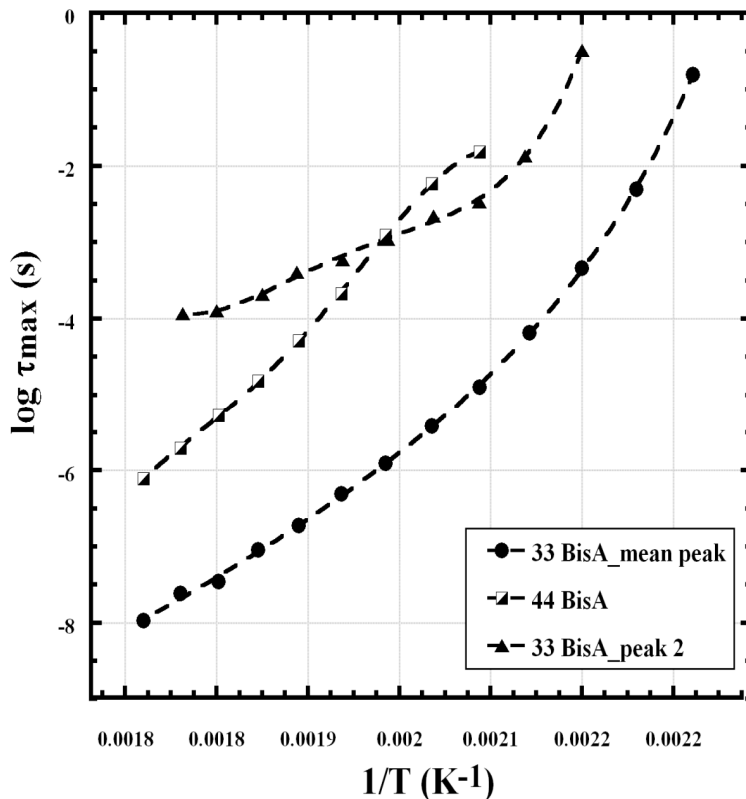


**Figure 67.** VFTH plots for the high temperature glass transition peaks of 33DDS/DGEBA and 44DDS/DGEBA.

Vogel temperature ( $T_V$ ) values were extracted from the curve-fitted VFTH data and were found to be 349 and 370K for the 44DDS/DGEBA and 33DDS/DGEBA (mean peak) samples, respectively. Thus,  $T_V$  increases for the 33DDS/DGEBA relative to the 44DDS/DGEBA, which suggests more restricted chain mobility for the 33DDS/DGEBA sample. Also, increased  $T_V$  suggests lower free volume per mass for the 33DDS/DGEBA sample, or more efficient packing of the local space surrounding the mobile dipolar segments. This result confirms free volume work conducted in the Nazarenko research group, clearly showing 33DDS-epoxies to possess lower free volume than 44DDS-epoxies.<sup>123</sup>

While this appears contradictory to the observed lower  $T_g$  of the 33DDS/DGEBA samples, this phenomenon can be explained by considering conformational entropy. The higher degree of chain packing in 33DDS is due to the conformational freedom given to 33DDS/DGEBA by the meta-substituted amine, which gives chains the flexibility to rearrange into better packed network. Interestingly, the increased conformational entropy of 33DDS which creates better chain packing and an increased  $T_V$  is the same property which lowers the  $T_g$  by allowing chains the flexibility to access more conformations at a lower temperature as the sample cools. Hence, 33DDS/DGEBA requires a greater amount of cooling to eliminate the configuration entropy than 44DDS/DGEBA and therefore has a lower  $T_g$ .

In the Havriliak-Negami equation,  $\alpha$  and  $\beta$  determine the distribution of relaxation times,  $G(\tau)$  such that  $\alpha$  characterizes the distribution breadth and  $\beta$ , by its deviation from unity, characterizes the degree of curve asymmetry [22].  $G(\tau)$  is given by Equation 19:

$$G(\tau) = \frac{\left(\frac{\tau}{\tau_{0i}}\right)^{\beta_i \alpha_i} \sin(\beta_i \Theta_i)}{\pi \tau \left[ \left(\frac{\tau}{\tau_{0i}}\right)^{2\alpha_i} + 2 \left(\frac{\tau}{\tau_{0i}}\right)^{\alpha_i} \cos(\pi \alpha_i) + 1 \right]^{\frac{\beta_i}{2}}}$$

where:  $\Theta_i = \arctan \left( \frac{\sin(\pi \alpha_i)}{\left(\frac{\tau}{\tau_{0i}}\right)^{\alpha_i} + \cos(\pi \alpha_i)} \right)$

The angular quantity  $\Theta_i$  has units in radians such that  $(0 \leq \Theta_i \leq \pi)$ .

**Equation 19.** Distribution of relaxation times from HN equation.

$G(\tau)$  plots at 250°C for 33DDS/DGEBA vs. 44DDS/DGEBA are shown in Figure 68. A bimodal curve is clearly observed for the 33DDS/DGEBA sample, while the 44DDS/DGEBA shows a much broader distribution of relaxation times. This could indicate broad distribution of molecular weight between crosslinks for the 44DDS/DGEBA while the 33DDS/DGEBA sample has an inhomogeneous network structure as discussed earlier. The shift in the distribution peak of 44DDS/DGEBA to longer relaxation times as compared to the mean  $T_g$  peak of the 33DDS/DGEBA sample, seen on the left side of the  $G(\tau)$  plot of 33DDS/DGEBA, supports the observed higher  $T_g$  of 44DDS/DGEBA.

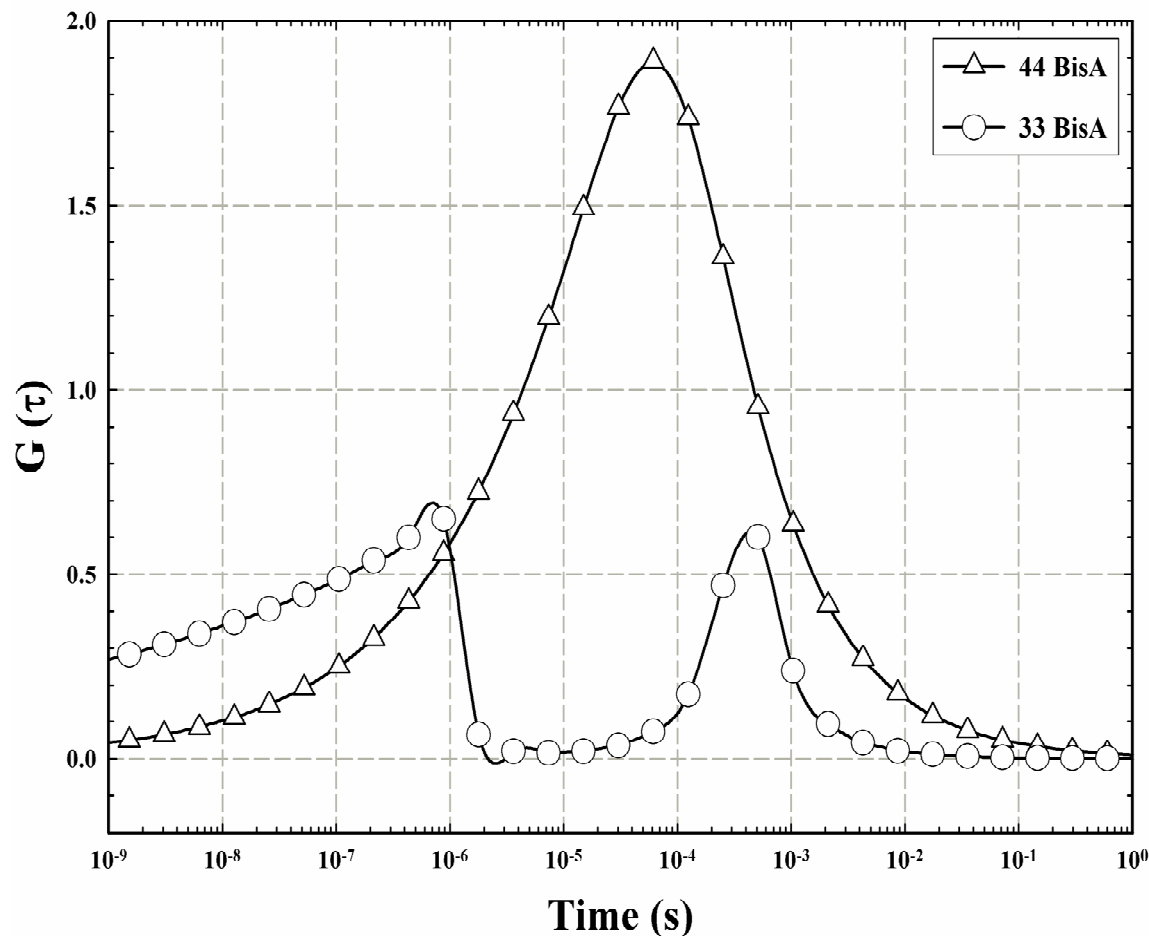


**Figure 68.** Distribution of relaxation times  $G(\tau)$  plots at 250°C for 33DDS/DGEBA and 44DDS/DGEBA.

In summary, broadband dielectric spectroscopy was used to examine macromolecular motions in epoxy networks formed from diglycidyl ether of bisphenol A and 3,3' vs. 4,4'-diaminodiphenyl sulfone isomers as crosslinkers. Dynamics of the secondary and glass transition related relaxation of the fully cured networks were analyzed and fitted to the Havriliak-Negami equation. The sub- $T_g$   $\gamma$  relaxation peak maximum,  $f_{max}$ , shifts to higher values with increasing temperature in an Arrhenius fashion with similar activation energies for the two crosslinker isomers. This result supports the proposed assignment of the  $\gamma$  relaxation to account

for the phenyl rings flipping in the main DGEBA chain facilitated by the presence of adjacent flexible ether linkage. 44DDS/DGEBA networks exhibited higher  $T_g$  relative 33DDS/DGEBA networks as indicated by both dynamic mechanical analysis and broadband dielectric spectroscopy results.

$T_g$  related relaxations spectra fitted to the Havriliak-Negami equation for networks of both isomers showed evidences for the higher  $T_g$  of 44DDS/DGEBA. This was clearly seen in D.C. subtracted  $\epsilon''$  vs.  $f$  spectra and the VFTH plots of samples of both isomers.

Vogel temperature showed an increase for the 33DDS/DGEBA network relative 44DDS/DGEBA, suggesting lower free volume per mass or more efficient packing of the local space surrounding the mobile dipolar segments. The distribution of relaxation times,  $G(\tau)$ , curves showed a bi-modal network structure for the 33DDS/DGEBA, suggesting microstructural heterogeneity in this sample or heterogeneity in its crosslink density.

## **RESULTS PART VII**

### **UNIAXIAL COMPRESSION ANALYSIS OF GLASSY POLYMER NETWORKS USING**

#### **INTRODUCTION**

The rapid proliferation of polymer composites for use in primary structure of aerospace and marine applications is profound and leading to a heightened requirement to improve failure modes. Since the composite structures generally realize less than 40% capability of the fiber reinforcements, it is a logical nexus to conclude failure modes are primarily matrix dominant. Strain Invariant Failure Theory (SIFT), or more recently termed “Onset Theory”, proposes the matrix critical effective properties of the lamina that control damage initiation are the effective volumetric and equivalent strains of the polymer<sup>124</sup>. Equivalent strain is a function of the second invariant of the strain deviator tensor associated with uniaxial compression yield. Accurate determination of this point is therefore fundamental in understanding how a composite will react to a high stress event. Uniaxial compression testing is valuable to optimize critical yield properties of glassy polymer networks, and accurate determination of strain behavior is necessary to advance matrix performance. The matrix yield characteristics are difficult to obtain in tension since tensile yield stress is greater than the fracture stress for highly crosslinked glassy networks leading to brittle failure prior to macroscopic yield<sup>125</sup>. Inherent brittleness is not a detriment in uniaxial compression, allowing for loading through the yield point. Comprehensive analysis of these properties, as well as small strain behavior, requires accurate and reproducible strain data acquisition.

Proper uniaxial compression testing of glassy networks is complex. Uniform load is critical since platen or specimen surface misalignment creates non-linear force-displacements at low strain levels, and pre-mature specimen failure at high strain<sup>126</sup>. Accurate strain measurement in compression is particularly difficult since test specimens are relatively small cylinders which require special extensometers or bonded-on strain gauges which are cumbersome to handle, provide limited test data and require high skill for accuracy. Compression testing sub-pressure fixtures which maintain appropriate platen alignment are also restricting as they reduce the amount of work area around the specimen to affix strain measurement devices. For these reasons non-contact strain measurement devices such as video or laser extensometers are useful for compressive testing, however they are limited to a fixed gauge length and only measure strain between extensometer edges (contact) or specimen surface marks (non-contact)<sup>127</sup>. In the case of strain gauges, only the specific points of bonding are measured.

Digital image correlation (DIC), also referred to as photogrammetry, was developed in the early 1980's at the University of South Carolina as a method for the full-field analysis of surface strain. This method is based on the calculation of surface deformation using a set of digital images from un-deformed and deformed states<sup>128,129,130</sup>. The technique consists of capturing gray-scale images of a random or regular surface pattern using one or two CCD cameras. The surface pattern is typically applied in the form of dark speckles on top of a white/high contrast base, providing patterns that can be easily recognized from image to image. This surface pattern deforms during loading. Image facets are created within the captured images allowing for surface coordinates and deformation to be tracked from image-to-image with sub-pixel accuracy. Upon conclusion of processing, a complete strain map of the specimen surface is obtained<sup>131,132,133</sup>. Originally developed as a 2D technique, measurements utilize a

single camera focused directly on the surface of a planar specimen undergoing planar deformation as seen in Figure 69A. This technique is limited by the requirement that the specimen must undergo only planar motion. Out of plane motion and lack of parallel positioning introduces error into the measurement making 2D digital image correlation impractical to apply to cylinders in uniaxial compression<sup>134</sup>. Therefore, a relatively new, 3D DIC technique applied to uniaxial compression of glassy polymer cylinders is the subject of this research. This three dimensional technique involves the use of two digital CCD cameras. The cameras are placed so the specimen surface is viewed from two different angles (Figure 69B) creating a full field three-dimensional measurement of the specimen shape and displacements.

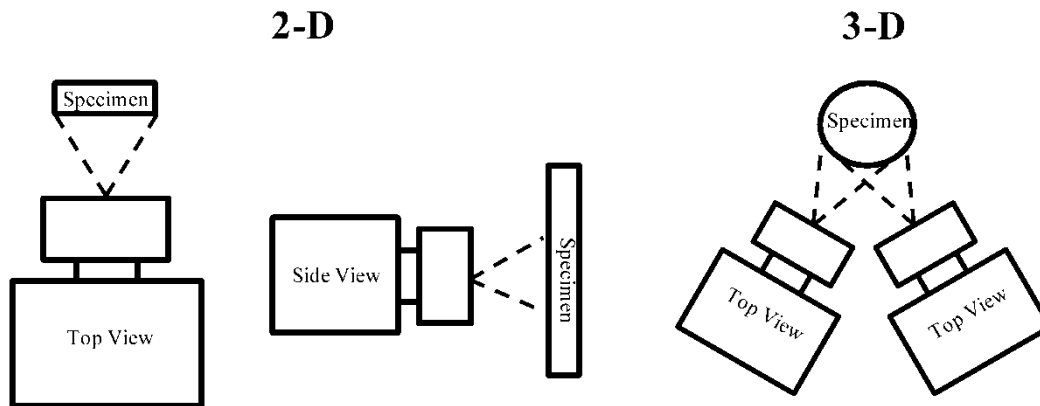


**Figure 69:** 2D DIC (A) and 3D DIC (B)

Use of DIC as an analytical technique has grown rapidly in recent years as hardware and software advancements have improved its viability. A large amount of research has been conducted on tensile behavior of materials using this technique, including the necking behavior of thermoplastics<sup>135,136</sup> and failure mechanisms of composite coupons<sup>137,138</sup>. However, the

development digital image correlation to study uniaxial compression of glassy polymer solids has not been reported. This paper presents analytical methods for the application of 3D digital image correlation to study uniaxial compression of glassy solids. We have found this technique particularly useful to gain a better understanding of how these matrices deform at low strains, pre-yield, yield and post-yield.

### **Materials**

Bisphenol A diglycidyl ether (DGEBA, EPON 825, 175 gram per equivalent, Hexion Specialty Chemicals Co.) and 4,4'-diaminodiphenyl sulfone (DDS, 97%, Aldrich Chemical Co.) were used as received. Chemical structures are depicted in Figure 70.

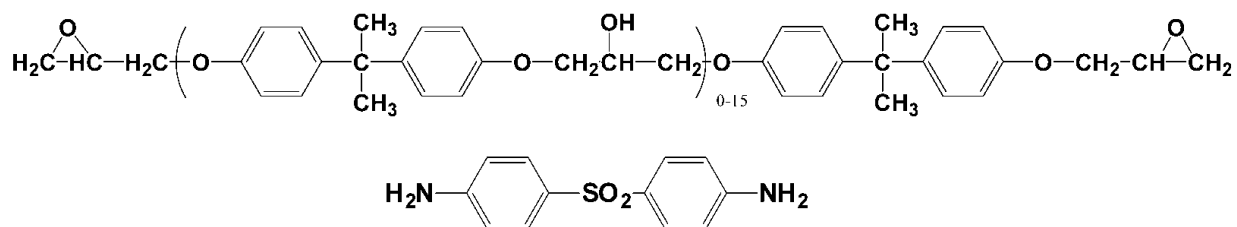


**Figure 70:** Chemical structures for DGEBA and 4,4'-DDS

### **Methods**

#### ***Glassy Polymer Network Preparation***

In a typical reaction, 200.0g (571.4 mmol) DGEBA was charged to a 500mℓ Erlenmeyer flask equipped with a vacuum fitting and magnetic stirring device. The epoxy prepolymer was heated to 100°C when 70.9g (285.7mmol) 4,4'-DDS ground powder was slowly added over a 10-15 minute period to avoid agglomeration. Upon addition, vacuum was slowly applied to a

level of  $\sim 10^{-3}$  Torr when the temperature was increased to 120°C and the mixture was stirred until dissolution of amine was observed. Vacuum was removed, the clear solution was poured into preheated (100°C) 2-part PTFE cylinder molds (internal cavity 25.4mm diameter x 152.4mm length) and the polymer was cured for 5h at 125°C and 1h at 200°C. Upon cooling, the glassy polymer network cylinder was precision lathed into three 12.70mm diameter x 25.40mm length compression test cylinders with perfectly parallel loading surfaces. Specimens were conditioned for 48h at 28°C and 50% RH prior to testing.

### ***Uniaxial Compression Testing***

Compression testing procedures followed ASTM 695-02a. Cylinders were compressed at a displacement controlled test rate of 1.27mm/min on a MTS Systems Corporation Model 810 servo-hydraulic universal test frame equipped with a low friction compression sub-press (Wyoming Test Fixtures Model CU-SP). Linear variable differential transformer (LVDT) compression data was recorded from MTS Testworks® software using a MTS 20 kip load cell at a sampling rate of 10Hz. Compression strain measurements were recorded simultaneously using digital image correlation methods.

### ***Digital Image Correlation Measurement***

Advanced strain analysis using digital image correlation (DIC) was conducted using a GOM Optical Measuring Techniques ARAMIS 3D Deformation Analysis System (Trilion Quality Systems). DIC requires specimens are “speckle coated” to create a non-uniform surface pattern which is tracked by the ARAMIS software between digital images captured during the deformation test. Speckle patterns were created on the glassy polymer network cylinder surfaces using white and black aerosol paints. A solid white basecoat was first applied and then followed

by a misted black paint which created black speckles in the size range of 2-5 pixels<sup>139</sup>. A typical speckle pattern and experimental setup for compression cylinders is shown in Figure 71. Digital gray scale images were captured via two 2M digital CCD cameras equipped with 50mm lenses at a frame (capture) rate of 5fps for small strain analysis. When appropriate, the capture rate was reduced to 1fps to minimize digital data file size and computation time. Calibration was performed using a 25mm x 20mm standard to obtain a resolution deviation of less than 0.03 pixels. Digital images were stored for post-test processing and analysis.

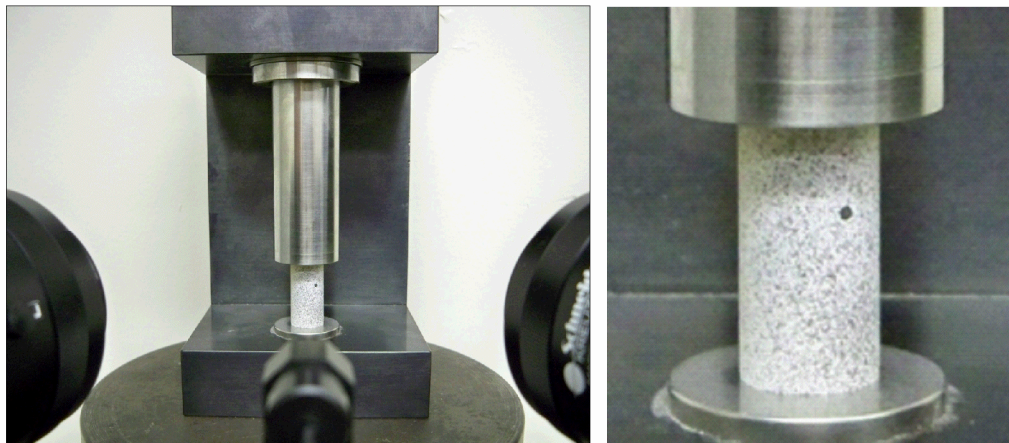


**Figure 71:** Low-friction compression sub-press showing speckle patterned cylinder

### ***Digital Image Correlation Analysis***

A distinct benefit for DIC compared to traditional mechanical testing methods is post-test analysis. Prior to analytical processing, digital images were taken through a series of steps to increase accuracy and decrease computation time. The first step was to define analysis areas for image processing and reduce image sizes to optimize data. Image sections, typically edges that did not display optimum contrast due to shadows or low light artifacts were eliminated to

enhance computational analysis. These steps were particularly useful for analyzing compression specimens since cylindrical surfaces create unique edge effects associated with shadowing and pixel mapping. Facets, defined by pixel size and step length, were generated in grid patterns across the optimized areas of the digital images. Facet size is the true dimension of the defined area in pixels. Step length is the distance between adjacent facet centers, with smaller steps leading to increased spatial resolution. Upon facet definition, a start point was defined for the initial image set. The start point provides a reference for the software to recreate the initial facet field on subsequent image sets to quantify three dimensional strains<sup>140</sup>. During computer computation the gray scale speckle pattern is tracked within each rectangular facet from image-to-image. A three-dimensional displacement gradient tensor field is calculated based on the change in facet coordinates with respect to the facet center. Using this displacement field, strain tensors are calculated to create strain distribution profiles capable of displaying both major and minor strain of the specimen during loading.

### ***Small Strain Analysis***

**Modulus:** Digital image correlation provides a non-contact method to analyze surface strains of material properties under deformation and compliments traditional measurement techniques. When studying the compression behavior of glassy polymer solids, the most prolific advantage of DIC is enhanced accuracy of small strain measurements. The compression sub-press used for studying these materials is space constrained, making it quite difficult to apply an extensometer or strain gages. As a result, the test often relies on LVDT measurements which generate accuracy concerns. Figure 72A compares the compressive stress-strain curves for the DGEBA-DDS cylinders generated from LVDT and DIC measured strain. Although the curves

have similar shapes and yield stresses, significant differences in the small strain regions (Figure 72B) are observed as the DIC data displays a larger initial slope and calculated modulus.

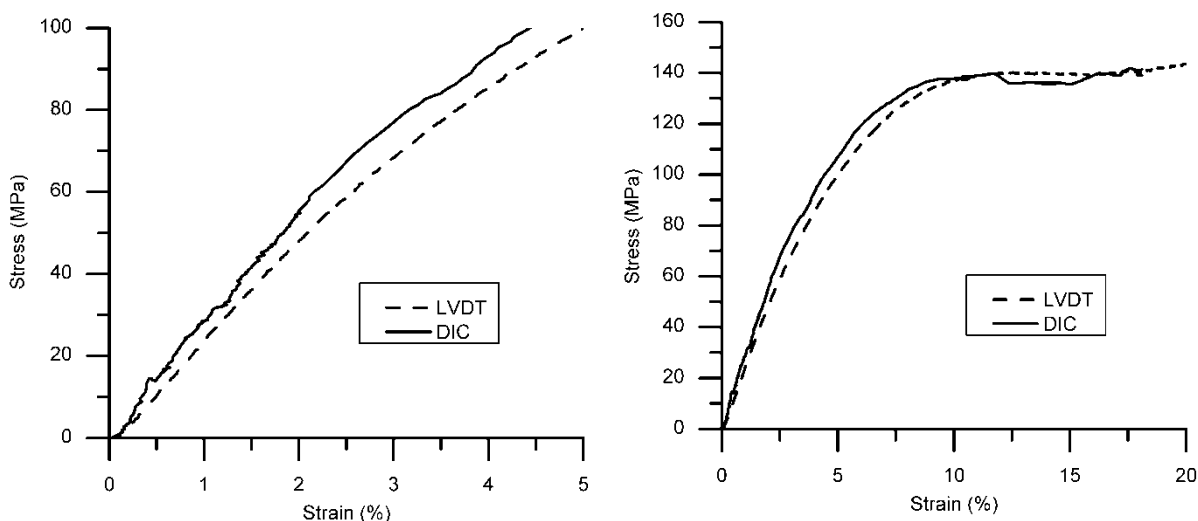


**Figure 72:** DIC and LVDT stress vs. strain (A) and small strain region (B) comparison

To quantify these differences, a comparison of the apparent modulus values at different longitudinal strains for DIC and LVDT are shown in Figure 73 (average of two tests). Values were determined by the slope of a linear fit to the stress-strain curves in 0.25% increments of longitudinal strain. Modulus values generated from LVDT increased to a maximum of 2670MPa at 0.75% strain. The increase in modulus from 2301MPa at 0.25% strain to this maximum is attributed to erroneous displacements in the small strain region. DIC calculated modulus values do not show this behavior since the measurement is independent of machine and fixture compliance, and only the actual strain deformations of the specimen under compression are measured. Thus, modulus values are highest at the lowest longitudinal strains and subsequently decrease in a near linear fashion. Peak modulus values were determined to be 3757MPa for DIC measurements at 0.25% strain. These observed differences of 1087MPa and 0.50% strain

between techniques demonstrates the improved accuracy in small strain measurements of DIC when measuring uniaxial compression modulus of glassy polymer matrices.

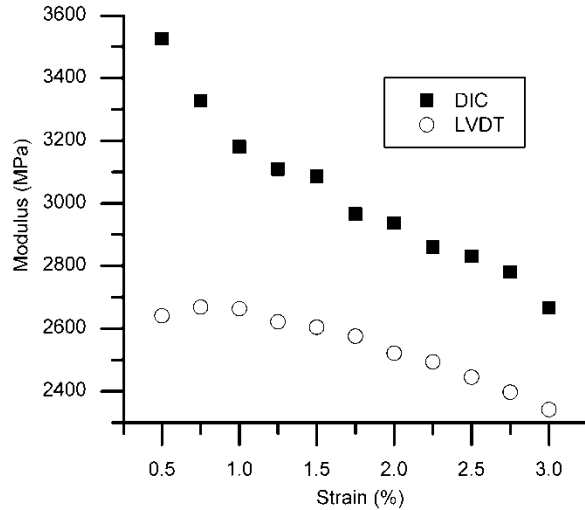


**Figure 73:** DIC and LVDT apparent modulus comparison

**Poisson's Ratio:** Since strain measurements in DIC are calculated from deformations in surface facets, transverse and longitudinal strains can be measured simultaneously. As a result, calculation of Poisson's ratio for glassy polymer matrices is attainable without the use of multiple extensometers or strain gauges. Figure 74 shows a representative plot of the nominal Poisson's ratio determined from DIC calculated longitudinal and transverse strains. Using this approach, we calculated the Poisson's ratio for the DGEBA-DDS network to be 0.36 at peak modulus, or 0.25% longitudinal strain.

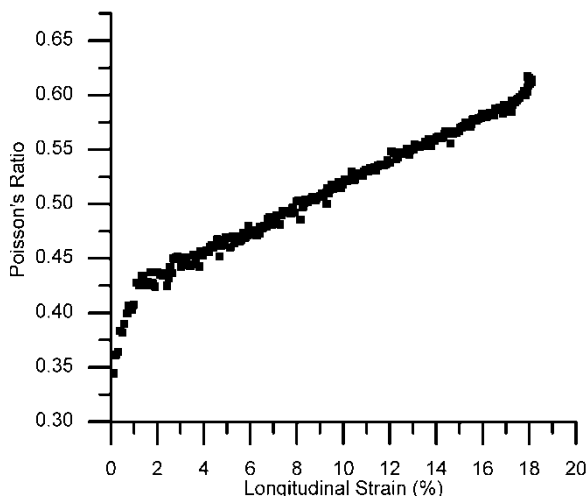


**Figure 74:** DIC nominal Poisson's ratio vs. longitudinal strain

### ***Yield Analysis***

For the purpose of this manuscript we will consider the yield point of the glassy polymer network to correlate with peak load or the apparent “knee” in the stress vs. strain curves. Correlation of MTS load data with digital image sets allowed us to assign the specific image set where peak load occurred. We used this image set to assign a uniaxial compression yield strain of 11.61% by averaging the total surface strains for the DGEBA-DDS glassy network. In comparison, the LVDT measured compression yield was 12.42% for this sample. This difference of 0.82% strain is significant and suggests 0.208mm of compliance strain for the LVDT measurement. As a result, we believe DIC is an excellent technique to determine the total compliance within an experimental set-up.

Digital image correlation is particularly useful for studying the pre-yield and post-yield strain behaviors of glassy polymer networks in uniaxial compression. To examine pre- and post-yield strain behavior, strain profiles at various stages throughout the compression test were analyzed. Figure 75 shows three DIC pre-yield capture images (stages 48, 80, and 103), and

three DIC post-yield capture images (stages 144, 165, and 194). As discussed, each capture image is generated from individual picture frames calculated as a three-dimensional displacement gradient tensor field compared with the start point. Prior to yield, the strain profiles show uniform strain across the image as indicated by small and barely noticeable color gradients from top to bottom. Once the glassy polymer cylinder yields, the material undergoes gross plastic deformation through “barreling” which results in a more significant strain gradient across the specimen.

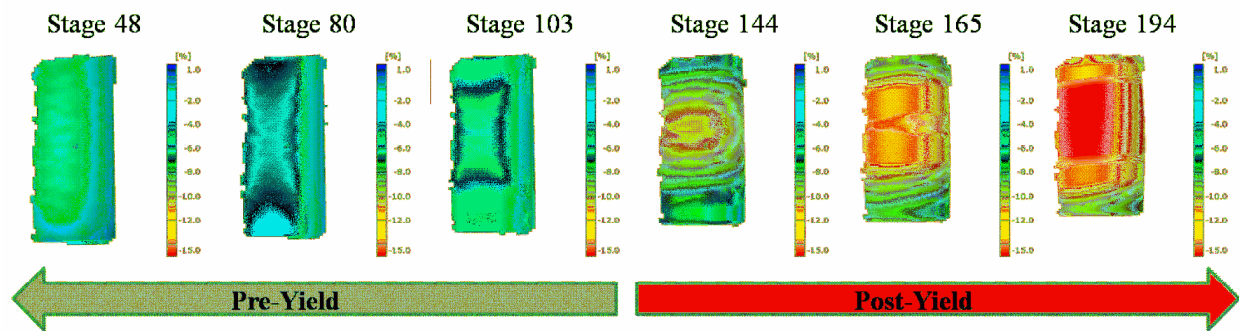


**Figure 75:** DIC pre- and post-yield capture images

Analysis of pre-yield strain using DIC suggests deviation from uniformity begins well before the yield point of the matrix. Figure 76 presents a post-test digital analysis and plots the minor (longitudinal) strain vs. time for two stage points. Stage points are individual digital points selected by the analyst on the surface of the specimen. In this example, we selected points in regions of the cylinder where we observed high longitudinal strain and low longitudinal strain to probe the onset of strain deviation within the glassy polymer network. At the yield point (11.61% average minor strain, time ~150s) the value of strain between these two stage points is deviated >5%. This result confirms the specimen does not deform at a uniform strain rate prior to yield. In fact, the strain deviation between these stage points began at ~27s, or a longitudinal

strain of 2.02%. Pre-yield deviation progressed slowly compared to post-yield deviation as observed in Figure 76. This post-yield behavior is attributed to the gross plastic deformation barreling of the glassy network cylinders.

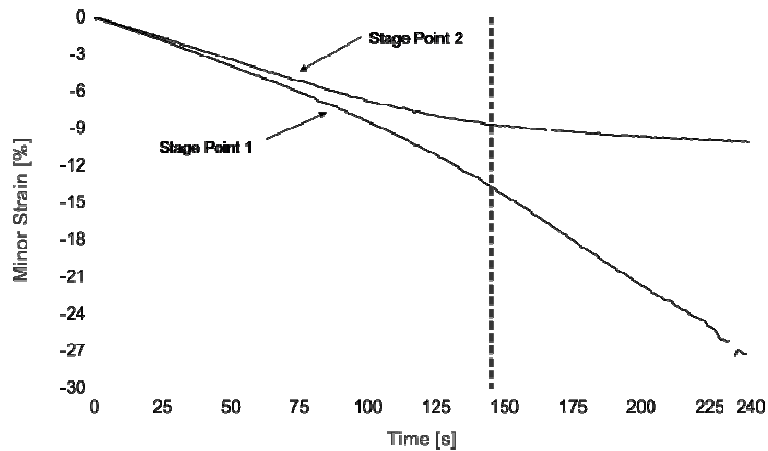


**Figure 76:** Minor strain vs. time for two stage points

Pre-yield strain deviation was further explored by comparing DIC minor strain vs. time to the traditional MTS compression stress vs. strain curve for the glassy polymer network in Figure 77. The traditional stress vs. strain curve is divided into three regions: elastic, anelastic, and plastic. These strain regions are distinguishable based upon their recovery behaviors.

Instantaneous strain recovery is the elastic deformation component. Recovery over a certain length of time and/or temperature is the anelastic deformation component and any non-recovered strain is considered irreversible or the plastic deformation component<sup>141,142,143</sup>. These strain regions are segmented in the traditional stress vs. strain curve in Figure 77A with the elastic component assigned to the initial linear portion of the curve, the anelastic component assigned to the pre-yield non-linear segment of the curve and the plastic component assigned to the post-yield segment of the curve. Comparing the DIC strain vs. time plot in Figure 77B indicates the

initial deviation of stage points at 2.02% correlates with onset of the anelastic strain component. This result is significant since the onset of non-uniform strain across the surface of the specimen correlated precisely with the elastic to anelastic transition of the traditional method.

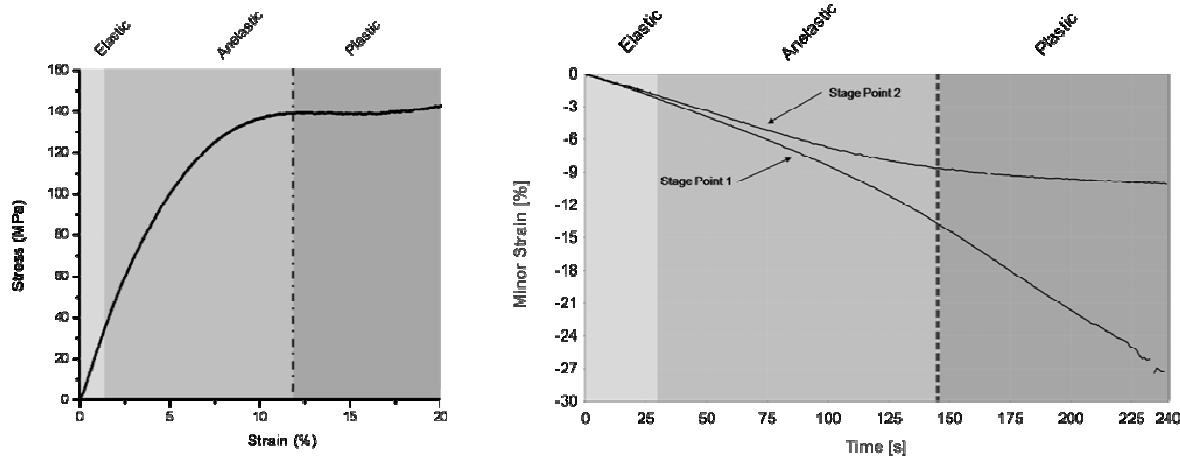


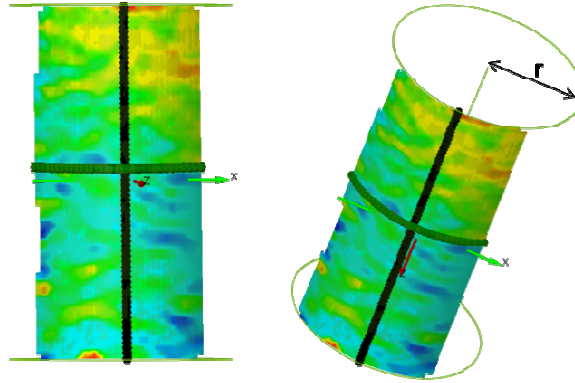
**Figure 77:** Traditional stress vs. strain (A) and DIC strain vs. time (B) comparison

### ***True Stress and Strain***

DIC is useful for the calculating true compression stress and strain of glassy polymer networks. Prior discussion has been based on nominal strain values determined from the DIC software and stress values calculated by  $\sigma_n = F/A_0$ , where  $F$  is the force, and  $A_0$  is the initial cross-sectional area of the cylinder. True strain values were generated from the DIC software and true stress was calculated as  $\sigma_t = F/A$ , where  $A$  is the actual cross-section of the specimen at force  $F$ . Difficulty arises in calculating true stress due to limitations in obtaining accurate real-time cross sectional areas. Traditional methods calculate these values from the Poisson's ratio. However, it is difficult to calculate a precise Poisson's ratio in compression testing as discussed above. DIC computational analysis provides a method to apply a best-fit cylinder to 3-D cylindrical specimen surfaces. We applied this technique to calculate the glassy network cylinder radius

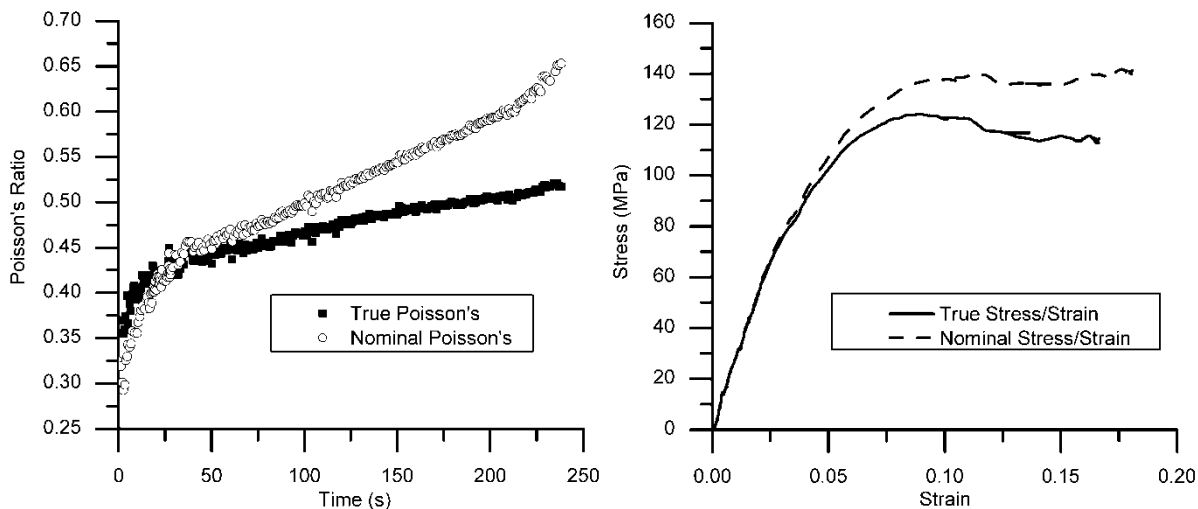
throughout the compression loading test to determine actual cross-sectional area with time.

Figure 78 depicts how the best fit method was applied to determine the radius of the cylinder.



**Figure 78:** Best-fit cylinder

Figure 79 compares the true stress vs. true strain curve with the nominal stress vs. strain curve for uniaxial compression of the DGEBA-DDS polymer network. The true stress vs. true strain curve more accurately depicts strain softening associated with increased radius due to specimen barreling. For this experiment, we observed an increase in radius from 6.395mm to 6.689mm at yield. We also used the true longitudinal and transverse strains to calculate the true Poisson's ratio. The true Poisson's ratio at peak modulus was calculated at 0.36 which is identical to the nominal Poisson's ratio presented above.



**Figure 79:** DIC true and nominal stress-strain curve comparison

Compression measurements of glassy networks are fraught with challenges associated with extensometers or strain gages since the sub-press has limited space and samples are relatively small. We found this non-contact technique simple to use and advantageous to generate accurate/reproducible data for analyzing compression modulus, Poisson's ratio, and yield strain. DIC provides a substantial increase in accuracy for measuring strain compared to LVDT, and also allows for simultaneous longitudinal and transverse strain measurements to calculate Poisson's ratio. DIC is particularly sensitive for measuring small strain compression modulus. DIC techniques are useful for studying the pre-yield, yield and post-yield behavior of glassy polymer solids and provide insights to the non-uniform strain behavior of these materials prior to yielding. Uniform strain was only observed in the purely elastic strain region during compression, and a slow deviation in surface strain was then observed through the anelastic region. An accurate yield strain was obtained using DIC which clearly eliminated erroneous strain data associated with fixture and equipment compliance. Finally, DIC allows for the

calculation of true compression stress and true compression strain by calculating a best-fit cylinder from a 3-dimensional surface map to monitor the change in radius throughout the test.

***Multi-Scale Validation: Finite Element Analysis of the 10° Off-Axis Coupon Test Using DIC***

Validation of the Boeing physics-based Onset Theory requires the existence of structural tests where the effective onset of damage initiation coincides with complete 2-piece (catastrophic) failure of the structure (or coupon). There are not very many cases where this condition can be rigorously satisfied. With respect to the distortional strain invariant, the 10° off-axis coupon satisfies this requirement. Loaded in tension the coupon fails catastrophically into two pieces (see Figure 80).



**Figure 80:** Two-piece failure

The micromechanically-enhanced FE solution for the distortional strain invariant (at failure) is shown in Figure 81. As can be seen, a NUMERICAL singularity exists at the fixed support and obscures the true location of the peak response of the matrix dominant strain invariant. It is clear that failure initiation can only take place in the space (along the edge) between the location where the fiber passes through the centroid of the coupon and where the part is supported by the fixture (see Figure 82). As a result, numerical solutions have been

conservatively extracted at the point where the fiber passing through the centroid intercepts the coupon edge. This resulted in good correlations with other sources of the critical distortional strain invariant. What has been lacking is experimental evidence supporting the above hypothesis.

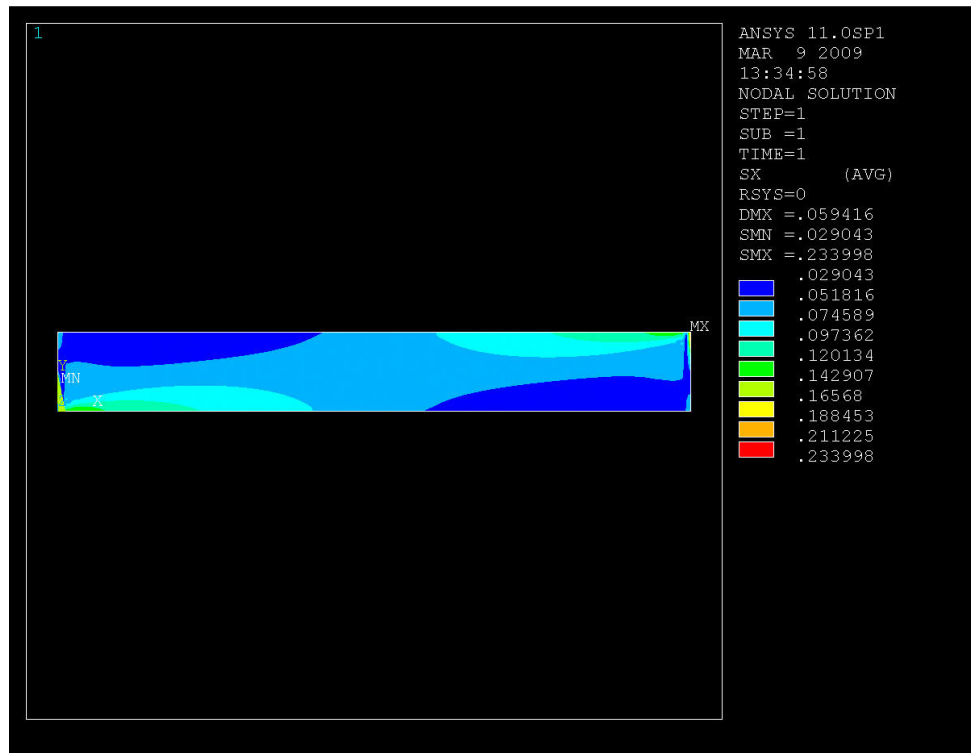


**Figure 81:** Micromechanically Enhanced FE solution for the Distortional Strain Invariant  
(Jon Gosse, Boeing)

This research has developed experimental techniques to validate finite element models used for improving Onset Theory multi-scale models for aerospace. A numerical analysis of the homogenous strain (applied mechanical only) along the part axis is shown in Figure 83. The experimentally determined contour plot of the same strain component is shown in Figure 84 for a 10° off-axis coupon of a different material than that of Figure 80.

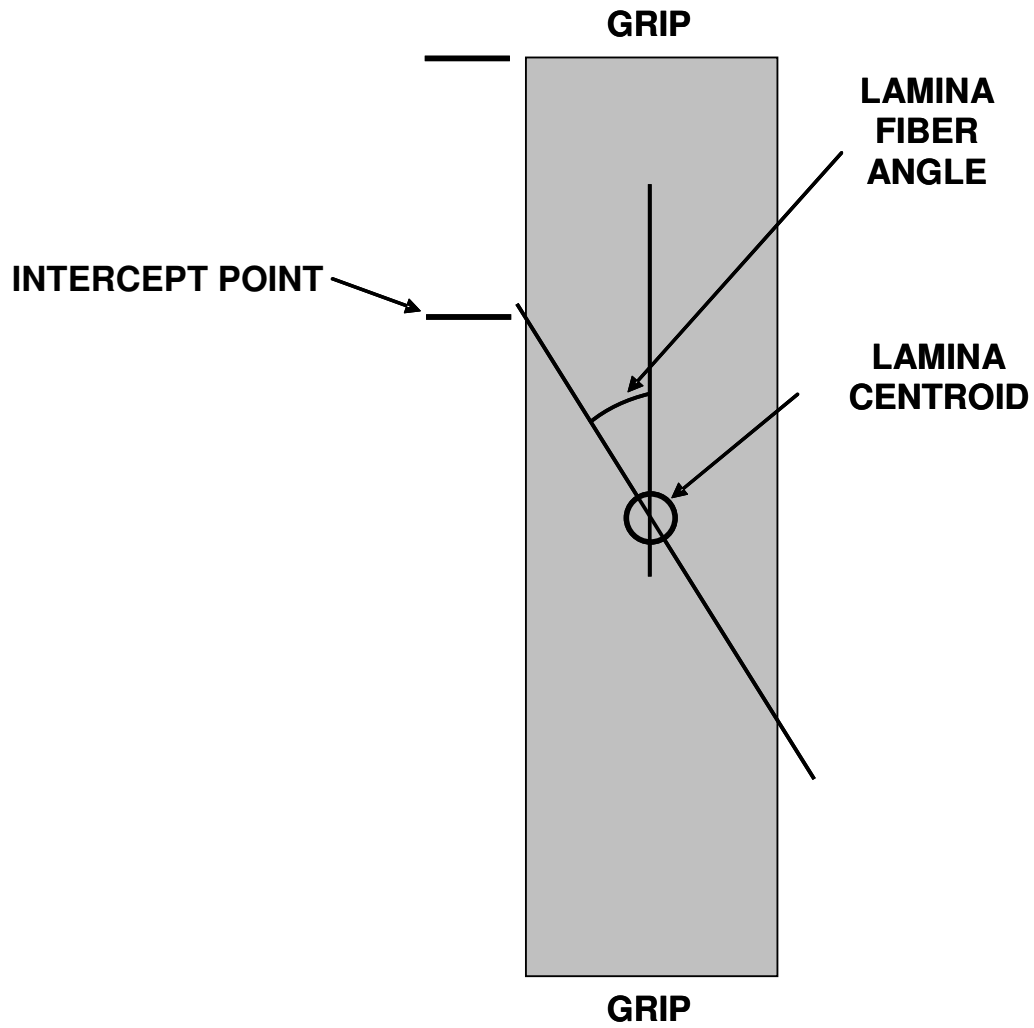


**Figure 82:** Off-Axis Coupon (Jon Gosse, Boeing)

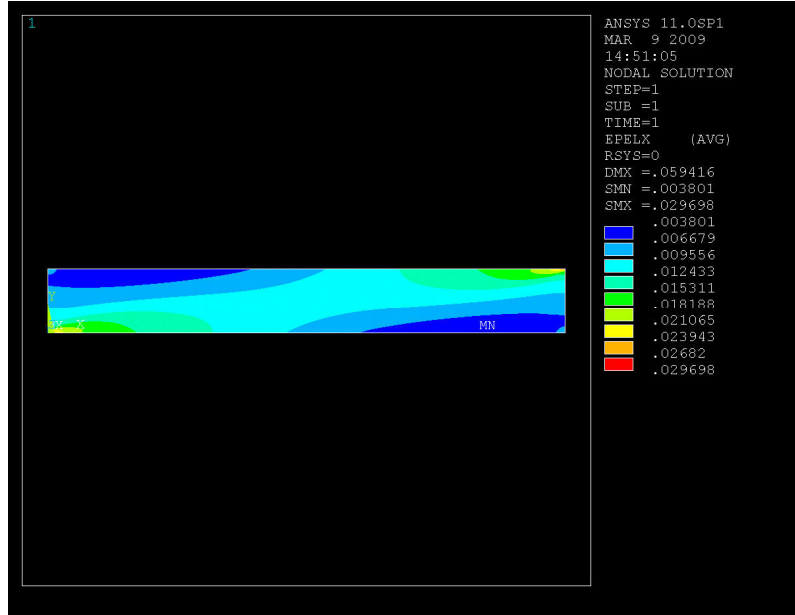


**Figure 83:** Axial Strain along the Major axis of the Coupon (Jon Gosse, Boeing)

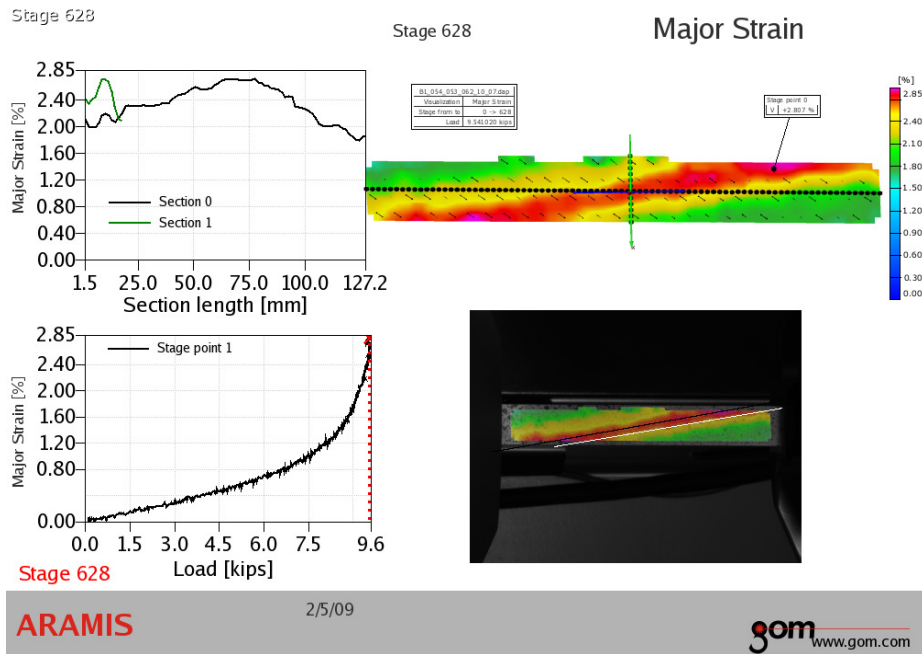
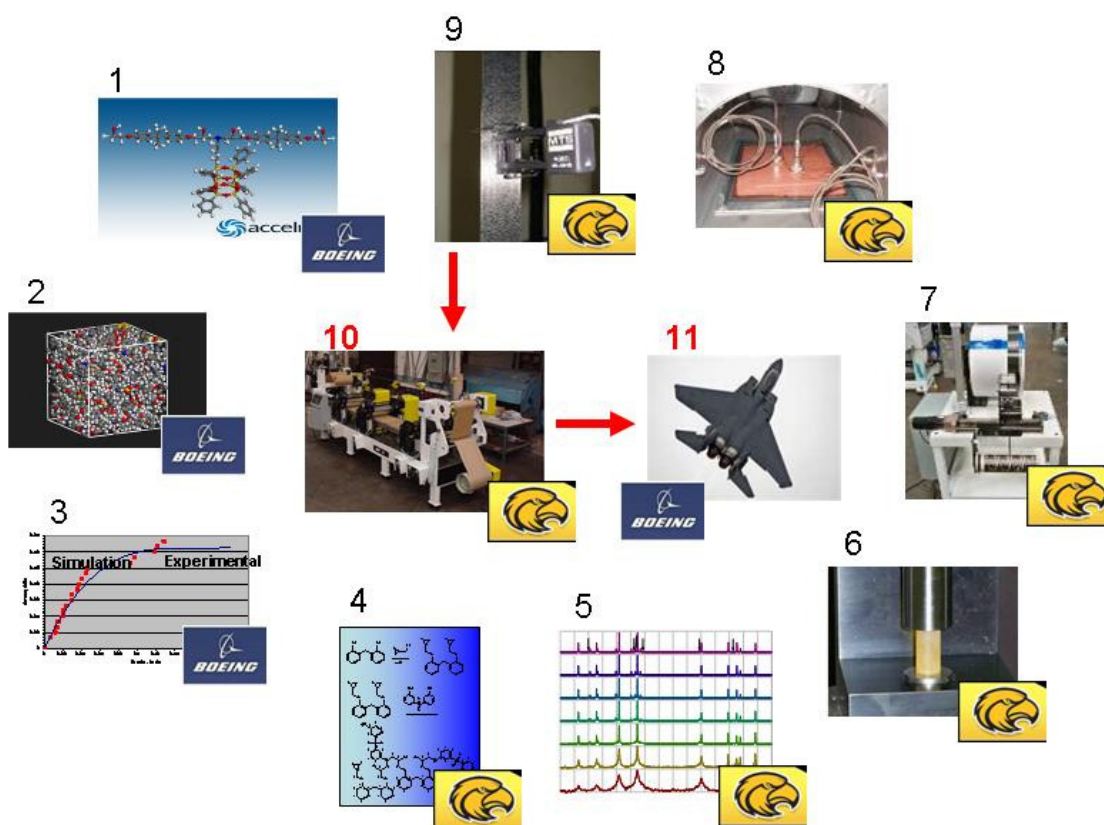


**Figure 84:** DIC 10° Off-Axis Composite Coupon Experimental Results

Validation of Onset Theory Finite Element Models

## CONCLUSIONS

A comprehensive glassy polymer matrix research platform has been established at the University of Southern Mississippi through funds provided by AFOSR and Boeing Research and Technology. The research platform is advancing computational methods for multi-scale modeling frameworks to expedite material development for aerospace. Computational models and solid state analytical techniques to enhance thermal and deformational responses of the network polymers are being developed. In addition, the research platform is developing next generation research scientists who have a unique combination of computational, experimental and engineering skills to drive the continued advancement of composite materials science for aerospace through the next generation.



## **ACKNOWLEDGEMENTS**

The P.I. would like to acknowledge sincere appreciation to the following organizations and individuals for their kind support and collaboration during the course of this research. Air Force Office of Scientific Research Program Managers (Dr. Charles Lee and Dr. Joycelyn Harrison), Award Nos. FA9550-08-1-0077 and FA9550-09-1-0442. Boeing Research and Technology (Director Gerould Young, Director Brian Smith, Senior Manager Steve Precup, Senior Manager Tom Augustine, Senior Manager Dave Furdek, Technical Fellow Steve Christensen, Technical Fellow Terry Schneider, Technical Fellow Jon Gosse, Technical Fellow Diane Rawlings and Technical Fellow Gregg Bogucki). Cytec Engineered Materials (Chief Scientist Rob Maskell, Technical Fellow Jim Senger, Senior Research Manager Steve Ward, Senior Process Engineer Scott Rogers and Senior Manufacturing Manager Joe Ritter).

## **REFERENCES**

1. J.H. Gosse, S. Christensen. Strain invariant failure criteria for polymers in composite materials. American Institute of Aeronautics & Astronautics 2001; AIAA-2001-1184.
2. A.E. Mayr, W.D. Cook, G.H. Edward. Yielding behaviour in model epoxy thermosets - I. Effect of strain rate and composition. *Polymer* 1998; 39: 3719-3724.
3. M. Jerabek, Z. Major, R.W. Lang. Uniaxial compression testing of polymeric materials. *Polym Test* 2010; 29: 302-309.
4. M. Jerabek, Z. Major, R.W. Lang. Strain Determination of Polymeric Materials Using Digital Image Correlation. *Polym Test* 2010; 29: 407-416.
5. T.C. Chu, W.F. Ranson, M.A. Sutton, W.H. Peters. Applications of digital-image-correlation techniques to experimental mechanics. *Exp Mech* 1985; 25: 232-244.
6. H.A. Bruck, S.R. McNeill, M.A. Sutton, W.H. Peters III. Digital image correlation using Newton-Raphson method of partial differential correction. *Exp Mech* 1989; 29: 261-267.
7. W.H. Peters, W.F. Ranson. Digital image technique in experimental stress analysis. *Opt Eng* 1982; 21: 427-431.
8. H. Jin, W. Lu, S. Scheffel, T.D. Hinnerichs, M.K. Neilsen. Full-field characterization of mechanical behavior of polyurethane foams. *Int J Solids Struct* 2007; 44: 6930-6944.
9. J. Tyson, T. Schmidt, K. Galanulis. Full-Field Dynamic Displacement and Strain Measurement Using Advanced 3D Image Correlation Photogrammetry. *Exp Tech Part I* 2003; 27: 47-50.
10. J. Tyson, T. Schmidt, K. Galanulis. Advanced Photogrammetry for Robust Deformation and Strain Measurement. Proceedings of SEM 2002 Annual Conference, Milwaukee, WI, June 2002.

11. F. Grytten, H. Daivan, M. Polanco-Loria, S. Dumoulin. Use of digital image correlation to measure large-strain tensile properties of ductile thermoplastics. *Polym Test* 2009; 28: 653-660.
12. E. Parsons, M.C. Boyce, D.M. Parks. An experimental investigation of the large-strain tensile behavior of neat and rubber-toughened polycarbonate. *Polymer* 2004; 45: 2665-2684.
13. E.M. Parsons, M.C. Boyce, D.M. Parks, M. Weinberg. Three-dimensional large-strain tensile deformation of neat and calcium carbonate-filled high-density polyethylene. *Polymer* 2005; 46: 2257-2265.
14. A. Godara, D. Raabe. Influence of fiber orientation on global mechanical behavior and mesoscale strain localization in a short glass-fiber-reinforced epoxy polymer composite during tensile deformation investigated using digital image correlation. *Compos Sci Technol* 2007; 67: 2417–2427.
15. A. Godara, D. Raabe, I. Bergmann, R. Putz, U. Muller. Influence of additives on the global mechanical behavior and the microscopic strain localization in wood reinforced polypropylene composites during tensile deformation investigated using digital image correlation. *Compos Sci Technol* 2009; 69: 139–146.
16. ARAMIS User Manual by GOM mbH. April 2007 version. Braunschweig, Germany.
17. C. Sachs, H. Fabritius, D. Raabe. Experimental investigation of the elastic–plastic deformation of mineralized lobster cuticle by digital image correlation. *J Struct Biol*, 2006; 155: 409–25.
18. C. Gauthier. “Recovery of glassy polymers.” *Mechanical properties and testing of polymers: an A-Z reference*. Ed. G.M. Swallowe. Kluwer Academic Publishers. 1999. p. 191

19. A. Pegoretti, S. Pandini, T. Ricco. Strain recovery of post-yield compressed semicrystalline polybutylene terephthalate. *Polymer* 2006; 47: 5862-5870.
20. J.T. Bendler, D.G. LeGrand, W.V. Olszewski. Phenomenology of plastic recovery in high polymer glasses. *Polymer* 2001; 43: 389-394.

- 
- <sup>1</sup>. Lesser, A.J.; Calzia, K.J. *J. Polym. Sci.: Part B: Polym. Phys.*, **2004**, 42, 2050.
  - <sup>2</sup>. Bershtein, V.A.; Peschanskaya, N.N.; Halary, J.L.; Monnerie, L. *Polymer*, **1999**, 40, 6687.
  - <sup>3</sup>. Bellenger, V.; Verdu, J.; Francillette, J.; Hoarau, P.; Morel, E. *Polymer*, **1987**, 28, 1079-1086.
  - <sup>4</sup>. Blanco, M.; Ramos, J.A.; Goyanes, S.; Rubiolo, G.; Salgueiro, W.; Somoza, A.; Mondragon, I. *J. Polym. Sci.: Part B: Polym. Phys.*, **2009**, 47, 1240.
  - <sup>5</sup>. Hiemenz, P.C.; Lodge, T.P. *Polymer Chemistry*, 2nd ed.; CRC Press: Boca Raton, FL, 2007; p. 404.
  - <sup>6</sup>. Heinz, S.R.; Wiggins, J.S. *SAMPE International Symposium Proceedings*, Salt Lake City, UT, October 2010.
  - <sup>7</sup>. Crosslinking. <<http://web.mst.edu/~wlf/Coatings/crosslink.html>> (accessed 08/10/2010).
  - <sup>8</sup>. Gosse, J.H. and Christensen, S., *American Institute of Aeronautics & Astronautics*, **2001**, 1184.
  - <sup>9</sup>. Christensen, S. *Explanation of Deformation*, Boeing Internal Report (Seattle, WA, 2001).

- <sup>10</sup>. Kuraishi, A., Gosse, J.H., Wollschlager, J.A. and Townsley, J.L., “Methodology for Composite Durability Assessment” DARPA-NAVAIR Presentation (2005).
- <sup>11</sup>. Seefeldt, M. *Advanced Material Science*; **2001**, 2, 44.
- <sup>12</sup>. Mott, P.H., Argon, A.S. and Suter, U. *Philosophical Magazine*, **1993**, 67, 961.
- <sup>13</sup>. Sternstein, S.S.; Ongchin, L. *ACS Poly. Prepr.*, **1969**, 10, 1117.
- <sup>14</sup>. Zebarjad, S.M.; Bagheri, R.; Seyed Reihani, M.; Lazzeri, A. *J. Appl. Poly. Sci.*, **2003**, *90*, **3767**.
- <sup>15</sup>. Fond, C.; Lobbrecht, A.; Schirrer, R. *International Journal of Fracture*, **1996**, 77, 141.
- <sup>16</sup>. Chui, C.; Boyce, M.C. *Macromolecules*, **1999**, 32, 3795.
- <sup>17</sup>. Capaldi, F.M.; Boyce, M.C.; Rutledge, G.C. *Physical Review Letters*, **2002**, 89, 175505.
- <sup>18</sup>. Argon, A.S.; Cohen, R.E. *Polymer*, **2003**, 44, 6013.
- <sup>19</sup>. Haward, R.N.; Young R.J. *The Physics of Glassy Polymers, 2nd ed.* London, UK: Chapman & Hall, 1997.
- <sup>20</sup>. Hou, Y.; Bai, X.; Gao, J.; Pang, T. *Heilongjiang Daxue Ziran Kexue Xuebao*. **2002**, 22, 781.
- <sup>21</sup>. Morrison, R.T.; Boyd, R.N. *Organic Chemistry, 5th ed.* Newton, MA: Allyn and Bacon, Inc, 1987
- <sup>22</sup>. Brown, T.L., LeMay, H.E., and Bursten, B.E. *Chemistry the Central Science, 6th ed.* Englewood Cliffs, NJ: Prentice Hall, 1994
- <sup>23</sup>. Atkins, P. and de Paula, J. *Atkin’s Physical Chemistry, 8th ed.* New York, NY: W.H. Freeman and Company, 2006.
- <sup>24</sup>. Gedde, U.W. *Polymer Physics*, 1st ed.; Chapman & Hall: London, UK, 1995; p. 92.
- <sup>25</sup>. Sun, N.; Liu, J.; Dull, T.; Yee, A.F. *J. Polym. Sci.: Part B: Polym. Phys.* **2007**, 45, 1410.
- <sup>26</sup>. Mijovic, J.; Zhang, H. *Macromolecules* **2003**, 36, 1279.

- <sup>27</sup>. Liu, J.; Yee, A.F. *Macromolecules* **1998**, *31*, 7865.
- <sup>28</sup>. Shi, J.-F.; Inglefield, P.T.; Jones, A.A.; Meadows, M.D. *Macromolecules* **1996**, *29*, 605.
- <sup>29</sup>. Bartolotta, A.; Carini, G.; Carini, G.; DiMarco, G.; Tripodo, G. *Macromolecules* **2010**, *43*, 4798.
- <sup>30</sup>. Schimidt-Rohr, K.; Kulik, A.S.; Beckham, H.W.; Ohlemacher, A.; Pawelzik, U.; Boeffel, C.; Spiess, H.W. *Macromolecules* **1994**, *27*, 4733.
- <sup>31</sup>. Kuebler, S.C.; Schaefer, D.J.; Boeffel, C.; Pawelzik, U.; Spiess, H.W. *Macromolecules* **1997**, *30*, 6597.
- <sup>32</sup>. Vogel, M.; Medick, P.; Rossler, E.A. *Ann. Rep. on NMR Spec.* **2005**, *56*, 231.
- <sup>33</sup>. Matsuoka, S.; Hale, A. *J. Appl. Polym. Sci.* **1997**, *64*, 77.
- <sup>34</sup>. Fitz, B.; Andjelic, S.; Mijovic, J. *Macromolecules* **1997**, *30*, 5227.
- <sup>35</sup>. Merenga, A.S.; Papadakis, C.M.; Kremer, F.; Liu, J.; Yee, A.F. *Colloid Polym. Sci.* **2001**, *279*, 1064.
- <sup>36</sup>. Jho, J.Y.; Yee, A.F. *Macromolecules* **1991**, *24*, 1905.
- <sup>37</sup>. Li, L.; Yee, A.F. *Macromolecules* **2002**, *35*, 425.
- <sup>38</sup>. Starkweather, H.W. *Macromolecules* **1981**, *14*, 1277.
- <sup>39</sup>. Pinto, S.S.; Moura-Ramos, J.J.; Diogo, H.P. *Euro. Polym. J.* **2009**, *45*, 2644.
- <sup>40</sup>. Starkweather, H.W. *Macromolecules* **1988**, *21*, 1798.
- <sup>41</sup>. Chen, L.P.; Yee, A.F.; Goetz, J.M.; Schaefer, J. *Macromolecules* **1998**, *31*, 5371.
- <sup>42</sup>. Heux, L.; Halary, J.L.; Laupretre, F.; Monnerie, L. *Polymer* **1997**, *38*, 1767.
- <sup>43</sup>. Johari, G.P.; Goldstein, M. *J. Chem. Phys.* **1970**, *53*, 2372.
- <sup>44</sup>. Johari, G.P. *J. Chem. Phys.* **1973**, *58*, 1766.
- <sup>45</sup>. Ngai, K.L.; Paluch, M. *J. Chem. Phys.* **2004**, *120*, 857.

- <sup>46</sup>. Tombari, E.; Salvetti, G.; Johari, G.P. *J. Chem. Phys.* **2000**, *113*, 6957.
- <sup>47</sup>. Kessairi, K.; Capaccioli, S.; Prevosto, D.; Lucchesi, M.; Sharifi, S.; Rolla, P.A. *J. Phys. Chem. B.* **2008**, *112*, 4470.
- <sup>48</sup>. Bengtzelius, U.; Gotze, W.; Sjolander, A. *J. Phys. Solid State Phys.* **1984**, *C17*, 5915.
- <sup>49</sup>. Gotze, W.; Sjogren, L. *Rep. Prog. Phys.* **1992**, *55*, 241.
- <sup>50</sup>. Schilling, R. *Disorder Effects on Relaxational Processes*; Springer-Verlag: Berlin, 1994; p. 193.
- <sup>51</sup>. Ngai, K.L. *J. Chem. Phys.* **1998**, *109*, 6982.
- <sup>52</sup>. Brand, R.; Lunkenheimer, P.; Loidl, A. *J. Chem. Phys.* **2002**, *116*, 10386.
- <sup>53</sup>. Hachenberg, J.; Bedorf, D.; Samwer, K. *Appl. Phys. Lett.* **2008**, *92*, 131911.
- <sup>54</sup>. Pelletier, J.M.; Perez, J.; Duffrene, L.; Sekkat, A. *J. Non-Cryst. Solid.* **1999**, *258*, 119.
- <sup>55</sup>. Thayyil, M.S.; Capaccioli, S.; Prevosto, D.; Ngai, K.L. *Philos. Mag.* **2008**, *88*, 4007.
- <sup>56</sup>. Bogoslovov, R.B.; Hogan, T.E.; Roland, C.M. *Macromolecules* **2010**, *43*, 2904.
- <sup>57</sup>. Roland, C.M.; Schroeder, M.J.; Fontanella, J.J.; Ngai, K.L. *Macromolecules* **2004**, *37*, 2630.
- <sup>58</sup>. Casalini, R.; Roland, C.M. *Macromolecules* **2005**, *38*, 1779.
- <sup>59</sup>. Kaminski, K.; Wlodarczyk, P.; Adrjanowicz, K.; Kaminska, E.; Wojnarowska, Z.; Paluch, M. *J. Phys. Chem. B* **2010**, *114*, 11272.
- <sup>60</sup>. Beiner, M.; Ngai, K.L. *Macromolecules* **2005**, *38*, 7033.
- <sup>61</sup>. Baljon, A.R.C.; Robbins, M.O. *Computational and Theoretical Polymer Science* **1999**, *9*, 35.
- <sup>62</sup>. Malandro, D.L.; Lacks, D.J. *J. of Chemical Physics* **1999**, *110*, 4593.
- <sup>63</sup>. Chui, D. and Boyce, M.C. *Macromolecules* **1999**, *32*, 3795.
- <sup>64</sup>. Kauskik, M.; Jackson, M.; Heinz, S; Wiggins, J.S.; Nazarenko, S. *SAMPE International Symposium Proceedings*, Wichita, KS, 2009.

- <sup>65</sup>. David, L.; Etienne, S. *Macromolecules*, **1992**, 25, 4302-4308.
- <sup>66</sup>. Cholli, A.L.; Dumais, J.J.; Engel, A.K.; Jelinski, L.W. *Macromolecules*, **1984**, 17, 2399-2404.
- <sup>67</sup>. Schaefer, J.; *Macromolecules*, **1985**, 18, 368-373.
- <sup>68</sup>. Sydney K. Brownstein and Michael D. Guiver, *Macromolecules*, **1992**, 25, 5181-5185.
- <sup>69</sup>. Marano, C.; Rink, M. *Mech. Time-Dependent Mat.* **2005**, 9, 1.
- <sup>70</sup>. Viscoelasticity notes. <<http://silver.neep.wisc.edu/~lakes/VENotes.html>> (accessed 8/29/2010).
- <sup>71</sup>. Gedde, U.W. *Polymer Physics*, 1st ed.; Chapman & Hall: London, UK, 1995; p.41.
- <sup>72</sup>. Lakes, R.S. *Viscoelastic Solids*; CRC Press: Boca Raton, FL, 1999.
- <sup>73</sup>. **G'Sell, C.** *Mat. Sci. Eng. A*, **2001**, 309, 539.
- <sup>lxxiv</sup>. *Accelrys Materials Studio 5.0 Help*, Group Based Cutoff.
- <sup>lxxv</sup>. Allen, M.P.; Tildesley, D.J. *Computer simulation of liquids*. New York, NY. Clarendon Pr. (1993).
- <sup>lxxvi</sup>. *Accelrys Materials Studio 5.0 Help*. Static Elastic Property Determination.
- <sup>77</sup>. Stephen Todd, "Accelrys Build and optimize dendrimer," 2009, <<https://community.accelrys.com/thread/1876>>.
- <sup>78</sup>. Andrea Browning, *Strain Controlled True Strain* (Boeing, 2010).
- <sup>79</sup>. Mirau, P.A. *A practical guide to understanding the NMR of polymers* Wiley-Interscience, New Jersey (2005).
- <sup>80</sup>. Schmidt-Rohr, K.; Spiess, H. W. *Multidimensional Solid-State NMR and Polymers*; Academic Press: San Diego, (1996) Chapters 7 and 8
- <sup>81</sup>. Shi, J.F.; Ingelfield, P.T.; Jones, A.A.; Meadows, M.D.; , *Macromolecules*, **1996**, 29, 605-609.

- <sup>82</sup>. Vorselaars, B; Lyulin, A.V.; Michels, M.A.J. *Macromolecules*, **2007**, *40*, 6001-6011.
- <sup>83</sup>. Chen, L.P.; Yee, A.F. *Macromolecules*, **1998**, *31*, 5371-5382.
- <sup>84</sup>. Sauvant, V.; Halary, J.L. *Journal of Applied Polymer Science*, **2001**, *82*, 759-774.
- <sup>85</sup>. Blanco, M.; Ramos, J.A.; Goyanes, S.; Rubiolo, G.; Salgueiro, W.; Somoza, A; Mondragon, I. *Journal of Polymer Science Part B: Polymer Physics*, **2009**, *47*, 1240-1252.
- <sup>86</sup>. Vold, R.L.; Hoatson, G.L. *Journal of Magnetic Resonance*, **2009**, *198*, 57-72.
- <sup>87</sup>. Roy, A.K.; Jones, A.A., Ingelfield, P.T. *Macromolecules*, **1986** *19*, 1356-1362.
- <sup>88</sup>. Schaefer, J.; Stejskal, E.O.; Perchak, D., Skolnick, J.; Yaris, R. *Macromolecules*, **1985**, *18*, 368-373.
- <sup>89</sup>. McEachern, D.M.B; Lehmann, P.E.F. *Journal of Molecular Structure*, **1971**, *7*, 267-276.
- <sup>90</sup>. Taylor, R.E.; Bacher, A.D.; Dybowski, C. *Journal of Molecular Structure*, **2007**, *846*, 147-152.
- <sup>91</sup>. Cholli, A.L.; Dumais, J.J.; Engel, A.K.; Jelinski, L.W. *Macromolecules*, **1984**, *17*, 2399-2404.
- <sup>92</sup>. Hiraoki, T.; Kogame, A.; Nishi, N.; Tsutsumi, A. *Journal of Molecular Structure*, **1998**, *441*, 243-250.
- <sup>93</sup>. Clayden, N.J. *Polymer*, **2000**, *41*, 1167-1174.
- <sup>94</sup>. Schaefer, J.; Stejskal, E.O.; Buchdahl, R. *Macromolecules*, **1977**, *10*, 384-405.
- <sup>95</sup>. Dixon, W.T. *The Journal of Chemical Physics*, **1982**, *77* 1800.
- <sup>96</sup>. Harris, R.K.; Yeung, R.R.; Johncock, P.; Jones, D. *Polymer*, **1996**, *37*, 721-727.
- <sup>97</sup>. Schaefer, J.; Stejskal, E.O.; Buchdahl, R. *Macromolecules*, **1977**, *10*, 384-405.
- <sup>98</sup>. Dixon, W.T. *The Journal of Chemical Physics*, **1982**, *77* 1800.
- <sup>99</sup>. Harris, R.K.; Yeung, R.R.; Johncock, P.; Jones, D. *Polymer*, **1996**, *37*, 721-727.
- <sup>100</sup>. Jeremy Swanson, Dissertation. Hattiesburg, MS: University of Southern Mississippi, 2010.

- <sup>101</sup> Oleinik EF. *Epoxy-aromatic amine networks in the glassy state: structure and properties*. In: Dušek K. *Advances in Polymer Science: Epoxy Resins and Composites IV*, Vol. 80. Verlag Berlin Heidelberg: Springer, 1986. pp. 49-99.
- <sup>102</sup> Hiemenz PC, Lodge, TP. *Polymer Chemistry*, 2nd ed. Boca Raton, FL: CRC Press, 2007. p. 404.
- <sup>103</sup> Tucker SJ, Fu B, Kara S, Heinz S, Wiggins JS. *Composites Part A Appl Sci Manufact*, **2010**, 1441-1446.
- <sup>104</sup> Ochi M, Shimbo M, Saga M, Takashima, N. *J Polym Sci Part B Polym Phys*, **1986**, 2185-2195.
- <sup>105</sup> Mikolajczak G, Cavaille JY, Johari GP. *Polymer* **1987**, 2023-2031.
- <sup>106</sup> Wiggins JS, Hassan MK, Mauritz KA, Storey RF. *Polymer*, **2006**, 1960–1969.
- <sup>107</sup> Rhoades DW, Hassan MK, Osborn SJ, Moore RB, Mauritz KA. *J Power Sources*, **2007**, 72–77.
- <sup>108</sup> Osborn SJ, Hassan MK, Divoux GM, Rhoades DW, Mauritz KA, Moore RB. *Macromolecules*, **2007**, 3886-3890.
- <sup>109</sup> Kremer F, Schönhals A. *Broadband Dielectric Spectroscopy*, Berlin: Springer, 2003. p 225.
- <sup>110</sup> Mauritz KA, Stefanithis ID. *Macromolecules*, **1990**, 1380.
- <sup>111</sup> Keenan JD, Seferis JC, Quinlivan JT. *J Appl Polym Sci*, **1979**, 2375-2387.
- <sup>112</sup> Mikolajczak G, Cavaille JY, Johari GP. *Polymer* **1987**, 2023-2031.
- <sup>113</sup> Ochi M, Okazaki, M, Shimbo M. *J Polym Sci Part B Polym Phys*, **1982**, 689-699.
- <sup>114</sup> Flory PJ. *J Macromol Sci Part B Phys*, **1976**, 1-11.
- <sup>115</sup> Havriliak S, Negami S. *Polymer*, **1967**, 161.

- <sup>116</sup> Kremer F, Schönhals A. *Broadband Dielectric Spectroscopy*, Berlin: Springer, 2003. p 64.
- <sup>117</sup> Ochi M, Yoshizumi, M, Shimbo M. *J Polym Sci Part B Polym Phys*, **1987**, 25, 1817-1827.
- <sup>118</sup> Mangion MBM, Johari GP. *J Polym Sci Part B Polym Phys*, **1990**, 71-83.
- <sup>119</sup> Mangion MBM. PhD Thesis, McMaster University, 1990.
- <sup>120</sup> Day DR, Lewis TJ, Lee HL, Senturia SD. *J Adhesion*, **1985**, 73-90.
- <sup>121</sup> McCrum NG, Read BE, Williams, G. *Anelastic and Dielectric Effects in Polymeric Solids*.  
New York: Dover, 1991.
- <sup>122</sup> Vogel H. *Phys Z* **1921**, 645; Fulcher GS. *J Am Ceram Soc*, **1923**, 339; Tammann G, Hesse W.  
*Z Anorg Allgem Chem*, **1926**, 245.
- <sup>123</sup> Kaushik M, Jackson M, Heinz S, Wiggins J, Nazarenko S. *Proc. from SAMPE I'nat. Conf*.  
Wichita, KS. 2009.
- <sup>124</sup> J.H. Gosse, S. Christensen. Strain invariant failure criteria for polymers in composite materials. American Institute of Aeronautics & Astronautics 2001; AIAA-2001-1184.
- <sup>125</sup> A.E. Mayr, W.D. Cook, G.H. Edward. Yielding behaviour in model epoxy thermosets - I. Effect of strain rate and composition. *Polymer* 1998; 39: 3719-3724.
- <sup>126</sup> M. Jerabek, Z. Major, R.W. Lang. Uniaxial compression testing of polymeric materials. *Polym Test* 2010; 29: 302-309.
- <sup>127</sup> M. Jerabek, Z. Major, R.W. Lang. Strain Determination of Polymeric Materials Using Digital Image Correlation. *Polym Test* 2010; 29: 407-416.
- <sup>128</sup> T.C. Chu, W.F. Ranson, M.A. Sutton, W.H. Peters. Applications of digital-image-correlation techniques to experimental mechanics. *Exp Mech* 1985; 25: 232-244.

- <sup>129</sup> H.A. Bruck, S.R. McNeill, M.A. Sutton, W.H. Peters III. Digital image correlation using Newton-Raphson method of partial differential correction. *Exp Mech* 1989; 29: 261-267.
- <sup>130</sup> W.H. Peters, W.F. Ranson. Digital image technique in experimental stress analysis. *Opt Eng* 1982; 21: 427-431.
- <sup>131</sup> H. Jin, W. Lu, S. Scheffel, T.D. Hinnerichs, M.K. Neilsen. Full-field characterization of mechanical behavior of polyurethane foams. *Int J Solids Struct* 2007; 44: 6930-6944.
- <sup>132</sup> J. Tyson, T. Schmidt, K. Galanulis. Full-Field Dynamic Displacement and Strain Measurement Using Advanced 3D Image Correlation Photogrammetry. *Exp Tech Part I* 2003; 27: 47-50.
- <sup>133</sup> J. Tyson, T. Schmidt, K. Galanulis. Advanced Photogrammetry for Robust Deformation and Strain Measurement. *Proceedings of SEM 2002 Annual Conference, Milwaukee, WI, June 2002.*
- <sup>134</sup> F. Grytten, H. Daivan, M. Polanco-Loria, S. Dumoulin. Use of digital image correlation to measure large-strain tensile properties of ductile thermoplastics. *Polym Test* 2009; 28: 653-660.
- <sup>135</sup> E. Parsons, M.C. Boyce, D.M. Parks. An experimental investigation of the large-strain tensile behavior of neat and rubber-toughened polycarbonate. *Polymer* 2004; 45: 2665-2684.
- <sup>136</sup> E.M. Parsons, M.C. Boyce, D.M. Parks, M. Weinberg. Three-dimensional large-strain tensile deformation of neat and calcium carbonate-filled high-density polyethylene. *Polymer* 2005; 46: 2257-2265.
- <sup>137</sup> A. Godara, D. Raabe. Influence of fiber orientation on global mechanical behavior and mesoscale strain localization in a short glass-fiber-reinforced epoxy polymer composite

- during tensile deformation investigated using digital image correlation. *Compos Sci Technol* 2007; 67: 2417–2427.
- <sup>138</sup> A. Godara, D. Raabe, I. Bergmann, R. Putz, U. Muller. Influence of additives on the global mechanical behavior and the microscopic strain localization in wood reinforced polypropylene composites during tensile deformation investigated using digital image correlation. *Compos Sci Technol* 2009; 69: 139–146.
- <sup>139</sup> ARAMIS User Manual by GOM mbH. April 2007 version. Braunschweig, Germany.
- <sup>140</sup> C. Sachs, H. Fabritius, D. Raabe. Experimental investigation of the elastic–plastic deformation of mineralized lobster cuticle by digital image correlation. *J Struct Biol*, 2006; 155: 409–25.
- <sup>141</sup> C. Gauthier. “Recovery of glassy polymers.” *Mechanical properties and testing of polymers: an A-Z reference*. Ed. G.M. Swallowe. Kluwer Academic Publishers. 1999. p. 191
- <sup>142</sup> A. Pegoretti, S. Pandini, T. Ricco. Strain recovery of post-yield compressed semicrystalline polybutylene terephthalate. *Polymer* 2006; 47: 5862-5870.
- <sup>143</sup> J.T. Bendler, D.G. LeGrand, W.V. Olszewski. Phenomenology of plastic recovery in high polymer glasses. *Polymer* 2001; 43: 389-394.